

UNIVERSITY OF CALIFORNIA
Santa Barbara

**Probing Strongly-Scattered Compact Objects
Using Ultra-High-Resolution Techniques in
Radio Astronomy**

A dissertation submitted in partial satisfaction
of the requirements for the degree of

Doctor of Philosophy

in

Physics

by

Michael Douglas Johnson

Committee in Charge:

Professor Carl Gwinn, Chair

Professor Omer Blaes

Professor Tommaso Treu

June 2013

The dissertation of
Michael Douglas Johnson is approved:

Professor Omer Blaes

Professor Tommaso Treu

Professor Carl Gwinn, Committee Chairperson

May 2013

**Probing Strongly-Scattered Compact Objects Using
Ultra-High-Resolution Techniques in Radio Astronomy**

Copyright © 2013

by

Michael Douglas Johnson

To Kristy.

For the song of the stars.

Acknowledgements

This dissertation is a reflection of the patience, support, and wisdom of my advisor, Carl Gwinn. I thank him for a seemingly boundless supply of insight, for teaching me how to unravel the elegance lurking within paradoxes, and for giving balance and meaning to my years here at UCSB.

The astronomy group has been exceptional as well. Even before I began research in astronomy, the atmosphere was both welcoming and dynamic. I especially thank Omer Blaes – his passion teaching graduate courses and fascinating discussions have served as a guide for the deep thinking that underlies the best of theoretical astrophysics. I also thank Tommaso Treu his many thoughtful comments about statistics and modeling and for graciously serving on my thesis committee.

These projects have required the expertise of several exceptional collaborators. In particular, Paul Demorest generously shared his knowledge on many observing runs, each of which seemed to require a new challenge – our observational results would have been impossible without his expertise.

Outside of astronomy, my friends have enabled some shreds of perspective in the journey to scholarship. Devin and Idse were mostly-willing cohorts on many ill-conceived adventures, and our years sharing an apartment provided many of my fondest memories of graduate school.

This work represents only the most recent chapter in a lifetime of scientific curiosity, and I thank my parents both for a home that always encouraged education and the many sacrifices they made to provide excellent opportunities for my siblings and me. Despite their unwillingness to sacrifice our house to electrolysis experiments, I never would have considered a scientific career without their guidance and support.

And, though words cannot begin to acknowledge the countless, selfless sacrifices that she has made, I thank Kristy. She has always been both my Muse and unwavering support, and I dedicate this thesis to her.

Michael D. Johnson

April 2013

Curriculum Vitae

Michael Douglas Johnson

Education

2013 Ph.D. in Physics, University of California, Santa Barbara (expected)
2010 M.A. in Physics, University of California, Santa Barbara
2007 B.S. in Physics; B.S. in Mathematics (summa cum laude), University of Southern California

Publications

“Interferometric Visibility of a Scintillating Source: Statistics at the Nyquist Limit,” **Johnson, M. D.** & Gwinn, C. R. 2013, ApJ, 768, 170

“Optimal Correlation Estimators for Quantized Signals,” **Johnson, M. D.**, Chou, H. H., & Gwinn, C. R. 2013, ApJ, 765, 135

“Constraining the Vela Pulsar’s Radio Emission Region Using Nyquist-Limited Scintillation Statistics,” **Johnson, M. D.**, Gwinn, C. R., & Demorest, P. 2012, ApJ, 758, 8

“Size of the Vela Pulsar’s Emission Region at 18 cm Wavelength,” Gwinn, C. R., **Johnson, M. D.**, Reynolds, J. E., Jauncey, D. L., Tzioumis, A. K., Dougherty, S., Carlson, B., Del Rizzo, D., Hirabayashi, H., Kobayashi, H., Murata, Y., Edwards, P. G., Quick, J. F. H., Flanagan, C. S., & McCulloch, P. M. 2012, ApJ, 758, 7

“Noise in the Cross-Power Spectrum of the Vela Pulsar,” Gwinn, C. R., **Johnson, M. D.**, Reynolds, J. E., Jauncey, D. L., Tzioumis, A. K., Dougherty, S., Carlson, B., Del Rizzo, D., Hirabayashi, H., Kobayashi, H., Murata, Y., Edwards, P. G., Quick, J. F. H., Flanagan, C. S., & McCulloch, P. M. 2012, ApJ, 758, 6

“Ultra-High-Resolution Intensity Statistics of a Scintillating Source,” **Johnson, M. D.** & Gwinn, C. R. 2012, ApJ, 755, 179

“Effects of Intermittent Emission: Noise Inventory for Scintillating Pulsar B0834+06,” Gwinn, C. R., **Johnson, M. D.**, Smirnova, T. V., & Stinebring, D. R. 2011, ApJ, 733, 51

“Noise and Signal for Spectra of Intermittent Noiselike Emission,” Gwinn, C. R. & **Johnson, M. D.** 2011, ApJ, 554, 1197

“Chaotic Time Reversed Acoustics: Sensitivity of the Loschmidt Echo to Perturbations,” Taddese, B. T., **Johnson, M. D.**, Hart, J. A., Antonsen, T. M., Ott, E., & Anlage, S. M. 2009, Acta Physica Polonica A, 116, 729

“Density of States of Helium Droplets,” Hansen, K., **Johnson, M. D.**, & Kresin, V. V. 2007, Phys. Rev. B, 76, 235424

“An Advanced, Low-Cost, GPS-Based Animal Tracking System,” Clark, P. E., Johnson, D. E., Kniep, M. A., Huttash, B., Wood, A., **Johnson, M. D.**, McGillivan, C., & Titus, K. 2006, J. Range Ecology & Management, 59(3):334340

Abstract

Probing Strongly-Scattered Compact Objects Using Ultra-High-Resolution Techniques in Radio Astronomy

Michael Douglas Johnson

This dissertation explores fundamental limits in radio astronomy and develops techniques that utilize the scintillation of compact objects to probe detailed properties of their emission regions and of the scattering material. I develop a statistical framework for observations with spectral resolution at or near the Nyquist limit, suitable for describing the observed statistics of strongly-scattered sources. I demonstrate that these statistics can effectively isolate the signature of an extended emission region, requiring no assumptions about the nature or distribution of the scattering material. Then, using observations of the Vela pulsar at 760 MHz with the Green Bank Telescope, I thereby achieve a spatial resolution of 4 km at the pulsar. Finally, I explore the signature of refractive scintillation on the interferometric visibility measured on long baselines, and I derive optimal correlation estimators for quantized data.

Contents

Abstract	viii
1 Introduction	1
1.1 Scintillation	2
1.2 Pulsars	4
1.3 Propagation Effects in the Ionized Interstellar Medium	6
1.3.1 The Spectrum of Electron Density Fluctuations in the ISM: a Turbulent Cascade?	9
1.3.2 Diffractive and Refractive Branches of Scintillation	11
1.4 Outline of Dissertation	12
2 Flux-Density Statistics for a Scintillating Source	14
2.1 Introduction	16
2.1.1 Noise and Scintillation	16
2.1.2 Strategy for Comparison with Observations	19
2.1.3 Comparison with Previous Work	19
2.1.4 Outline of Chapter	21
2.2 Theoretical Background	21
2.2.1 Pulsar Radio Emission	21
2.2.2 Interstellar Scattering	23
2.2.3 Instrumental and Observational Requirements	24
2.2.4 Notation	25
2.3 Distribution of Intensity	26
2.3.1 The Exact Intensity PDF	26
2.3.2 Approximating the Intensity PDF	29
2.3.2.1 The i.i.d. Approximation	30
2.3.2.2 The Gamma Approximation	31
2.3.2.3 The Gaussian Approximation	33
2.3.3 Utility of Approximations	33
2.4 PDF Modifications	35

2.4.1	Effects of Temporal Decorrelation	36
2.4.2	Effects of Extended Source Emission	39
2.4.2.1	Effects of a Non-Static Emission Region	45
2.4.3	Comparison of Emission Size and Temporal Decorrelation	46
2.4.4	Effects of Noise and Bias in Model Parameters	47
2.4.4.1	Effects of Biased Background or Source Amplitude	48
2.4.4.2	Effects of Background or Source Parameter Noise	49
2.4.5	Effects of Instrumental Distortion	51
2.4.6	Expected Resolving Power	52
2.5	Moments of the Distributions: The Modulation Index and Self-Noise	55
2.5.1	The Modulation Index	55
2.5.2	An Estimate of Self-Noise	58
2.6	Summary	60
2.7	Appendix: Mathematical Results	62
2.7.1	Average of Exponential Random Variables with Different Scales	62
2.7.2	Distribution of Correlated Exponential Random Variables	63
2.7.2.1	Example: Bivariate PDF of Correlated Exponential Random Variables	65
2.7.2.2	Convolution of Correlated Exponential Random Variables	65

3 Interferometric Visibility of a Scintillating Source: Statistics at the Nyquist Limit 67

3.1	Introduction	68
3.1.1	Assumptions and Strategy for Comparison with Observations	70
3.1.2	Relation to Previous Work	72
3.1.3	Outline of Chapter	73
3.2	PDF of Visibility	74
3.2.1	Field Statistics	76
3.2.2	Moments and Noise of Snapshot Visibilities	79
3.2.3	Approximating the Visibility Statistics within a Scintillation Snapshot	82
3.2.3.1	The i.i.d. Approximation	82
3.2.3.2	The Gaussian Approximation	83
3.2.4	The PDF of Visibility	84
3.2.4.1	The i.i.d. Approximation	85
3.2.4.2	The Gaussian Approximation	86
3.2.5	Examples	89
3.2.5.1	Zero-Baseline	89
3.2.5.2	Long-Baseline	90
3.2.5.3	High Signal-to-Noise	91

3.2.6	Asymptotic Behavior	93
3.2.7	Estimation of the Self-Noise	95
3.3	Effects of an Extended Emission Region on the Visibility PDF . .	97
3.3.1	The Effects of an Extended Emission Region on the Field Statistics	97
3.3.2	The Relation Between the Emission Region and the Dimensionless Size Parameters $\gamma_{s,i}$	100
3.3.3	Approximate Evaluation of the PDF of Visibility	101
3.3.4	The Short Baseline Limit	103
3.4	Summary	105
3.5	Appendix: Mathematical Results	106
3.5.1	Product of Correlated Complex Gaussian Random Variables	106
3.5.2	Visibility Projections	108
4	Constraining the Vela Pulsar's Radio Emission Region	110
4.1	Introduction	111
4.1.1	Pulsar Emission and Scintillation	111
4.1.2	Comparison with Previous Work	113
4.1.3	Outline of Chapter	115
4.2	Theoretical Background	116
4.2.1	Pulsar Radio Emission	116
4.2.2	Interstellar Scattering	117
4.2.2.1	Scintillation Physics	117
4.2.2.2	Interpretation of the Inferred Emission Size . . .	118
4.2.2.3	Scattering Geometry of the Vela Pulsar	119
4.3	Observation and Data Reduction	120
4.3.1	Observation and Baseband Recording	120
4.3.2	Coherent Dedispersion and Formation of Spectra	120
4.3.3	Data Excision and Bandpass Correction	121
4.3.3.1	RFI Excision	121
4.3.3.2	Background Noise and Bandpass Shape Estimation	122
4.3.3.3	Rejection of Pulses with Quantization Saturation	122
4.3.4	Observed PDF of Intensity	123
4.3.4.1	Histogram Formation	123
4.3.4.2	Effects of Finite Histogram Resolution	123
4.3.5	Model PDF of Intensity	124
4.3.5.1	Model PDF Parameter Estimation	125
4.3.5.2	Construction of the Model PDF	125
4.3.6	Expected Residual Structure	126
4.3.7	Fitting the Residual Structure	128
4.4	Analysis	128
4.4.1	All Pulses	129

4.4.2	$N = 2$ with Temporal Lag $\Delta\tau$	131
4.4.3	Quantiles	133
4.4.4	Single-Pulse Statistics	134
4.5	Sources of Bias in the Estimated Emission Size	135
4.5.1	Effects of Noise in Model Parameters	136
4.5.2	Effects of Bias in Model Parameters	137
4.5.3	Effects of Modified Scattering Assumptions	139
4.5.4	Effects of Proper Motion	140
4.6	Interpretation	141
4.6.1	Geometric Model for Pulsar Emission	141
4.6.2	Emission Altitude from Effective Transverse Size	143
4.6.3	Comparison with Previous Emission Altitude Estimates	144
4.6.4	Comparison with 1.66 GHz and 2.3 GHz Scintillation Studies	145
4.7	Summary	146
5	The Effects of Refractive Substructure on Ultra-Long-Baseline	
	Visibilities	149
5.1	Refractive Scintillation and Noise	149
5.2	Scattering and Scintillation	151
5.2.1	The Phase Structure Function	151
5.2.2	The Averaging Regimes for Interferometric Visibility	153
5.3	Interferometric Visibility from Kirchoff Diffraction	154
5.3.1	The Scalar Electric Field	154
5.3.2	The Ensemble-Average Visibility	156
5.4	Refractive Noise	158
5.4.1	The Second Moment of $ V_{ss} $	158
5.4.2	Refractive Noise	160
5.4.2.1	One-Dimensional, Isotropic Scattering	161
5.4.2.2	Two-Dimensional, Isotropic Scattering	164
5.4.2.3	The Effects of an Extended Emission Region	165
5.4.2.4	The Effects of Anisotropy	166
5.4.3	The Distribution of Refractive Noise	168
5.5	The Utility of Refractive Noise	170
6	Optimal Correlation Estimators for Quantized Signals	172
6.1	Introduction	174
6.1.1	Terminology and Notation	175
6.1.2	Relation to Previous Work	176
6.1.3	Outline of Chapter	177
6.2	Mathematical Background	177
6.2.1	Optimal Estimators and Maximum Likelihood	178
6.2.2	Distribution of Correlated Gaussian Variables	179

6.3	Correlation Estimators for Unquantized Signals	180
6.3.1	Correlation via Sample Covariance: r_∞	181
6.3.2	Optimal Correlation: r_p	182
6.3.3	Optimal Correlation with Known Signal Variance: r_q	183
6.4	Correlation Estimators for Quantized Signals	184
6.4.1	The Quantization Transfer Function	185
6.4.2	Quantized Correlation via Sample Covariance	185
6.4.3	The MLE of Correlation for Quantized Signals	185
6.4.4	Noise in the MLE and the Cramér-Rao Lower Bound	187
6.5	Examples	188
6.5.1	One-bit Quantization	188
6.5.2	Two-Bit Quantization	190
6.5.3	Many-Bit Quantization	192
6.6	Reductions for Small Correlation	194
6.7	Summary	196
6.8	Appendix: MLE for Unquantized Signals with Known Variance	198

Appendices **201**

A	An Extension and Application of Price’s Theorem	203
A.1	Extending Price’s Theorem	203
A.2	Example: Calculating the Bias in One-Bit Correlation	205
A.3	Evaluating Quadrant Integrals with Diagrams	205
B	Generalized Effects of Source Structure on the Modulation Index	208

List of Figures

2.1	PDF of intensity for different pulse averaging numbers $N = 1, 2, 100,$ and ∞ .	30
2.2	Exact PDF of intensity for $N = 2, 10,$ and $50,$ and the corresponding Gaussian, i.i.d., and gamma approximations.	34
2.3	PDF of intensity and the corresponding modification expected for an extended emission region, for $N = 1, 10,$ and $100.$	45
2.4	Intensity PDF and the corresponding modification for emission size effects, for $N = 1$ and varying gated signal-to-noise.	54
3.1	Characteristics of complex noise δV for snapshot visibilities.	81
3.2	Visibility projections as a function of baseline and signal-to-noise for $N = 1.$	86
3.3	Visibility projections $P(V_r)$ and $Q(V_r)$ for $N = 2, 10,$ and $50,$ and the corresponding errors δP and δQ in the Gaussian approximation for a moderate baseline.	88
3.4	Exact projections $P(V_r)$ and $Q(V_r)$ for $N = 1$ to demonstrate the broad scintillation-induced wings at large $ V_r .$	95
3.5	Visibility projections for a point source and their modifications corresponding to an elongated emission region. Modest averaging, $N = 10,$ reveals the W-shaped signature of emission size.	103
4.1	Observed and model PDFs of intensity for three degrees of averaging: $N = 1, 3,$ and $5.$	130
4.2	Observed and model PDFs of intensity with their corresponding residual structure; $N = 2.$ Three cases are plotted, corresponding to averaged pairs of intensities that are separated by $\Delta\tau = 1, 10,$ and 20 pulses. The residuals are concurrently fit to the decorrelation timescale and the dimensionless emission size.	132
4.3	Observed and model PDFs of intensity for the subsets of pulses in the top and bottom decile by pulse intensity with corresponding residual curves.	134

4.4	Inferred emission sizes of individual pulses as a function of their gated signal-to-noise.	136
5.1	The ensemble average and noise for average visibilities from simulations and from theory for a one-dimensional scattering screen. . . .	163
5.2	The distribution of refractive noise from simulations compared with the expected Rayleigh distribution.	169
6.1	Asymptotic noise in correlation estimators for unquantized signals.	181
6.2	Noise in estimates of correlation for signals quantized with two bits.	192
6.3	Noise in the MLE of correlation for quantized signals for various quantization levels. The noise is shown for both when the signal variance is known and when it is unknown.	194

Common Symbols and Abbreviations

Symbol	Definition
Abbreviations	
ACF	Autocorrelation function
CRB	Cramér-Rao bound
i.i.d.	Independent and identically distributed
ISM	Interstellar medium
MLE	Maximum-likelihood estimator
PDF	Probability density function
Observational Parameters	
λ	Observing wavelength
ν	Observing frequency
k	Observing wavenumber
B	Observing bandwidth
t_{obs}	Observing duration
\mathbf{b}	Interferometer baseline
\mathcal{B}	Scaled interferometer baseline $\mathcal{B} \equiv (1 + M)^{-1}\mathbf{b}$
Data Reduction	
N	Degree of temporal averaging
t_{acc}	Spectral accumulation time
Scintillation & Scattering Parameters	
D	Characteristic Earth-scattering distance
R	Characteristic source-scattering distance
M	Effective magnification of the scattering disk: $M \equiv D/R$
$D_\phi(\mathbf{x})$	Phase structure function of a scattering screen
r_{in}	Inner scale of the turbulent cascade
α	Power-law index of D_ϕ in the inertial range
r_0	Phase coherence length: $D_\phi(r_0) \equiv 1$
r_{d}	Diffractive scale: $r_{\text{d}} = \lambda/\theta$
r_{F}	Fresnel scale: $r_{\text{F}} = \sqrt{k^{-1}DR/(D+R)}$
r_{R}	Refractive scale: $r_{\text{R}} = r_{\text{F}}^2/r_0$
Σ	Characteristic linear scale of the scattering disk
$\Gamma(\Delta t, \Delta\nu)$	ACF of the scintillation pattern; we often fix Δt or $\Delta\nu$ implicitly
$\Delta\nu_{\text{d}}$	Characteristic bandwidth of diffractive scintillation
Δt_{d}	Characteristic timescale of diffractive scintillation
t_0	Pulse-broadening timescale
Source Characteristics	
R_{LC}	Light-cylinder radius
P_0	Pulsar rotational period
γ_{s}	Squared dimensionless characteristic size of the emission region
σ	Characteristic linear size of the emission region

Chapter 1

Introduction

In a nutshell, this dissertation explores the delicate interplay between the intrinsic and extrinsic physical processes related to pulsars, especially in how the latter (scintillation) can shed light on the former (the radio emission region). This work reflects the continuation of a rich history connecting these rather disparate physical regimes, including the fortuitous discovery of pulsars.

In this chapter, we outline this connection while introducing the basic concepts that underlie the work that follows. We first discuss the various manifestations of scintillation in astronomy, their physical mechanisms, and their relation to imaging. We then introduce pulsars and their special relationship to scintillation. Next, we discuss the nature of radio wave propagation in the interstellar plasma and the role of turbulence. Finally, we conclude with an overview of the subsequent chapters.

1.1 Scintillation

For the Air through which we look upon the Stars, is in a perpetual Tremor; as may be seen by the tremulous Motion of Shadows cast from high Towers, and by the twinkling of the fix'd Stars. But these Stars do not twinkle when viewed through Telescopes which have large apertures. For the Rays of Light which pass through divers parts of the aperture, tremble each of them apart, and by means of their various and sometimes contrary Tremors, fall at one and the same time upon different points in the bottom of the Eye, and their trembling Motions are too quick and confused to be perceived severally. And all these illuminated Points constitute one broad lucid Point, composed of those many trembling Points confusedly and insensibly mixed with one another by very short and swift Tremors, and thereby cause the Star to appear broader than it is, and without any trembling of the whole. Long Telescopes may cause Objects to appear brighter and larger than short ones can do, but they cannot be so formed as to take away that confusion of the Rays which arises from the Tremors of the Atmosphere.

Opticks
NEWTON

Newton was the first to recognize the twinkling of stars as a multipath propagation effect, now termed *scintillation*, and his prescient remarks foreshadowed the industry devoted to optical seeing. In addition, his comments on large apertures solve a related riddle – namely, why planets do not twinkle. For planets, the larger angular size superimposes slightly offset copies of the same diffractive pattern, which suppresses the variations (see, e.g., Narayan, 1993).

More explicitly, the phase variations across the scattering disk are coherent across the first Fresnel zone, with transverse scale $r_F \approx \sqrt{D/k}$, where D is the distance from the observer to the scattering material and k is the observing wavenumber. The additional phase from scattering weakly perturbs this coherence. Accordingly, a source size that exceeds r_F will quench the scintillation.

Yet, the Rayleigh criterion for our eyes suggests a diffraction-limited visual acuity of $1.22\lambda/D \approx 1.22(500 \text{ nm})/(5 \text{ mm}) \sim 1'$ – somewhat larger than the typical angular size of planets. Hence, the atmospheric scattering serves to *improve* the resolution of our eyes, which would not be able to distinguish the angular size of a star from a planet without it.

The outflowing plasma of the solar wind provides another astrophysical example of scintillation. This plasma scatters long radio wavelengths, leading to *interplanetary scintillation*, with behavior similar to the optical case (Hewish et al., 1964). Early radio astronomers quickly developed techniques to utilize this type of scintillation for source inference of quasars (Little & Hewish, 1966; Salpeter, 1967; Cohen et al., 1967).

The focus of this dissertation is *interstellar scintillation*, which arises from scattering in the tenuous interstellar plasma and affects sufficiently compact sources at radio wavelengths, as was first recognized by Scheuer (1968). This type of scintillation, however, is fundamentally different from the others. In this case, the phases incurred from scattering vary by many radians across the first Fresnel zone – the regime of “strong” scattering. Here, the size of a coherent patch, the phase coherence length r_0 , depends of the nature of the scattering material and can be orders of magnitude smaller than r_F .

Techniques such as speckle imaging or adaptive optics can potentially restore the performance of an instrument to its diffraction limit. Yet, the achievable an-

gular resolution $\sim r_0/D$ from interstellar scintillation can be orders of magnitude smaller than the diffraction limit of conventional instruments. Thus, a major focus of this dissertation is to derive precise metrics for this type of scintillation and to determine techniques that utilize the scattering for source inference. Because the results of this dissertation apply to the strong-scattering regime, “scintillation” will always imply interstellar scintillation.

1.2 Pulsars

The discovery of pulsars was one of the most unexpected and extraordinary findings in the history of astronomy. Antony Hewish had supervised construction of a new radio telescope operating at 81.5 MHz with a 1 MHz passband – an array of 1024 dipoles designed to study interplanetary scintillation (Hewish, 1975). Because of the rapid (~ 1 s) variations from scintillation, the new receiver employed a typical time constant of 0.1 s.

In fact, the unique role of scintillation in source inference was already in play. Although Martin Ryle had developed the aperture-synthesis technique and located several thousand radio galaxies, interplanetary scintillation afforded $0.1'' - 1''$ resolution – sufficient to determine which of these were quasars (Hewish et al., 1964; Little & Hewish, 1966).¹

¹In fact, Hewish and Ryle would later share the 1974 Nobel Prize in Physics for their respective work.

The telescope began operation in July of 1967. Hewish then assigned his graduate student Jocelyn Bell to analyze the pen-chart recordings for indications of radio interference; a source that persisted over a repetitive observing routine was unlikely to be spurious. She quickly noticed a regular pulsed anomaly, which appeared at a fixed right ascension and declination. Systematic observations confirmed the presence of this object – the first pulsar, B1919+21.

The phenomenal stability of pulsars was realized immediately, with the first publication reporting a period for B1919+21 of $P_0 = 1.3372795 \pm 0.0000020$ s (Hewish et al., 1968). Moreover, a lack of observed parallax, with an accuracy of $2'$, gave a source distance greater than 1000 AU. However, the origin of the pulsed radio emission was still uncertain.

Several potential mechanisms for the pulsed radiation were proposed, including a rotational pulsation from neutron stars. Indeed, Walter Baade and Fritz Zwicky had suggested the existence of neutron stars, their stability, and their association with supernovae more than 30 years prior, only two years after Chadwick's discovery of the neutron (Baade & Zwicky, 1934). Woltjer (1964) had even derived the correct magnetic field of a pulsar, inferred from conserved magnetic flux during stellar collapse, and Pacini (1967) discussed the resulting energetic output from a rotating neutron star; he even considered its potential role as a source of energy in the Crab nebula. Nevertheless, the powerful radio emission was unexpected, and the association of pulsars with neutron stars was only cemented by the discovery

of the much shorter period Vela (89 ms) and Crab (33 ms) pulsars, as well as the measured slowdown of the Crab pulsar, which identified a rotational, rather than vibrational, origin (Lyne & Graham-Smith, 1998).

1.3 Propagation Effects in the Ionized Interstellar Medium

Remarkably, the first pulsar publication also noted an aspect of the scattering material that pulsars are uniquely suited to probe: dispersion.² The following discussion will summarize the essential aspects of radio-wave scattering in the ionized interstellar medium and their relevance to the remainder of this dissertation.

Recall that the refractive index n of a dilute plasma is (e.g. Jackson, 1998)

$$n = \sqrt{1 - \frac{\nu_p^2}{\nu^2 (1 \pm \frac{\nu_B}{\nu})}}. \quad (1.1)$$

Here, the $+/-$ corresponds to left-/right-handed circularly polarized waves, ν_p is the plasma frequency and ν_B is the cyclotron frequency:³

$$\begin{aligned} \nu_p &= \sqrt{\frac{n_e e^2}{\pi m_e}} \approx 9.0 \times \sqrt{\frac{n_e}{1 \text{ cm}^{-3}}} \text{ kHz}, \\ \nu_B &= \frac{e B_{\parallel}}{2\pi m_e c} \approx 2.8 \times \left(\frac{B_{\parallel}}{1 \text{ } \mu\text{G}} \right) \text{ Hz}, \end{aligned} \quad (1.2)$$

²Actually, any intermittent or bursty signal can probe dispersion. For instance, gamma-ray burst afterglows might identify dispersion from the intergalactic medium (Ioka, 2003).

³We employ Gaussian units throughout this chapter.

where e , n_e , and m_e are the electron charge, number density, and mass, respectively. The phase velocity of the medium is $v_p = n^{-1}c$, while the group velocity is $v_g = nc$. For the ionized ISM, ν_p is $\sim\text{kHz}$ and ν_B is $\sim\text{Hz}$.

The plasma dispersion relation gives rise to three types of effects. First, the frequency dependence introduces dispersion – longer wavelengths are delayed relative to shorter ones. The dispersive delay Δt at a frequency ν depends on the integrated electron column density along the line of sight, typically expressed as a *dispersion measure* DM in units of pc/cm^3 : $\Delta t \approx 4 \times \text{DM} \times \nu_{\text{GHz}}^{-2}$ ms. The DM can be estimated by comparing pulse arrival times across sufficiently wide bandwidths. Moreover, measurements of DM among many lines of sight can then map the Galactic distribution of n_e (Taylor & Cordes, 1993; Cordes & Lazio, 2002). However, multiplication by an appropriate phase-only transfer function in the spectral domain can entirely remove dispersive effects, by simply unwrapping the frequency-dependent dispersive phase (Hankins, 1971). This process, known as coherent dedispersion, is now standard and straightforward, and we will, therefore, ignore dispersive effects for the remainder of this dissertation.

Second, Eq. 1.1 indicates that the ionized ISM is birefringent. While the relative delay between the circular polarizations is negligible, it introduces a gradual rotation of the polarization position angle: $\Delta\Psi = \text{RM} \times \lambda^2$, where the *rotation*

measure RM corresponds to (see, e.g., Lorimer & Kramer, 2004)

$$\text{RM} = \frac{e^3}{2\pi m_e^2 c^4} \int dl n_e B_{\parallel}. \quad (1.3)$$

An estimated RM, typically expressed in units of rad/m^2 , can be combined with the DM to estimate the mean parallel magnetic field along the line of sight: $\langle B_{\parallel} \rangle \approx 1.23 (\text{RM}/\text{DM}) \mu\text{G}$. However, similar to dispersion, Faraday rotation is straightforward to remove, using an appropriate filter, and is negligible over the extremely narrow scintillation bandwidths typical of observations that motivate the present work.

The third effect, scattering, is more subtle. Because the plasma frequency depends on n_e , inhomogeneities in the electron density scatter radio waves, leading to the interstellar scintillation discussed in §1.1. Pulsars provide many techniques for quantifying this scattering, including temporal broadening, angular broadening, and characteristic scales of the scintillation. In §1.3.1, we discuss the power spectrum of the density fluctuations. Then, in §1.3.2, we present qualitative details of the resulting scintillation.

1.3.1 The Spectrum of Electron Density Fluctuations in the ISM: a Turbulent Cascade?

At typical radio observing frequencies ν , we can simply write $n \approx 1 - \frac{1}{2} \frac{\nu_p^2}{\nu^2}$. Thus, the phase shift (i.e. the *screen phase*), relative to the average, of a light ray propagating through a thin screen with random density fluctuations is

$$\phi(\mathbf{x}) = k(n(\mathbf{x}) - \langle n(\mathbf{x}) \rangle)ct = -2\pi (\nu_p^2 - \langle \nu_p^2 \rangle) t\nu \propto \Delta n_e \nu. \quad (1.4)$$

Here, t is the timescale to cross the screen. The density fluctuations Δn_e are typically quantified by their resulting phase structure function:

$$D_\phi(\mathbf{x}) \equiv \left\langle [\phi(\mathbf{x} + \mathbf{x}') - \phi(\mathbf{x}')]^2 \right\rangle. \quad (1.5)$$

This function contains sufficient information when the phases form a statically-homogeneous Gaussian random field, as is expected whenever the screen thickness encompasses many independent phase irregularities of finite variance.

The phase structure function relates neatly to several observable quantities. For example, an observer samples elements of the diffraction pattern, and an interferometer calculates the complex two-point function of this pattern, called the *visibility*. For a scintillating point source, the variation of the average visibility $V(\mathbf{b})$ with the observing baseline determines the phase structure function of the

scattering medium: $V(\mathbf{b}) = \exp \left[-\frac{1}{2} D_\phi(\mathbf{b}/(1 + D/R)) \right]$, where D is the Earth-scatterer distance and R is the source-scatterer distance. For a spatially-extended emission region, the observed visibility is that of a point source multiplied by the Fourier transform of the source intensity distribution – the basis of aperture-synthesis imaging (Thompson et al., 2001). In Chapter 5, we will discuss the effects of scintillation on these relations.

An abundance of measurements indicate that the spectrum of density fluctuations is close to a power law on scales from 1000 km to scales exceeding 100 AU, suggestive of a turbulent cascade (e.g. Armstrong et al., 1995). In fact, the index of this power law appears to be close to the classical Kolmogorov value of $11/3$, which corresponds to incompressible hydrodynamic turbulence. However, the index is also close to 4, which would arise from a medium consisting of many scattering regions with abrupt boundaries (Lambert & Rickett, 1999).

For a turbulent cascade, the dissipation scale is of particular interest because the final mechanism for dissipation is intimately related to the magnetic field structure in the ISM. Theoretical expectations place the inner scale as small as ~ 100 km, reflecting the plasma microscales in the warm ionized medium – a significant challenge to probe observationally (Spangler & Gwinn, 1990). An inner scale set by the ion inertial length, for example, would be independent of the field strength but inversely proportional to the density of the scattering material. Al-

ternatively, an inner scale given by the ion Larmor radius is instead proportional to the square-root of temperature and inversely proportional to the magnetic field.

Pulsars are ideally suited to probe these small scales. For example, Lambert & Rickett (1999) demonstrated that the asymptotic behavior of the pulse-broadening decay is highly sensitive to the inner scale. To test this prediction, Rickett et al. (2009) analyzed the pulse profile of the strongly-scattered pulsar B1641-45 at 660 MHz and 2300 MHz; they estimated an inner scale in the range 70-100 km, assuming a Kolmogorov spectrum. They also noted that this value is quite sensitive to anisotropy of the scattering disk (which increases the inferred inner scale). Likewise, Smirnova & Shishov (2010) analyzed the pulse profile of B2111+46 at 112 MHz and 610 MHz and found that the data were consistent with an inner scale of 350 ± 150 km. Each of these measurements is broadly consistent with an inner scale determined by the ion inertial scale in localized, high density regions.

1.3.2 Diffractive and Refractive Branches of Scintillation

With a power-law structure function, the majority of scintillation occurs in two widely separated branches. Inhomogeneities on small scales wrinkle the wavefronts so that they interfere, resulting in *diffractive* scintillation, a rapid (\sim second) narrowband flickering of compact sources (Scheuer, 1968). Concurrently, inhomogeneities on larger scales deflect and focus radiation, giving rise to *refractive* scintillation, a weaker and slower (\sim month) wideband modulation (Rickett et al.,

1984; Rickett, 1990). While diffractive scintillation is quenched for sources exceeding the ~ 1000 km diffractive scale, refractive scintillation persists until source extents exceed the size of the scattering disk.

However, many observational and theoretical challenges remain for this simple prescription. For example, Stinebring et al. (2000) conducted daily flux density monitoring of 21 pulsars at 610 MHz for five years. They found that most pulsars showed good agreement with the anticipated variability from refractive effects. However, the Vela pulsar was one of six pulsars, termed “Super-Kolmogorov,” with markedly higher fluctuation in flux density than expected. Unfortunately, the flux density structure function did not appear to have sufficient information to discriminate between various mechanisms for boosting refractive power. Many other researches have noted similar excesses of refractive effects (e.g. Ramachandran et al., 2006; Bhat et al., 1999a,b). Hence, in Chapter 5, we develop new refractive metrics, which may help to identify the origin of these discrepancies.

1.4 Outline of Dissertation

In the subsequent chapters, we explore fundamental limits in radio astronomical observations of highly-scattered compact objects, and we develop techniques to recover precise information about both the source and the scattering. In Chapter 2, we analyze flux density statistics with a focus on spectral resolution at or near the Nyquist limit, and we show that the effects of an extended emission region

can be neatly isolated in this regime. Next, in Chapter 3, we extend these ideas to interferometric visibility. In Chapter 4, we then apply these techniques to analyze observations of the Vela pulsar at 760 MHz. In Chapter 5, we explore the effects of refractive scintillation on long baseline visibilities, and we show that studies of the resulting noise have many advantages relative to other refractive metrics. Finally, in Chapter 6, we examine the problem of maximizing the information gleaned from radio astronomical observations from an instrumental perspective and demonstrate that conventional methods are significantly sub-optimal for strong sources, such as pulsars.

Chapter 2

Flux-Density Statistics for a Scintillating Source

This chapter considers the flux density statistics of a scintillating source observed with spectral resolution at, or comparable to, the fundamental limit of the Nyquist theorem.¹ While this limit is of considerable interest from an information-theoretic perspective, we are also motivated by practical considerations. In particular, for the most heavily scattered pulsars at meter and decimeter wavelengths, the scintillation pattern can decorrelate over a bandwidth that is comparable to that of a single spectral channel. Equivalently and perhaps more intuitively, the pulse broadening $t_0 \propto \lambda^4$ can exceed the pulse duration.

However, we unexpectedly uncovered many attractive features enabled by these ultra-high-resolution statistics. As one example, Gwinn & Johnson (2011) demonstrated that intrinsic variability introduces correlations in spectral noise without modifying the mean spectrum. But, a single spectral sample is drawn from an exponential random variable, with a single degree of freedom (its scale).

¹This chapter is adapted from Johnson & Gwinn (2012).

Thus, since the mean spectrum is immune to intrinsic modulation, the statistics of an individual channel are as well. However, spectral averaging will introduce features that reflect the correlated spectral noise. Indeed, Gwinn et al. (2011) demonstrated that this property can identify intrinsic variability, regardless of dispersion or scattering.

Though typically viewed as a hindrance, the strong-scattering regime actually enables another simplification: the propagation acts to convolve the intrinsic signal with a stochastic kernel that takes the same form as the amplitude-modulated noise of the pulsar. Thus, the scattering in this regime follows an extremely general prescription, regardless of the nature or distribution of the scattering material.

In addition to incorporating the effects from scattering and intrinsic variability, we will also account for the possibility of a spatially-extended emission region. The AU-scale scattering disk acts analogously to a stochastic lens, with a corresponding resolution of several nanoarcseconds – sufficient to resolve a pulsar magnetosphere. Hence, with a precise understanding of the statistics involved, this scattering can be used to *improve* the achievable resolution (see §1.1). Longer observing wavelengths afford the highest resolution, but source noise quickly overwhelms the scintillation statistics.

In short, this chapter establishes a new analysis strategy to enable emission size inferences regardless of the scattering strength – this technique can even be applied

to single pulses. Moreover, both the noise and variability of the source are neatly decoupled from the scintillation, allowing a precise and confident determination of the signature of extended emission. In Chapter 4, we will apply these ideas and techniques to observations of the Vela pulsar at 760 MHz.

2.1 Introduction

2.1.1 Noise and Scintillation

Scintillation of compact astrophysical radio sources has proven to be a remarkable probe of both the turbulent interstellar plasma and the extreme conditions of the emission regions of these sources. This chapter is primarily motivated by observations of pulsars at meter and decimeter wavelengths, for which the AU-scale scattering resembles a stochastic “lens” with a potential resolving power of less than a nanoarcsecond. However, our results apply to any compact object that exhibits diffractive scintillation.

The emission and scattering physics involve the interaction and mixing of many random variables. At the heart is the amplitude-modulated noise emitted by the source (Rickett, 1975). Indeed, even the amplitude modulation is stochastic, with individual pulses showing complex broadband profile structures, from bursty microstructure to strong and often non-Gaussian pulse-to-pulse variations (Rickett et al., 1975; Cairns et al., 2001; Kramer et al., 2002). This emission then propagates through the dilute, turbulent plasma of the interstellar medium (ISM),

where it undergoes dispersion and Faraday rotation, in addition to being strongly scattered. Finally, an observer samples the electric field in the presence of additive background noise, which often dominates the signal. Furthermore, the statistics of this random process evolve as the Earth, pulsar, and ISM move relative to each other.

Since the size of the scattering disk (Σ) scales approximately as the square of the observing wavelength (λ), the angular resolution afforded by the scintillation is $\theta_{\text{diff}} \sim \lambda/\Sigma \propto \lambda^{-1}$. Thus, longer wavelengths permit superior resolving power. However, at longer wavelengths, each scintillation element contains far fewer samples because of the relatively smaller timescale ($\Delta t_{\text{d}} \propto \lambda^{-1}$) and bandwidth ($\Delta \nu_{\text{d}} \propto \lambda^{-4}$) of the scintillation pattern. It therefore becomes subtle to decouple the scintillation from the source and background noise.

To address these difficulties, we present analytical expressions for the probability density function (PDF) of intensity after arbitrary temporal averaging of the spectra. We describe the case when single-pulse spectra are formed and then are averaged in groups of N adjacent pulses; we exclusively use N to denote such temporal averaging. We account for the decorrelation of the scintillation pattern during this averaging and derive the resulting modification to the intensity PDF. We also account for spatially-extended source emission and show that the leading order PDF correction is identical, up to scale, to that of the decorrelation of the scintillation pattern within the averaging time. In addition, we demonstrate that

spatially-extended emission affects the measured PDF of intensity, even in the limit of $N = 1$ averaged spectra. This feature presents the remarkable opportunity of measuring the emitting region sizes for individual pulses, or of subclasses of pulses.

The sources and variety of noise are diverse, stemming from the background noise and the amplitude-modulated noise emitted by the source. Measured quantities such as intensity then correspond to random variables, and their stochastic variation introduces additional noise. Applied to the source, this noise is the familiar *self-noise* (Dicke, 1946; Kulkarni, 1989; Zmuidzinas, 2003; Gwinn & Johnson, 2011), but the background and scintillation parameters have similar limitations. Such noise is generally unbiased and scales with intensity. Our derivations fully account for all these types of noise. We also account for artifacts arising from instrumental limitations, such as quantization of the analog signal and quadrature downconversion. These types of effects introduce additional noise as well as bias and distortion.

To supplement our calculated PDFs, we also analyze expressions based on the moments of the distributions. In particular, we extend the modulation index, a traditional estimator of source emission geometry, to include the effects of self-noise and pulsar amplitude variations, and we analyze a technique that estimates self-noise. Our expressions refine these simple tools for intrinsic emission inference.

2.1.2 Strategy for Comparison with Observations

An observation well-suited for comparison with our models has an observing bandwidth $B \gg \Delta\nu_d$, an observation duration $t_{\text{obs}} \gg \Delta t_d$, and a spectral accumulation time much longer than the pulse-broadening timescale. For each pulse period, the on-pulse and off-pulse regions yield estimates of the signal and noise intensities, respectively. These estimated parameters fully define a model of the intensity PDF (see §2.3), which is readily compared with a histogram of the measured data.

The residual structure in this comparison contains information about the spatial extent of the emission region and the evolution of the scintillation pattern, as well as artifacts from instrumental limitations and errors in the estimated on-pulse and off-pulse intensities. The on-pulse and off-pulse averages once again parametrize a model for this residual structure (see §2.4), which is quantified by a single fitted parameter for amplitude. This fitted parameter yields the transverse size of the emission region, if the scattering geometry is specified.

2.1.3 Comparison with Previous Work

Most past work has focused on the regime of many samples of the spectrum averaged together: $N \rightarrow \infty$. For such data, the effects of noise can be approximated as Gaussian. Gwinn et al. (1998) gave the expected distribution of intensity for a strongly scintillating source, including the effects of a spatially-extended emission

region. Gwinn et al. (2000) extended these forms to account for Gaussian self-noise at small intensity, and estimated the contributions of averaging in time and frequency by deriving their effects on the modulation index. In an unpublished manuscript, Cordes (2000) presented expressions for the PDF of scintillation gain in terms of a Karhunen-Loève expansion with the coefficients defined by a Fredholm equation, and suggested approximate forms determined by χ^2 distributions with the appropriate number of degrees of freedom. Gwinn (2001) gave the distribution of interferometric visibility for a pointlike or extended source in strong scintillation. Gwinn et al. (2011) presented expressions for self-noise, suitable for large N .

The present work focuses on the complementary regime of single spectral realizations, and averages of N such spectra. We connect with these previous works through the asymptotic forms of our distributions. Similarly, van Straten (2009) analyzed statistics of Stokes parameters when $N = 1$ and showed, for instance, that the degree of polarization is undefined in this case. His results describe the high signal-to-noise regime with no effects of propagation or source emission structure, as appropriate for the high-frequency observations of giant pulses from the Crab pulsar that motivated his work (Hankins et al., 2003).

2.1.4 Outline of Chapter

In §2.2, we briefly review the theoretical descriptions of pulsar emission and interstellar scintillation, and establish our assumptions about each. Then, in §2.3, we present an expression for the exact intensity PDF of a scintillating point source, as well as useful approximations. We next apply these approximations in §2.4 to estimate modifications to the PDF arising from the decorrelation of the scintillation pattern within the averaging time, effects of finite source emission size, and observational constraints such as finite scintillation averages; we then use these expressions to derive the limiting resolution for emission size inference. In §2.5, we derive the modulation index and analyze a technique that identifies self-noise. Finally, in §2.6, we summarize our results and outline the prospects for pulsar observations.

2.2 Theoretical Background

2.2.1 Pulsar Radio Emission

Pulsar radio emission is thought to arise from coherent curvature radiation from a relativistic electron-positron plasma, flowing outward along open field lines from the stellar surface to the light cylinder. Charge acceleration occurs in a “gap” of depleted charge density where the force-free state cannot be maintained. Such sites initiate a pair-production cascade, which forms a secondary plasma (Sturrock,

1971; Ruderman & Sutherland, 1975). This secondary plasma generates the radio emission, which is then beamed, ducted, and refracted as it propagates through the upper magnetosphere (Barnard & Arons, 1986; Arons & Barnard, 1986; Lyutikov & Parikh, 2000). The gap may be located close to the polar cap region (the “polar gap”) (Arons & Scharlemann, 1979), or along the boundary of the open and closed field lines (the “slot gap”) (Arons, 1983). An “outer gap” (Cheng et al., 1986; Romani, 1996), situated close to the light cylinder radius, is the favored site for much high-energy emission and may also contribute to the radio emission. Differing locations of the gap may be responsible for some of the emission variety between pulsars.

The superposition of many independent radiators produces white Gaussian noise. Thus, although the radio emission process is fundamentally coherent, by groups of many particles, the bulk emission may still be effectively spatially and temporally incoherent. Intrinsic physical processes (and the pulsar’s rotation) then modulate the envelope of this random field, motivating an “amplitude-modulated noise” description of the emission (Rickett, 1975). Our results assume this type of emission, confined to a region that is a small fraction of the diffractive scale $r_d \equiv \lambda D / (2\pi\Sigma) \sim 10^6$ m, where D is the characteristic Earth-scatterer distance.

2.2.2 Interstellar Scattering

Density inhomogeneities in the dilute, turbulent plasma of the ISM scatter the radio emission, leading to multipath propagation. For most pulsars observed at decimeter wavelengths, the phases between pairs of paths differ by many turns and are therefore uncorrelated; this is the regime of “strong” scattering. Equivalently, the diffractive scale is much smaller than the Fresnel scale, $r_F \equiv \sqrt{\lambda D} \sim 10^9$ m.

In general, the timescale for the evolution of the diffraction pattern at the observer ranges from seconds to hours, and so is effectively static over the scattering timescale. In this case, the effect of scattering is to convolve the pulsar signal with a “propagation kernel.” The characteristic width of the average propagation kernel is the pulse-broadening timescale t_0 . Dispersion contributes an additional frequency-dependent delay that is readily reversed (Hankins, 1971). The motivation and limitations of approximating scattering as a convolution are given in much greater detail by Gwinn & Johnson (2011).

Although this picture of strong scattering of a point source is quite general, a description of the effects of a spatially-extended emission region requires specification of the scattering geometry. We present explicit results for the case of thin-screen scattering, as is observationally motivated (Williamson, 1972; Komesaroff et al., 1972; Hill et al., 2005). We give additional reductions by assuming a square-law phase structure function; the generalization to Kolmogorov or other-

wise is straightforward and changes only the scale of the PDF modifications that we derive.

2.2.3 Instrumental and Observational Requirements

In practice, spectra must be formed over a finite accumulation time t_{acc} ; the convolution representation of scattering requires $t_{\text{acc}} \gg t_0$ (see Gwinn & Johnson (2011) for additional details). The unique nature of pulsars and their generally short duty cycles allow a particularly elegant limiting option: the formation of single-pulse spectra that contain *all* pulsed power. Our descriptions are exact in this limit, and appropriate whenever $t_{\text{acc}} \gg t_0$.

We assume that such spectra are formed and then averaged in groups of N adjacent pulses. We also assume that the averaging timescale is much shorter than the scintillation timescale – the “snapshot image” of Narayan & Goodman (1989) – which subsumes the much weaker condition that the scattering material is approximately static during the accumulation of a single spectrum.

Frequency averaging is analogous but inherits additional information from non-stationary signals. The intrinsic pulse shape incurs spectral mixing via its associated frequency-domain convolution; the average is then of correlated intensities (see §2.7.2.2). Thus, a description of frequency averaging requires the specification of individual pulse profiles, whereas a description of temporal averaging requires only the phase-averaged source intensity for each pulse.

Lastly, we assume that the data explore a large representation of the full ensemble of diffractive scintillation: $(B/\Delta\nu_d) \times (t_{\text{obs}}/\Delta t_d) \gg 1$. Comparison with observations is most powerful if the stronger condition $B \gg \Delta\nu_d$ is satisfied so that the intrinsic amplitudes of individual pulses can be estimated.

2.2.4 Notation

Despite the number and variety of random variables involved in the emission and scattering processes, much statistical homogeneity exists; our notation highlights this foundational uniformity. We use z_x to denote a circular complex Gaussian random variable with unit variance, indexed by x . Some common examples of such variates are a single realization of the scalar electric field or the complex gain from propagation. The PDF of z_x is exponential in its squared norm, $P(z_x) = \pi^{-1}e^{-|z_x|^2}$, with respect to the standard complex metric $d\text{Re}[z_x]d\text{Im}[z_x]$. This norm is implicit for all PDFs presented with respect to complex random variables.

We also encounter many exponential random variables, usually in connection with a scintillation “gain,” which are thus denoted G or G_i , with $P(G) = e^{-G}$ for $G > 0$. Note that we use $P()$ to generically denote a PDF with respect to the given variables and parameters, as in the previous examples.

2.3 Distribution of Intensity

We now derive the expected PDF of intensity when the spectra are averaged over groups of N consecutive pulses. We assume that the scintillation pattern is frozen during each average, and that the source emission is pointlike. In §2.4, we relax these assumptions and discuss practical limitations. Our results apply to scalar electric fields that have been baseband shifted and coherently dedispersed.

We first derive an exact expression for the PDF of intensity in §2.3.1. However, for $N > 1$ this expression has a removable singularity at the origin and is analytically burdensome. These features motivate various alternatives, such as the *i.i.d. approximation* and the *gamma approximation*, which we derive in the following §2.3.2.1 and §2.3.2.2, respectively. We present a traditional representation, the *Gaussian approximation*, in §2.3.2.3 for comparison. Both the i.i.d. and gamma approximations are simple and powerful, and we heavily utilize them for the remainder of the chapter.

2.3.1 The Exact Intensity PDF

The pulsar emits white Gaussian noise ϵ_i , modulated by a time-varying envelope $\sqrt{I_s}f_i$. Here, I_s is a constant characteristic scale of the source intensity, ϵ_i is normalized to have unit variance, and the modulation f_i is power-preserving. To account for pulse-to-pulse variations in the phase-averaged flux density, we also

include a dimensionless pulse amplitude factor A_j , where j indexes the spectrum (i.e. the pulse number). We require no assumptions about the timescale of variability of the envelope f_i or the nature of the pulse-to-pulse variations A_j . Our treatment therefore accommodates arbitrary variability of the pulsar, such as the possibility of correlated pulse-to-pulse variations, log-normal amplitude statistics, or nanosecond-scale bursts, which merely modulates the Gaussian self-noise.

The propagation then acts to convolve this intrinsic emission with a scattering kernel, as discussed in §2.2.2. The kernel similarly consists of a power-preserving envelope g_i that modulates white Gaussian noise η_i of unit variance. The propagated signal is then superimposed with the background noise $\sqrt{I_n}\beta_i$, where I_n is the amplitude of the noise, and β_i is white Gaussian noise of unit variance. We assume that the background noise level is effectively constant over the averaging time, although this restriction is easily relaxed.

The observed scalar electric-field time series x_i and its Fourier-conjugate spectrum are thus given by

$$\begin{aligned}
 x_i &= \sqrt{A_j I_s} [(f\epsilon) * (g\eta)]_i + \sqrt{I_n}\beta_i \\
 \Rightarrow \tilde{x}_i &= \sqrt{A_j I_s} (\tilde{f} * \tilde{\epsilon})_i (\tilde{g} * \tilde{\eta})_i + \sqrt{I_n}\tilde{\beta}_i.
 \end{aligned}
 \tag{2.1}$$

Here, we denote Fourier conjugate variables with a tilde. In short, this equation describes the amplitude-modulated noise of the pulsar ($\sqrt{I_s}f_i\epsilon_i$) convolved with the stochastic propagation kernel ($g_i\eta_i$) and added to background noise ($\sqrt{I_n}\beta_i$).

Conventionally, these terms are labeled by their noise-free limits: the pulse profile $|f_i|^2$, pulse-broadening function $|g_i|^2$, gated signal I_s , and background I_n .

Of course, $\tilde{\epsilon}_i$, $\tilde{\eta}_i$, and $\tilde{\beta}_i$ are mutually independent (circular complex Gaussian) white noise. We see that a single spectral sample \tilde{x}_i is of the form $\sqrt{A_j I_s} z_f z_g + \sqrt{I_n} z_b$, where z_f , z_g , and z_b are each circular complex Gaussian random variables with unit variance. If the scintillation is held fixed (i.e. $z_g = \text{const.}$), then the intensity $|\tilde{x}_i|^2$ is drawn from an exponential distribution with scale $\bar{I}_j \equiv A_j I_s |z_g|^2 + I_n$. The PDF of the average of N such intensities is then given by Eq. 2.31:

$$\begin{aligned}
 P(I; N | z_g) &= N \sum_{j=1}^N \left(\frac{\bar{I}_j^{N-2}}{\prod_{\substack{\ell=1 \\ \ell \neq j}}^N (\bar{I}_j - \bar{I}_\ell)} \right) e^{-NI/\bar{I}_j} \\
 &= \frac{N}{(I_s |z_g|^2)^{N-1}} \sum_{j=1}^N \frac{(A_j I_s |z_g|^2 + I_n)^{N-2}}{\prod_{\substack{\ell=1 \\ \ell \neq j}}^N (A_j - A_\ell)} e^{-\frac{NI}{(A_j I_s |z_g|^2 + I_n)}}.
 \end{aligned} \tag{2.2}$$

Observe that when we designate N as a distribution parameter, we implicitly include the background I_n and source amplitudes $\{A_j I_s\}$.

All that remains is to incorporate the distribution of the scintillation random variable z_g . We assume that z_g explores a representation of the full diffractive ensemble. We introduce a ‘scintillation gain’ parameter $G \equiv |z_g|^2$, so $P(G) = e^{-G}$. Integrating the scintillation ensemble through G then provides the PDF of

intensity:

$$P(I; N) = N \int_0^\infty dG \frac{e^{-G}}{(I_s G)^{N-1}} \sum_{j=1}^N \frac{(A_j I_s G + I_n)^{N-2}}{\prod_{\substack{\ell=1 \\ \ell \neq j}}^N (A_j - A_\ell)} e^{-\frac{NI}{A_j I_s G + I_n}}. \quad (2.3)$$

This equation gives the expected PDF of intensity for the average of N pulses with amplitudes $\{I_s A_i\}$ and fixed scintillation, in the presence of white background noise with mean intensity I_n , if the spectra explore a representative ensemble of diffractive scintillation. Examples of this distribution for various N are shown in Figure 2.1.

Numerical evaluation of the PDF can be challenging because of the singularity at $G = 0$, although the integrand is not divergent. To address this difficulty, we employ variable-precision arithmetic libraries; the additional precision is essential for $N \gtrsim 10$.

2.3.2 Approximating the Intensity PDF

Although we have derived the exact expression for the intensity PDF (Eq. 2.3), we now derive several useful approximations. These approximations resolve the singularity at $G = 0$, uncover the $N \rightarrow \infty$ behavior, and present a simplified framework for deriving and interpreting perturbations of the PDF arising from effects such as a finite size of the emission region, decorrelation of the scintillation pattern within the averaging time, and errors in model parameters.

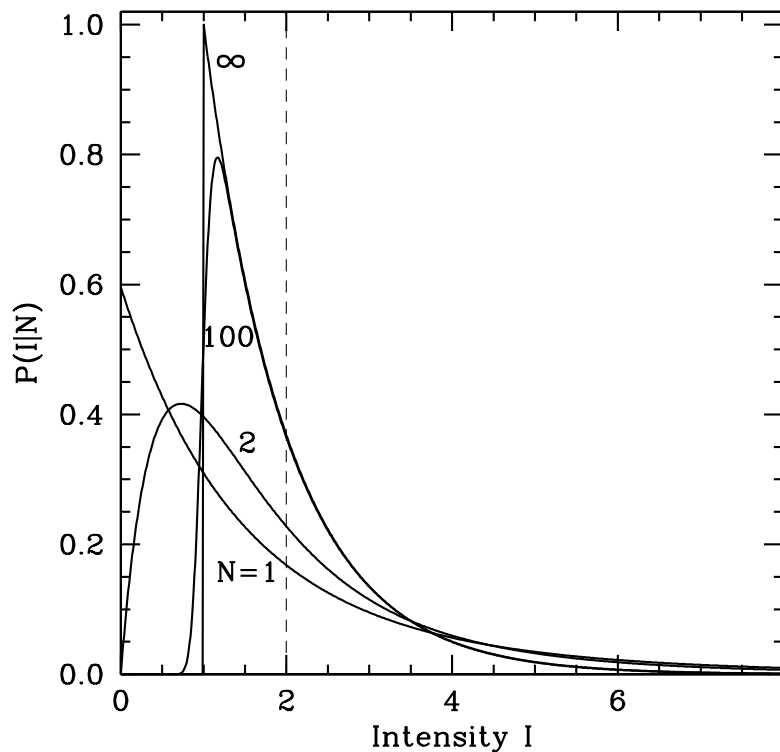


Figure 2.1: PDF of intensity for different pulse averaging numbers $N = 1, 2, 100,$ and ∞ . The source and background intensities are unity, as are all the pulse amplitude factors A_j ; the dashed line denotes the mean of 2.0. Because of the pulse amplitude degeneracy, the i.i.d. representation (Eq. 2.4) must be used (and is exact).

2.3.2.1 The i.i.d. Approximation

We derive our first approximation by replacing each set of N pulse amplitude factors A_j by its average $A \equiv \langle A_j \rangle$. This replacement simplifies the statistics because the intensities that are averaged under such assumptions are independent and identically distributed (i.i.d.); thus, we refer to this approximation scheme as the *i.i.d. approximation*.

We emphasize that the i.i.d. approximation does not ignore amplitude variability of the pulsar, but does reduce the variability to a moving average. The

difference is critical because, for example, the i.i.d. approximation is exact when $N = 1$.

After substituting the local amplitude average A , the PDF of intensity during a fixed scintillation gain G (i.e. Eq. 2.2) is given by an Erlang distribution (Eq. 2.32):

$$P(I; N|G) = \frac{N^N}{(N-1)!} \frac{I^{N-1}}{(AI_s G + I_n)^N} e^{-\frac{NI}{AI_s G + I_n}}. \quad (2.4)$$

As for Eq. 2.3, the scintillation ensemble can then be included via its exponential density: $P(I; N) = \int_0^\infty dG e^{-G} P(I; N|G)$.

2.3.2.2 The Gamma Approximation

We now extend the i.i.d. approximation to partially account for the effects of variation in the pulse amplitudes A_j within sets of N pulses. To achieve this extension, we replace N in Eq. 2.4 by an effective number of degrees of freedom N_{eff} , chosen such that the mean and variance match those of the exact PDF. Because N_{eff} is not necessarily an integer, the factorial in the Erlang distribution must be replaced by a gamma function; this modified form is the gamma distribution. The mean and variance of this gamma distribution are

$$\begin{aligned} \mu_{\text{gamma}} &= AI_s G + I_n, \\ \sigma_{\text{gamma}}^2 &= \frac{(AI_s G + I_n)^2}{N_{\text{eff}}}. \end{aligned} \quad (2.5)$$

For the exact distribution, given by Eq. 2.2, the mean is simply the average of the marginal means, and the variance is the average of the marginal variances, divided by N :

$$\begin{aligned}\mu_{\text{exact}} &= \frac{1}{N} \sum_{j=1}^N (A_j I_s G + I_n), \\ \sigma_{\text{exact}}^2 &= \frac{1}{N^2} \sum_{j=1}^N (A_j I_s G + I_n)^2.\end{aligned}\tag{2.6}$$

Matching Eq. 2.5 and Eq. 2.6 gives the correspondence appropriate for the gamma distribution:

$$\begin{aligned}A &= \frac{1}{N} \sum_j A_j, \\ N_{\text{eff}} &= \frac{\left(\sum_{j=1}^N 1 + A_j I_s G / I_n\right)^2}{\sum_{j=1}^N (1 + A_j I_s G / I_n)^2} \leq N.\end{aligned}\tag{2.7}$$

The scintillation ensemble is again included via integration over G with its exponential weight.

We refer to this extension of the i.i.d. approximation as the *gamma approximation*. The gamma approximation partially accounts for the pulse-to-pulse variability, and substantially improves the i.i.d. approximation for $N \gg 1$.

2.3.2.3 The Gaussian Approximation

By the Central Limit Theorem, Eq. 2.4 approaches a Gaussian distribution as $N \rightarrow \infty$, with mean $\bar{I} = AI_sG + I_n$ and variance $\delta I^2 = (AI_sG + I_n)^2/N = \bar{I}^2/N$. Accounting for the amplitude variations that are ignored by the i.i.d. approximation gives the generalized form, $\delta I^2 = \left[\bar{I}^2 + 2(\bar{I} - I_n)^2 \frac{\delta A^2}{\langle A \rangle^2} \right] / N$; i.e. pulse-to-pulse amplitude variations contribute twice their variance to the source self-noise. These relationships both reflect the familiar fact that self-noise is inversely proportional to the number of averaged samples N (Dicke, 1946).

A traditional approximation strategy replaces $P(I; N|G)$ with this matched Gaussian distribution; we refer to this scheme as the *Gaussian approximation*.

2.3.3 Utility of Approximations

These three approximations are particularly useful because they reduce the $N + 1$ degrees of freedom in a single averaged spectra to three: an overall scale partitioned into source and background contributions, and a measure of the averaging. In fact, the i.i.d. approximation has only two degrees of freedom because the degree of averaging is N ; this reduction comes at the expense of ignoring pulse amplitude variance.

Figure 2.2 demonstrates the relative quality of these three approximations in the presence of substantial amplitude variations. The Gaussian approximation is inferior to both the i.i.d. and gamma approximations, particularly for small N ;

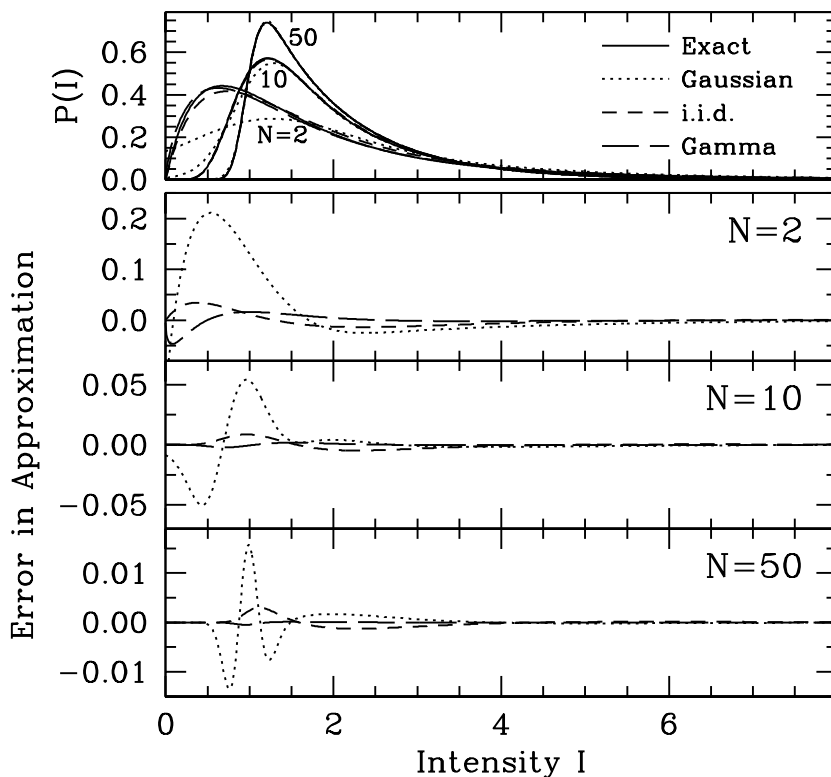


Figure 2.2: Exact PDF of intensity for $N=2$, 10, and 50, and the three approximations discussed in §2.3.2. The source and background intensities are unity, and the N pulse amplitude factors are uniformly distributed between 0 and 2.

indeed, the Gaussian approximation includes nonzero probability for negative intensities. The i.i.d. and gamma approximations, on the other hand, give excellent representations for arbitrary N and are much easier to implement numerically than the exact representation of Eq. 2.3, particularly for large N .

Our principal use of these approximations is to derive analytical estimates for PDF modifications arising from effects such as finite emission size and decorrelation of the scintillation pattern within the averaging time. We favor the relatively simple i.i.d. approximation for this purpose. While the small errors in the approximations might be significant in some measured PDFs, we expect the similarly

small errors on the expected $\lesssim 1\%$ PDF modifications to be negligible. Furthermore, the most intriguing degree of averaging is $N = 1$, which allows single-pulse studies and complete decoupling of emission size from decorrelation; both the i.i.d. and gamma approximations are, of course, exact for this case.

We therefore recommend the exact representation for PDF comparisons (or the gamma approximation if its accuracy suffices), and now derive PDF modifications using the i.i.d. approximation.

2.4 PDF Modifications

We now analyze effects that modify the PDF of intensity relative to the form derived in §2.3. Modifications can arise from physical processes both intrinsic and extrinsic to the source, as well as from instrumental effects. Since the model PDF of intensity of §2.3 depends only on direct observables (the average on-pulse and off-pulse intensities), the residual structure in a measured distribution relative to the corresponding model reflects these modifications. We also analyze the consequences of errors in the model parameters.

We find degeneracies among these many types of effects. Many of these degeneracies can be resolved by varying the degree of averaging N or the bandwidth used to construct the PDFs. We quantify the significance of each effect in terms of its expected bias on the inferred emission size γ_s and give strategies for identifying each source of bias.

However, despite the nearly identical form resulting from these varied effects, the derivation for each is unique. First, we account for decorrelation of the scintillation pattern within the averaging time in §2.4.1. Then, we derive the effects of spatially-extended source emission in §2.4.2. These two effects are degenerate, to excellent approximation, and we analyze their relative strength in §2.4.3. Next, we calculate the consequences of both noise and bias in the model parameters in §2.4.4, and we estimate the influence of instrumental distortion in §2.4.5. Finally, we derive the expected spatial resolution afforded by these scintillation statistics in §2.4.6.

2.4.1 Effects of Temporal Decorrelation

The scintillation pattern slowly evolves in response to the relative motions of the Earth, pulsar, and scattering medium, thereby affecting statistics of averaged intensities. We now derive the effects of this evolution on the observed distribution of intensity, in terms of the temporal autocorrelation function of the observed scintillation pattern.

Although the scintillation pattern evolves somewhat similarly with frequency, the effects of frequency averaging fundamentally differ from those of temporal averaging. Namely, for temporal averaging, the intensities within each average are independent, with correlated scales (i.e. the respective scintillation gains); whereas for frequency averaging, both the intensities within each average *and*

their scales can be correlated because of the intrinsic amplitude modulation. As noted in §2.2.3, spectral statistics after frequency averaging depend on individual pulse profiles, whereas spectral statistics after temporal averaging only depend on the phase-averaged flux densities.

Procedurally, we must index the scintillation factors G by pulse number. The resulting set $\{G_i\}$ is then a collection of correlated exponential random variables, with covariance determined by the autocorrelation function of the measured dynamic spectrum:

$$\begin{aligned}\Gamma_{ij} &\equiv \langle G_i G_j \rangle - 1 \\ &= \frac{\langle [I(t, \nu) - I_n] [I(t + \Delta t_{ij}, \nu) - I_n] \rangle}{\langle I(t, \nu) - I_n \rangle^2} - 1.\end{aligned}\tag{2.8}$$

Details of this type of multivariate exponential distribution are given in Appendix 2.7.2.

In the “snapshot image” regime, the averaging timescale is much shorter than the decorrelation timescale of the scintillation pattern, so $\Gamma_{ij} \approx 1$. The leading order decorrelation effects in $(1 - \Gamma_{ij})$ then provide an excellent approximation. Using Eq. 2.35, we obtain

$$\begin{aligned}P(I; N, \{\Gamma_{ij}\}) - P(I; N) \\ \approx - \sum_{i < j} (1 - \Gamma_{ij}) \int_0^\infty dG G e^{-G} \left. \frac{\partial^2 P(I; N | \{G_i\})}{\partial G_i \partial G_j} \right|_G.\end{aligned}\tag{2.9}$$

Note that the partial derivatives are easily evaluated using the characteristic function of $P(I; N|\{G_i\})$: $\varphi(k) = \prod_{\ell} (1 - i\bar{I}_{\ell}k/N)^{-1}$, where $\bar{I}_{\ell} \equiv A_j I_s G_j + I_n$. For example, applying the i.i.d. approximation ($A_j \equiv A$) yields the following relationship:

$$\left. \frac{\partial^2 P(I; N|\{G_i\})}{\partial G_i \partial G_j} \right|_G = \frac{1}{N(N+1)} \frac{\partial^2 P(I; N|G)}{\partial G^2}. \quad (2.10)$$

We can also reduce the sum over Γ_{ij} in Eq. 2.9 by approximating the evolution of the scintillation pattern as relative motion of the pulsar and observer with respect to a “frozen” random screen. The decorrelation in time is then simply expressed in terms of the phase structure function of the scattering medium (Goodman, 1985; Cornwell et al., 1989). For example, a square-law phase structure function has $\Gamma_{ij} = \exp[-(\Delta t_{ij}/\Delta t_d)^2]$, even in the presence of axial anisotropy (Rickett, 1977; Johnson et al., 2013b). If the averaging timescale is much less than the decorrelation timescale, then $\sum_{i<j} (1 - \Gamma_{ij}) \approx N^2 (N^2 - 1) / (12\Delta\tau_d^2)$, where $\Delta\tau_d$ is the decorrelation timescale in pulse periods. The quartic dependence on N leads to a rapid onset of decorrelation artifacts in the observed PDF after only modest averaging.

Combining this approximation for the decorrelation behavior with the general form for the PDF modification (Eq. 2.9), and applying the reduction afforded by

the i.i.d. approximation (Eq. 2.10) then provides the following estimate:

$$\begin{aligned}
 & P(I; N, \{\Gamma_{ij}\}) - P(I; N) \\
 & \approx - \frac{N(N-1)}{12\Delta\tau_d^2} \int_0^\infty dG G e^{-G} \frac{\partial^2 P(I; N|G)}{\partial G^2}.
 \end{aligned}
 \tag{2.11}$$

2.4.2 Effects of Extended Source Emission

A spatially-extended emission region smoothes the fluctuations from scintillation by superimposing many slightly offset copies of the diffraction pattern at the observer. In fact, extended source emission is merely one example in a broad class of physical effects that alter the distribution of scintillation gain. Other possibilities arise from modified scattering assumptions, such as weak scintillation or Lévy-type scattering statistics (Boldyrev & Gwinn, 2003). To account for these cases, we introduce a generalized scintillation gain random variable \mathcal{G} , which is no longer constrained to follow exponential statistics. Specification of $P(\mathcal{G})$, combined with $P(I; N|\mathcal{G})$ given by Eq. 2.3, then provides the intensity PDF $P(I; N)$.

Gwinn et al. (1998) examined $P(\mathcal{G})$ for thin-screen scattering of a Gaussian distribution of source intensity. They demonstrated that, if the source emission region is small relative to the magnified diffractive scale, \mathcal{G} is well-approximated by the convolution of three independent exponential random variables. The scales of these random variables reflect the size of the emission region. Gwinn (2001) derived an analogous result for interferometric visibility.

By extending the description of §2.3.1, we now demonstrate that an equivalent form arises for any spatially-incoherent, compact emission region in strong scattering. We parametrize the transverse coordinates of the source by \mathbf{s} . Each emitting location has independent source noise, and the emission envelope at each location may also vary. However, the propagation kernel is correlated over the emission region. A single spectral sample thus takes the form

$$\tilde{x}_i = \left\{ \int d^2\mathbf{s} \sqrt{A(\mathbf{s})I_s} z_f(\mathbf{s}) z_g(\mathbf{s}) \right\} + \sqrt{I_n} z_b. \quad (2.12)$$

We specify our source coordinates, \mathbf{s} , to be centered on the spatial mean of source intensity: $\int d^2\mathbf{s} \mathbf{s} A(\mathbf{s}) = \mathbf{0}$.

If the emission is confined to a small fraction of the magnified diffractive scale, then the scintillation random variable, $z_g(\mathbf{s})$, will be strongly correlated over the region of source intensity. We therefore expand to linear order: $z_g(\mathbf{s}) \approx z_g(\mathbf{0}) + (\mathbf{s} \cdot \nabla) z_g|_{s=0}$. The source term in Eq. 2.12 is then a convolution of three complex Gaussian random variables. Because of our choice of origin for \mathbf{s} , these three random variables are mutually uncorrelated during a fixed scintillation pattern. The marginal variances therefore add to give \mathcal{G} (up to overall normalization). In addition, the scintillation random variable, $z_g(\mathbf{s})$, is uncorrelated with its spatial derivatives, so the scales of the three variances are mutually independent. Thus,

\mathcal{G} is the convolution of three independent exponential random variables:

$$\mathcal{G} \equiv \frac{1}{1 + \gamma_{s,1} + \gamma_{s,2}} (G + \gamma_{s,1}G_1 + \gamma_{s,2}G_2). \quad (2.13)$$

The dimensionless subsidiary scales $\gamma_{s,i} \ll 1$ contain information about the transverse extent of the source emission. The scaling prefactor is merely chosen so that $\langle \mathcal{G} \rangle = 1$ and could equally well be absorbed into the definition of source intensity.

Using the results of Gwinn et al. (1998), we now explicitly relate the parameters $\gamma_{s,i}$ to the emission geometry by assuming a Gaussian distribution of source intensity and thin-screen scattering. In this case, the $\gamma_{s,i}$ give the squared size of the source in orthogonal directions \hat{x}_i , in units of the magnified diffractive scale:

$$\gamma_{s,i} = \left(\frac{D}{R} \frac{\sigma_i}{\frac{1}{2\pi} \frac{\lambda}{\theta_i}} \right)^2. \quad (2.14)$$

Here, D is the characteristic observer-scatterer distance, R is the characteristic source-scatterer distance, λ is the observing wavelength, θ_i is the angular size of the scattering disk along \hat{x}_i , and σ_i is the standard deviation of the distribution of source intensity along \hat{x}_i . This representation accommodates anisotropy of both the source emission and the scattering. If the source emission arises from a circular Gaussian intensity profile, then the FWHM of the emission region is $2\sqrt{\ln 4}\sigma \approx 2.35\sigma$, where $\sigma \equiv \sigma_i$.

Efforts to infer emission size often attempt to isolate the distribution $P(\mathcal{G})$ through sufficient spectral averaging; the modulation index m then quantifies the effects of emission size on this distribution (Salpeter, 1967; Cohen et al., 1967; Gwinn et al., 1998):

$$\begin{aligned} m^2 &= \frac{\langle \mathcal{G}^2 \rangle}{\langle \mathcal{G} \rangle^2} - 1 \\ &= \frac{1 + \gamma_{s,1}^2 + \gamma_{s,2}^2}{(1 + \gamma_{s,1} + \gamma_{s,2})^2} \approx 1 - 2(\gamma_{s,1} + \gamma_{s,2}). \end{aligned} \quad (2.15)$$

In §2.5.1, we discuss the modulation index in depth and extend Eq. 2.15 to account for the effects of self-noise, temporal decorrelation within the averaging time, and pulsar amplitude variability.

To determine the PDF modification resulting from a finite emission size, we first expand the PDF for a fixed scintillation pattern to linear order in $\gamma_{s,i}$:

$$\begin{aligned} P(I; N, \gamma_s | \mathcal{G}) - P(I; N, \gamma_s=0 | G) \\ \approx [G_1 \gamma_{s,1} + G_2 \gamma_{s,2} - G(\gamma_{s,1} + \gamma_{s,2})] \frac{\partial P(I; N, \gamma_s=0 | G)}{\partial G}. \end{aligned} \quad (2.16)$$

Of course, the scintillation ensemble must now be included. Integrating each G_i with its respective weight e^{-G_i} gives

$$P(I; N, \gamma_s | G) - P(I; N, \gamma_s=0 | G) \approx 2\gamma_s (1 - G) \frac{\partial P(I; N, \gamma_s=0 | G)}{\partial G}. \quad (2.17)$$

Here, we have eliminated the degeneracy that appears at linear order between $\gamma_{s,1}$ and $\gamma_{s,2}$ by setting them both equal to a single characteristic size γ_s . If the effects of source emission size are substantial, then additional emission information, such as elongation or core/cone geometry, can be inferred from the higher order terms, although higher terms in the original gain expansion must also be retained. To facilitate a comparison with the decorrelation effects derived in §2.4.1, we integrate by parts after combining with the final scintillation weight:

$$\begin{aligned}
P(I; N, \gamma_s) - P(I; N, \gamma_s=0) & \quad (2.18) \\
& \approx -2\gamma_s \int_0^\infty dG G e^{-G} \frac{\partial^2 P(I; N, \gamma_s=0|G)}{\partial G^2}.
\end{aligned}$$

See Figure 2.3 for a comparison of these effects of emission size for various N .

The approximate form of Eq. 2.18 must be applied with some care; it fails in the limit $N \rightarrow \infty$, for example, because of the resulting divergent derivatives of the delta function that characterizes the measured intensity. However, the large- N limit is still easily accessible numerically by applying the full distribution of scintillation gain, as given by Eq. 30 in Gwinn et al. (1998). Substituting $\gamma_s = \gamma_{s,1} = \gamma_{s,2}$ in their expression and scaling to normalize the mean gives

$$P(\mathcal{G}) = \frac{1 + 2\gamma_s}{(1 - \gamma_s)^2} \left[e^{-(1+2\gamma_s)\mathcal{G}} - \left(\frac{\mathcal{G}}{\gamma_s} + (1 + \mathcal{G}) - 2\mathcal{G}\gamma_s \right) e^{-(2+\frac{1}{\gamma_s})\mathcal{G}} \right]. \quad (2.19)$$

When combined with the conditional PDF $P(I; N|\mathcal{G})$ (Eq. 2.2), this equation produces the scintillation averaged PDF of intensity. The disadvantage of this method is that the PDF must be calculated separately for every value of γ_s . Fits for emission size effects are then non-linear and computationally expensive, in contrast with the simple linear fit enabled by Eq. 2.18. Fortunately, the linear expansion of Eq. 2.18 is easily adequate for the full expected range of N , even exceeding 10^6 , if $\gamma_s \ll 1$. For $\gamma_s \gtrsim 0.1$, the linear approximation begins to differ substantially from the exact expression, but this region requires the appropriate quadratic term added to the original gain expansion as well.

Comparison of Eq. 2.18 with Eq. 2.11 shows that, at linear order and to the accuracy of the i.i.d. approximation for the pulse amplitudes, the effects of an extended emission region on the PDF of intensity are identical to the effects of temporal decorrelation, up to overall scale; this relationship is further analyzed in §2.4.3. Moreover, the modification arising from extended emission increases with the number of samples averaged, as was the case for temporal decorrelation (see Figure 2.3). These effects also depend on the gated signal-to-noise $S \equiv \langle A \rangle I_s / I_n$ of the observation; see Figure 2.4. Indeed, the dependence on S , when combined with the Poisson noise, determines the resolution limit of an observation. We derive this limit explicitly in §2.4.6.

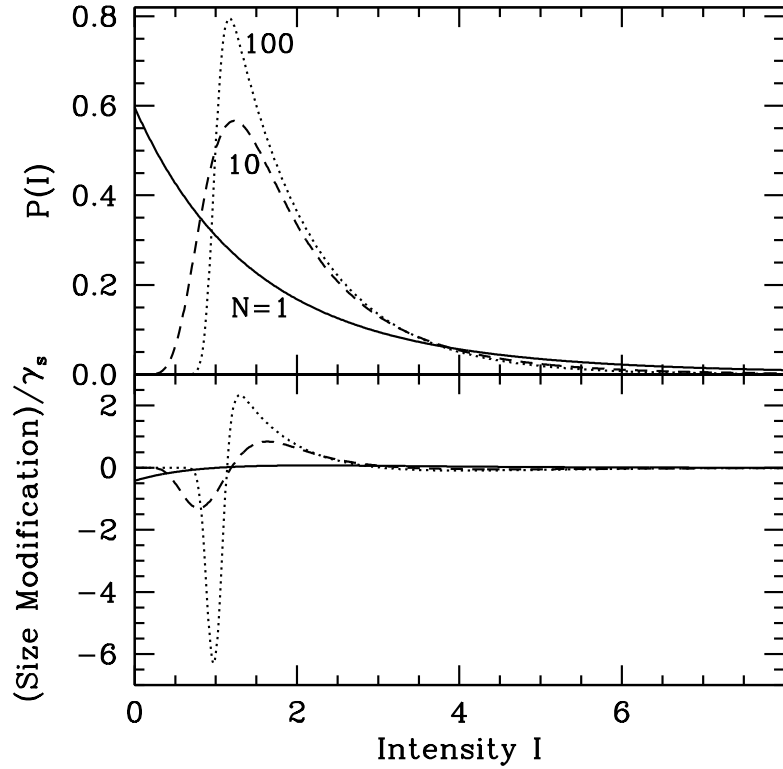


Figure 2.3: PDF of intensity and the corresponding modification expected for an extended emission region, for $N=1$, 10, and 100. The source and background intensities are unity, as are all pulse amplitudes A_j .

2.4.2.1 Effects of a Non-Static Emission Region

Our analysis is well-suited for long spectral accumulation times, over which the pulsed emission may be highly non-stationary, and the pulsar motion may be substantial. For instance, the emission might be bursty; the received radiation would then represent a superposition of spatially-offset emission sites. The inferred emission size, as quantified by γ_s , will then be a characteristic size for the emitting region over the corresponding retarded time. This characteristic size weights the spatial standard deviation by the integrated flux density at each location. Thus,

spatially-offset emitting regions contribute to the characteristic size, if they emit within the same accumulation time. In this sense, our estimate presents an upper limit on emission size, since the emitting region at a single instant may be small relative to the overall emission site. Furthermore, a small emitting region may undergo substantial displacement over the accumulation time, from lateral motion of the pulsar or rotation; both of these effects will present an upward bias of the size estimate. However, because of the weighting by flux density, weak extended emission may be overwhelmed by a strong pointlike component, yielding a nearly zero characteristic size. Any interpretation of a measured γ_s must address these competing factors.

2.4.3 Comparison of Emission Size and Temporal Decorrelation

As we have already observed, comparison of Eq. 2.11 with Eq. 2.18 demonstrates that the linear corrections to the intensity PDF for effects of finite emission size and temporal decorrelation are perturbations of identical shape, and differing weights, at least within the excellent i.i.d. approximation for the averaged intensities. The relative strength of these two perturbation weights is

$$\frac{\text{size}}{\text{decorrelation}} \approx 24 \frac{\Delta\tau_d^2}{N(N-1)} \gamma_s, \quad (2.20)$$

where we have substituted the square-law autocorrelation given in §2.4.1. Eq. 2.20 allows immediate assessment of the relative importance of effects. For example, if the source extends over 5% of the diffractive scale, then effects arising from the finite emission size will dominate those from decorrelation of the scintillation pattern as long as the averaging is over less than a quarter of the diffractive timescale.

2.4.4 Effects of Noise and Bias in Model Parameters

In practice, the estimates of parameters such as the source and background intensity are random variates, and are therefore subject to both noise and bias; we now derive the consequences of such errors. These effects, in contrast with effects in the previous sections, do not alter the theoretical PDF of intensity. However, they lead to similar changes in the model PDF, which mimic the effects of an extended emission region. They can thus lead to errors in the inferred parameters (γ_s and $\Delta\tau_d$) that are distinct from the fundamental limits posed by sampling.

We have seen that the PDF modifications that arise from both an extended emission region and decorrelation of the scintillation within the averaging time are naturally represented in terms of partial derivatives of $P(I; N|G)$ with respect to G , prior to integration with $P(G)$. To express all the results of this section in the same way, we again analyze departures using the i.i.d. approximation for

$P(I; N|G)$. We also give the expected bias to γ_s that arises from each type of parameter error.

2.4.4.1 Effects of Biased Background or Source Amplitude

Many effects can bias the estimates of the background or source amplitudes. For example, leaked pulse power from quadrature downconversion is frequency-reversed and can be dispersed into the off-pulse region (Demorest, 2007). Moreover, the analog-to-digital conversion of the signal requires quantization of the signal; this process introduces an offset of the background noise that varies with signal intensity (Jenet & Anderson, 1998; Gwinn, 2006).

A bias δI_n in the estimated background noise will result in a bias of the estimated pulse amplitudes $\delta A_j = -\delta I_n/I_s$, leading to a bias of the estimated mean intensity within a scintillation element $\delta(\bar{I} \equiv AI_sG + I_n) = (1 - G)\delta I_n$. To obtain the incurred PDF modification, we apply the i.i.d. approximation and use that $P(I; N|G)$ then only depends on the scale \bar{I} and the degree of averaging N . We first expand to leading order in $\delta\bar{I}$, then re-express the derivative using $AI_s\partial/\partial\bar{I} = \partial/\partial G$, and finally integrate G with its exponential weight to obtain

$$\begin{aligned}
 & P(I; N, \delta I_n=0) - P(I; N, \delta I_n) \\
 & \approx -\frac{\delta I_n}{AI_s} \int_0^\infty dG (1 - G) e^{-G} \frac{\partial P(I; N, \delta I_n=0|G)}{\partial G}.
 \end{aligned} \tag{2.21}$$

Comparison with Eq. 2.17 shows that this incurred modification is identical to a change in emission size $\gamma_s \rightarrow \gamma_s - \delta I_n / (2AI_s)$. A bias in pulse amplitudes is equivalent, with the substitution $\delta I_n = -I_s \delta A_j$. Thus, at leading order, emission size effects are indistinguishable from a biased estimate of the source or background intensities, regardless of averaging N . However, because the source emission size and the noise bias divided by signal-to-noise likely vary differently with pulse amplitude, segregating the pulses by strength provides a means to resolve this degeneracy.

2.4.4.2 Effects of Background or Source Parameter Noise

We similarly analyze the consequence of unbiased noise in the estimated source and background model parameters. This type of parameter error introduces spurious modulation in the corresponding model PDF, which must be compensated by artificial size effects. We therefore expect a positive bias on the inferred size.

Such parameter noise is frequently dominated by the source power estimate because of the limited sampling of the scintillation ensemble in each spectrum. This noise δA will be effectively independent of N , because we have assumed that the scintillation pattern remains approximately constant during the averaging, so each of the N consecutive pulses will be similarly biased. The mean intensity within each scintillation element is therefore biased: $\delta \bar{I} = (G - 1) I_s \delta A$. However, because this parameter noise is generally unbiased, the leading order correction

after an ensemble average is quadratic in $\delta\bar{I}$. Again translating to derivatives with respect to G and averaging over an ensemble of pulse amplitudes, we obtain

$$\begin{aligned}
 & P(I; N, \delta A=0) - P(I; N, \delta A) \\
 & \approx -\frac{1}{2} \left\langle \left(\frac{\delta A}{A} \right)^2 \right\rangle \int_0^\infty dG G^2 e^{-G} \frac{\partial^2 P(I; N, \delta A=0|G)}{\partial G^2}.
 \end{aligned} \tag{2.22}$$

This departure is similar to, though not strictly degenerate with, the effects of a finite emission size. This noise δA increases the inferred dimensionless emission size by $\gamma_s \rightarrow \gamma_s + \langle (\delta A/A)^2 \rangle / 4$. The normalized variance is given by the reciprocal of the number of averaged scintillation elements, $N_{\text{scint}} \sim B/\Delta\nu_d$, so γ_s experiences a positive bias $\sim 1/(4N_{\text{scint}})$.

The analogous emission size bias from noise in the estimated background intensity is $\sim 1/(4S^2 N_b)$, where S is the gated signal-to-noise, and N_b is the number of samples averaged to estimate the background intensity. Observe that parameter noise for the background intensity, unlike parameter noise arising from scintillation, is independent for each spectrum and can therefore be mitigated by averaging over series of pulses.

Similarly with effects of bias in the model parameters, the near-degeneracy with effects of finite emission size is broken by comparing multiple analyses. For example, varying the bandwidth used to estimate the model parameters changes

their noise; the evolution of measured residual structure with analyzed bandwidth thus precisely quantifies the influence of parameter noise.

2.4.5 Effects of Instrumental Distortion

Many instrumental distortions depend on the signal amplitude; they can therefore be modeled by imposing appropriate distortions on the distribution of scintillation gain $P(G)$. The influence on the PDF can be modeled by combining the modified $P(G)$ with the conditional distributions $P(I; N|G)$ derived above. Alternatively, the modulation index m (Eq. 2.15) provides a simple measure to quantify changes in $P(G)$; we therefore use m to characterize effects in this section.

Instrumental distortions can arise, for example, from saturation of the observing system. Because strong pulsars can be highly variable and dominate backgrounds when they are on, optimal quantization levels are often difficult to determine, and even systems with many bits may saturate. A simplified model of saturation imposes a voltage cutoff on the observed scalar electric field in the time-domain:

$$\hat{x}_i = \begin{cases} x_i & \text{if } |x_i| < \sigma_{\max}, \\ \sigma_{\max}\text{sign}(x_i) & \text{else.} \end{cases} \quad (2.23)$$

The effect of this cutoff is two-fold: power from the strongest samples is spread across all channels in the spectral domain, and the observed signal intensity is

underestimated. At leading order, the second effect predominates, so that the estimated off-pulse noise overestimates the effective on-pulse noise. In terms of the discussion in §2.4.4.1, saturation leads to a bias $\delta I_n < 0$ and thus, an inferred emission size that is upward biased.

Likewise, if the pulse is heavily dispersed, then the saturation predominantly affects samples with the highest scintillation gain G . As a simplified model of this effect, we replace the distribution of scintillation gain $P(G) = e^{-G}$ by a truncated version: $\hat{P}(G) \equiv e^G \theta(G_{\max} - G) + e^{-G_{\max}} \delta(G - G_{\max})$, where $\theta(x)$ is the Heaviside step function. The corresponding modulation index is

$$\hat{m}^2 = \frac{\langle G^2 \rangle_{\hat{P}}}{\langle G \rangle_{\hat{P}}^2} - 1 = \frac{\sinh(G_{\max}) - G_{\max}}{\cosh(G_{\max}) - 1} \leq 1. \quad (2.24)$$

Comparison with Eq. 2.15 shows that even a relatively large cutoff $G_{\max} = 5$ gives suppression equivalent to modest emission size effects, $\gamma_s \approx 0.014$. Furthermore, the exponential character of the incurred suppression leads to an extremely rapid onset of saturation artifacts once the largest intensities clear the threshold for saturation; the effects on the strongest pulses may therefore be quite pronounced relative to those on the weaker pulses.

2.4.6 Expected Resolving Power

Poisson noise presents a fundamental limit on the resolving power afforded by scintillation, as a fraction of the magnified diffractive scale. This limit depends on

both the gated signal-to-noise ratio $S \equiv \langle A \rangle I_s/I_n$ and the observational parameters B and T_{obs} . Figure 2.4 illustrates the variation of PDF modification with S , for $N = 1$. The modification from extended emission size is maximal at zero intensity, with fractional strength

$$\begin{aligned} & \left| \frac{P(I=0; N=1, \gamma_s) - P(I=0; N=1, \gamma_s=0)}{P(I=0; N=1, \gamma_s=0)} \right| & (2.25) \\ & = -2\gamma_s \left[2 + \frac{1}{S} + (1+S) \frac{e^{-1/S}}{\text{Ei}(-1/S)} \right], \end{aligned}$$

where $\text{Ei}(x)$ is the imaginary error function. Equating Eq. 2.25 with the level of Poisson noise η in the observed PDF then provides an excellent assessment of resolving power.

We apply an approximation for Eq. 2.25 to obtain the following estimate for the achievable resolution, $\sqrt{\gamma_{s,\text{min}}}$, in units of the magnified diffractive scale:

$$\sqrt{\gamma_{s,\text{min}}} \approx \sqrt{\frac{\eta}{S}} \exp [0.2 + 0.09 (\ln S)^2 + 0.005 (\ln S)^3]. \quad (2.26)$$

This approximation is good to within 10% for $10^{-3} < S < 2$. Simulations indicate that substituting $\eta \equiv \frac{1.3}{\sqrt{N_{\text{tot}}}}$ effectively estimates the standard errors from the full distribution fits, where N_{tot} is the total number of sampled points used to estimate the PDF of intensity.

We now apply this result to estimate the resolving power for typical observational parameters. A (1 hour) \times (4 MHz) observation of a pulsar with 5% duty

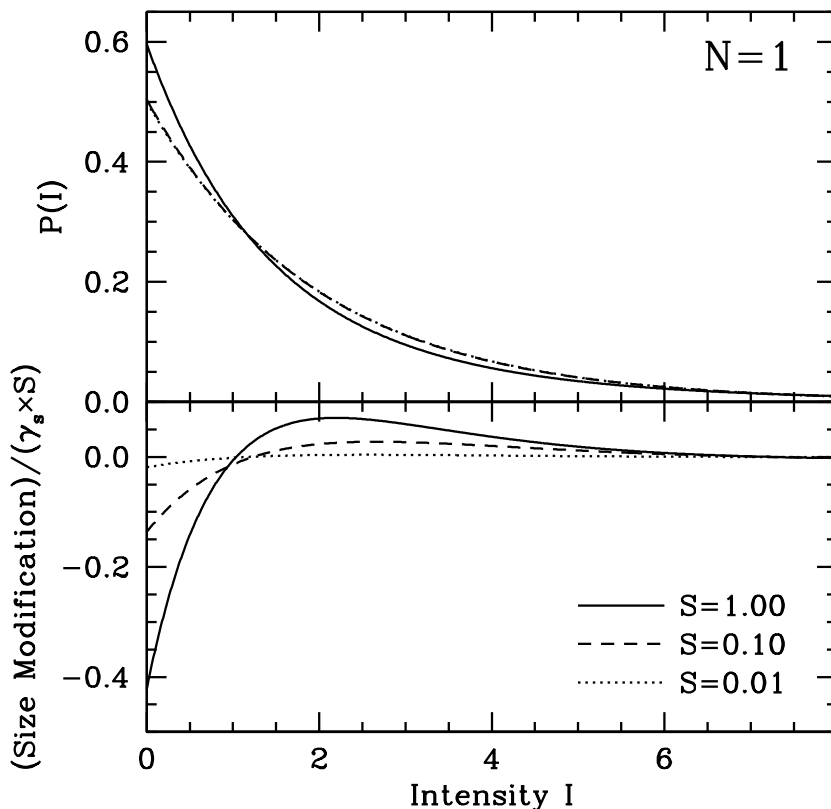


Figure 2.4: Intensity PDF and the corresponding modification for emission size effects, for $N=1$ and varying gated signal-to-noise (S). In each case, $\langle A \rangle I_s + I_n = 2.0$. Observe that the plotted modification is scaled by both the dimensionless size parameter (γ_s) and S .

cycle gives $\sim 10^9$ on-pulse samples of the flux density. A gated SNR $S = 1$ then gives a 3σ detection limit of about 1% of the magnified diffractive scale, $S = 0.1$ gives about 10% of the magnified diffractive scale, and $S = 0.01$ gives about 50% of the magnified diffractive scale. Since the detection limit is much more sensitive to S than to the number of sampled points, an analysis of a subset of strong pulses may provide optimal resolution.

2.5 Moments of the Distributions: The Modulation Index and Self-Noise

Moments of the intensity distribution provide simple diagnostics for scattering and source inference. Frequently, moments provide optimal estimators of distribution parameters and are therefore both powerful and elegant tools for characterizing distributions. However, a blind calculation of moments may be blind to effects of RFI, artifacts of finite scintillation averages, or deficiencies of models, whereas a comparison with the full distribution functions might identify such effects.

We focus on two applications of moments of the distribution: the intensity modulation index and a practical technique for estimating self-noise. For the modulation index, we include all sources of noise, as well as evolution of the scintillation pattern and spatially-extended source emission. For the self-noise estimator, we constrain amplitude variations of the pulsar and assume that there is no decorrelation of the scintillation pattern within the averaging time ($N \ll \Delta\tau_d$); we then assess departures from these assumptions qualitatively.

2.5.1 The Modulation Index

In §2.4.2, we demonstrated that the size of the emission region affects the modulation index m . However, self-noise, temporal decorrelation, and background noise also affect the modulation index. These effects are readily evaluated, either by

analysis of the random variables that make up each sample of intensity (Eq. 2.1), or by appropriate derivatives of the corresponding characteristic function.

Here, we analyze only the case for which the pulse amplitudes are i.i.d.: $\langle A_i A_j \rangle = \langle A \rangle^2 + \delta_{ij} \langle \delta A^2 \rangle$. This condition is different than the assumptions for the i.i.d. approximation derived above, which assumes the stronger condition that the spectral statistics are i.i.d.. Although many pulsars appear to have i.i.d. pulse amplitudes, others display striking departures. For example, phenomena such as nulling and mode-changing break statistical isotropy, and the brightest pulses from the Vela pulsar tend to occur in groups (Palfreyman et al., 2011).

To explicitly account for the temporal decorrelation of the scintillation pattern, we again assign the autocorrelation appropriate for square-law scattering, quantified by the decorrelation timescale (in pulse periods) $\Delta\tau_d$. We incorporate effects of an extended emission region in terms of the dimensionless size parameter γ_s , defined by Eq. 2.14, with the assumption that $\gamma_s \ll 1$. Modification of the scattering assumptions will introduce minor scaling alterations for these contributions.

To leading order in the effects of emission size and temporal decorrelation, the modulation index is then given by

$$\begin{aligned}
m^2 &\equiv \frac{\langle (I - I_n)^2 \rangle}{\langle I - I_n \rangle^2} - 1 & (2.27) \\
&\approx 1 - \underbrace{4\gamma_s \left(1 + \frac{1}{N}\right)}_{\text{Emission Size}} + \underbrace{\frac{2}{N}}_{\text{Self-Noise}} + \underbrace{\frac{1}{NS} \left(2 + \frac{1}{S}\right)}_{\text{Signal-to-Noise}} \\
&\quad + \underbrace{4(1 - 2\gamma_s) \frac{\langle \delta A^2 \rangle}{N \langle A \rangle^2}}_{\text{Intrinsic Variability}} - \underbrace{(1 - 4\gamma_s) \frac{N^2 - 1}{6\Delta\tau_d^2}}_{\text{Decorrelation}}.
\end{aligned}$$

Here, we have grouped the contributions to the modulation index, to explicitly illustrate the relative influence of the various effects. We also have used $\gamma_{s,1} = \gamma_{s,2} \equiv \gamma_s$ because of the degeneracy at linear order. We see that the relative contributions of an extended emission region and decorrelation of the scintillation pattern give the previously derived relationship between their respective PDF modifications (Eq. 2.4.3).

The modulation index corresponds to the zero time and frequency lags in the autocorrelation function of intensity; analysis of non-zero lags eliminates many of the terms in Eq. 2.27. For example, non-zero spectral lags eliminate the ‘‘Signal-to-Noise’’ contribution and mitigate the ‘‘Self-Noise’’ contribution (although intrinsic modulation induces correlations in the spectral self-noise that preserve the contribution). Non-zero temporal lags fully eliminate all terms other than ‘‘Emission Size’’ and ‘‘Decorrelation,’’ which is enhanced.

2.5.2 An Estimate of Self-Noise

The self-noise of a signal is a useful diagnostic, which can be used to identify intrinsic variability on timescales shorter than the spectral accumulation time. Intrinsic modulation induces correlations among frequencies, without modifying the mean spectrum (Gwinn & Johnson, 2011). If spectra are formed according to the criteria in §2.2.3, then the power in each spectral channel is an exponential random variable. Because such variables are completely characterized by their mean, the single-channel statistics are therefore immune to intrinsic modulation. However, the intrinsic modulation does introduce correlations in the noise of nearby channels. We now derive the expected self-noise in the spectral domain, thereby enabling detection of such correlations.

One method for estimating self-noise is to compare pairs of nearby samples that are assumed to be within the same scintillation element. We will assume that the pair consists of samples with uncorrelated self-noise (e.g. pairs from different pulses, or from the same pulse with negligible intrinsic modulation). Because self-noise is heteroscedastic (see §2.3.2.3), we calculate the noise $\delta I^2 \equiv (I_1 - I_2)^2/2$ in pairs of samples $\{I_1, I_2\}$ as a function of their mean $I = (I_1 + I_2)/2$; we denote the resulting noise estimate $\delta I^2(I)$. The ensemble average is given by

$$\delta I^2(I) = \frac{\int_0^{2I} 2(I - I')^2 P(I', 2I - I'; N) dI'}{\int_0^{2I} P(I', 2I - I'; N) dI'}, \quad (2.28)$$

where $P(I_1, I_2; N)$ represents the probability of sampling the pair $\{I_1, I_2\}$, including an ensemble average over scintillation. Because we assume that the samples are independent but are drawn from the same scintillation element, $P(I_1, I_2; N) = \int_0^\infty dG P(I_1; N|G)P(I_2; N|G)$.

As usual, we apply the i.i.d. approximation. Although the scintillation integral cannot be evaluated in closed form, Eq. 2.32 readily yields the identity

$$\begin{aligned} \int_0^{2I} 2(I - I')^2 P(I', 2I - I'; N) dI' & \quad (2.29) \\ & = \frac{I^2}{N + \frac{1}{2}} \int_0^{2I} P(I', 2I - I'; N) dI'. \end{aligned}$$

This relationship immediately unveils the simple relationship between the estimated mean signal and noise:

$$\delta I^2(I) = \frac{I^2}{N + \frac{1}{2}}. \quad (2.30)$$

In fact, because the identity given by Eq. 2.29 holds regardless of the integration over G , this property of the estimated self-noise is independent of the degree of sampling and the properties of scintillation. We see that this method for estimating the self-noise gives the same form as the exact expression (see §2.3.2.3), except that $N \rightarrow N + 1/2$.

If the averaged intensities are from different pulses, then pulse-to-pulse variations contribute additional noise. If the averaged intensities are from the same

pulses, then intrinsic variations on timescales shorter than t_{acc} induce correlations in self-noise, and thereby decrease the measured noise; if $N > 1$ then pulse-to-pulse variations within the averaging will increase the noise. Each of these effects can be estimated by applying the appropriate substitution $N \rightarrow N_{\text{eff}}$. Similar tests were applied by Gwinn et al. (2011) to infer short-timescale variability ($< 300\mu\text{s}$) of PSR B0834+06.

2.6 Summary

We have presented observable quantities that describe the flux density of a source exhibiting strong diffractive scintillation. These observables include both distribution functions and bulk indicators, such as the modulation index and estimates of self-noise. Our results encompass a broad range of physical and instrumental effects, such as non-stationary background noise, arbitrary temporal averaging, pulse-to-pulse variability, decorrelation of the scintillation pattern within the averaging, and the possibility of spatially-extended source emission, making them well-suited for direct comparison with observations. The primary benefits of such comparisons include the following:

- We can completely decouple effects arising from decorrelation of the scintillation pattern from those of extended emission size by analyzing Nyquist-limited data without averaging.

- Our results enable estimation of the emission region sizes of individual pulses and of arbitrary subclasses of pulses.
- For point-source emission, our statistical description does not require specification of either the nature or geometry of the scattering material. Residuals relative to the point-source model of §2.3 therefore provide robust indicators of either intrinsic emission effects (e.g. finite size of the emission region), extrinsic effects (e.g. evolution of the scintillation pattern), or instrumental limitations (e.g. finite observing bandwidth). These competing effects can be distinguished by varying the degree of averaging, the analyzed bandwidth or the chosen subset of pulses.
- Our technique does not appeal to extraordinary scattering geometry (such as is inferred for parabolic arcs) or extreme scattering events to infer the size of the emission region. Furthermore, our analysis is effective on short observations ($\lesssim 1$ hour) and is easily reproducible. The achievable resolution limits (see §2.4.6) can be a small fraction of the magnified diffractive scale.

In particular, our results are ideal for describing the statistics of low-frequency observations of scintillating pulsars. In such cases, the scintillation bandwidth can be narrow relative to the observing bandwidth, allowing an estimate of the scintillation-averaged source intensity for each pulse. The tight coupling of scintillation and source variations is then described by our models, which fully in-

corporate the intrinsic source amplitudes and the background noise estimates via on-pulse and off-pulse averages.

As we will discuss in Chapter 4, we found excellent agreement between these theoretical expectations and observations of the Vela pulsar at 800 MHz. We thereby achieved a spatial resolution of $\sim 1\%$ of the magnified diffractive scale – about 4 km at the pulsar. Application to other pulsars will enrich the empirical description of pulsar radio emission regions, potentially including variation among individual pulses and pulse subclasses.

2.7 Appendix: Mathematical Results

2.7.1 Average of Exponential Random Variables with Different Scales

Consider an exponential random variable I : $P(I; \bar{I}) = \bar{I}^{-1} e^{-I/\bar{I}}$ for $I > 0$, where $\bar{I} \equiv \langle I \rangle$. The corresponding characteristic function is $\varphi(k) = (1 - i\bar{I}k)^{-1}$. The distribution $P(I; \{\bar{I}_j\})$ of the average of N such variables from independent distributions with different scales $\{\bar{I}_j\}$ is then easily derived by inverting the partial fraction decomposition of the product of characteristic functions:

$$P(I; \{\bar{I}_j\}) = N \sum_{j=1}^N \left(\frac{\bar{I}_j^{N-2}}{\prod_{\substack{\ell=1 \\ \ell \neq j}}^N (\bar{I}_j - \bar{I}_\ell)} \right) e^{-NI/\bar{I}_j}, \quad I > 0. \quad (2.31)$$

In other words, the distribution of the average of exponential random variables is a weighted sum of the marginal distributions. This sum is the hypoexponential (or generalized Erlang) distribution.

The representation of Eq. 2.31 is singular if any of the scales are equal. In particular, if the random variables are i.i.d., each with scale \bar{I} , then their average is drawn from an Erlang distribution, which is simply a gamma distribution with integer shape parameter:

$$P(I; \bar{I}, N) = \frac{N^N}{(N-1)!} \frac{I^{N-1}}{\bar{I}^N} e^{-\frac{NI}{\bar{I}}}, \quad I > 0. \quad (2.32)$$

Goodman (1985) discusses both these distributions in the similar context of polarized thermal light.

2.7.2 Distribution of Correlated Exponential Random Variables

We now approximate the distribution of N correlated exponential random variables $\{I_i\}$. The exact distribution follows by first constructing a complex multivariate normal distribution with the desired covariance matrix; the exponential random variables are the squared norms of each circular complex Gaussian random variable. We restrict ourselves to the case in which each random variable has unit mean. The characteristic function of $P(\{I_i\})$ can then be written (Mallik,

2003)

$$\varphi(\{k_i\}; \boldsymbol{\Sigma}) = \frac{1}{\det[\mathbf{I} - i \text{diag}\{k_i\} \boldsymbol{\Sigma}]}. \quad (2.33)$$

Here, $[\boldsymbol{\Sigma}]_{ij} = \sqrt{\langle I_i I_j \rangle - 1} \equiv \sqrt{\Gamma_{ij}}$.

We now expand in $\boldsymbol{\epsilon} \equiv \mathbf{J} - \boldsymbol{\Sigma}$, where \mathbf{J} is the $N \times N$ unit matrix: $[\mathbf{J}]_{ij} = 1 \forall i, j$. Since $[\boldsymbol{\epsilon}]_{ij} \approx (1 - \Gamma_{ij})/2$, we can approximate the characteristic function to leading order as

$$\varphi(\{k_i\}; \boldsymbol{\Sigma}) = \frac{1}{1 - i \sum_{j=1}^N k_j} + \frac{\sum_{i < j} k_i k_j (1 - \Gamma_{ij})}{\left(1 - i \sum_{j=1}^N k_j\right)^2} + \mathcal{O}([1 - \Gamma_{ij}]^2). \quad (2.34)$$

The inverse Fourier transform of $\varphi(\{k_i\}; \boldsymbol{\Sigma})$ then gives our approximation to $P(\{I_i\})$. Although this inverse can be written in terms of delta functions and derivatives, the most natural form expresses the action as a weight function:

$$\begin{aligned} & \int d^N I_i f(\{I_i\}) P(\{I_i\}) \\ &= \int_0^\infty dI \left[f(\{I\}) e^{-I} - \sum_{i < j} (1 - \Gamma_{ij}) I e^{-I} \frac{\partial^2 f}{\partial I_i \partial I_j} \Big|_I + \mathcal{O}([1 - \Gamma_{ij}]^2) \right]. \end{aligned} \quad (2.35)$$

Here $f(\{I\})$ denotes $f(\{I_i = I \forall i\})$.

2.7.2.1 Example: Bivariate PDF of Correlated Exponential Random Variables

The joint distribution of a pair of correlated exponential random variables is particularly simple. In this case, the characteristic function (2.33) is easily inverted:

$$P(I_1, I_2; \Gamma) = \frac{1}{1 - \Gamma} I_0 \left(\frac{2\sqrt{\Gamma}}{(1 - \Gamma)} \sqrt{I_1 I_2} \right) \exp \left[-\frac{1}{(1 - \Gamma)} (I_1 + I_2) \right], \quad I_1, I_2 > 0. \quad (2.36)$$

Here, $\Gamma = \langle I_1 I_2 \rangle - 1$, and $I_0(x)$ is the modified Bessel function. Using Eq. 2.35, we can approximate Eq. 2.36 as

$$P(I_1, I_2; \Gamma) = e^{-\hat{I}} \left\{ \delta(\Delta I) + (1 - \Gamma) \left[\frac{2 - \hat{I}}{4} \delta(\Delta I) + \hat{I} \delta''(\Delta I) \right] + \mathcal{O}[(1 - \Gamma)^2] \right\}, \quad \hat{I} > 0, \quad (2.37)$$

where $\hat{I} \equiv (I_1 + I_2)/2$ and $\Delta I \equiv I_1 - I_2$.

2.7.2.2 Convolution of Correlated Exponential Random Variables

The gamma distribution is an excellent approximation for the sum of independent exponential random variables that are not necessarily isotropic (see §2.3.2) and can also be used to approximate the convolution of correlated exponential random variables. This approximation is most effective for correlations that are particularly strong or weak. For example, consider the average of two exponential

random variables, each with unit mean, and with covariance $\langle I_1 I_2 \rangle = 1 + \Gamma$. The gamma distribution that matches the mean and variance of the exact average has a corresponding effective number of degrees of freedom $N_{\text{eff}} = 2/(1 + \Gamma)$. These distributions agree exactly for the limits $\Gamma \rightarrow 0, 1$, but suffer sizeable discrepancies for intermediate correlations. For example, the third central moment of the average of two correlated exponential random variables is $(1 + 3\Gamma)/2$ but is $2/N_{\text{eff}}^2 = (1 + \Gamma)^2/2$ for the corresponding gamma distribution – a difference of $\sim 10\%$ for intermediate correlation.

More generally, for N averaged exponential random variables with correlation matrix Γ_{ij} , as defined above, and unit mean, the appropriate number of degrees of freedom based on variance matching is $N_{\text{eff}} = N \left(1 + 2N^{-1} \sum_{i < j} \Gamma_{ij}\right)^{-1}$. Even in the case of large N , the disparity in skewness between the exact average and the appropriate gamma distribution remains. For instance, if $\Gamma_{ij} \equiv \Gamma$ for $i \neq j$ then,

$$\mu_3 = \begin{cases} 2\Gamma^{3/2} + \frac{6\Gamma}{N} (1 - \sqrt{\Gamma}) + \frac{2}{N^2} (1 - 3\Gamma + 2\Gamma^{3/2}) & \text{Exact Average,} \\ 2\Gamma^2 + \frac{4\Gamma}{N} (1 - \Gamma) + \frac{2}{N^2} (1 - \Gamma)^2 & N_{\text{eff}} = \frac{N}{1 + (N-1)\Gamma}, \end{cases} \quad (2.38)$$

where μ_3 denotes the third central moment. Again, we see that these expressions agree for $\Gamma \rightarrow 0, 1$ as expected, but differ substantially for intermediate correlation, even as $N \rightarrow \infty$.

Chapter 3

Interferometric Visibility of a Scintillating Source: Statistics at the Nyquist Limit

We now extend the ideas and treatment of Chapter 2 to interferometric visibility.¹ While interferometry poses a natural extension, practical considerations again motivate this work. In particular, the advent of space-VLBI with RadioAstron has increased accessible baselines by an order of magnitude, up to the distance of the moon (Kardashev et al., 2013). However, such long baselines require exceptional delicacy, especially to decouple the variability of scintillation from that of the source.

As in Chapter 2, we will account for arbitrary temporal averaging, intrinsic variability within the averaging time, and the possibility of spatially-extended source emission. We will demonstrate that the interplay between scintillation and self-noise induces several remarkable features, such as a broad “skirt” in the visibility distribution. Preliminary results with RadioAstron suggest that

¹This chapter is adapted from Johnson & Gwinn (2013).

these techniques can effectively identify extremely weak correlation signatures on extremely long baselines, perhaps sufficient to identify refractive substructure in the scattering disk (see Chapter 5).

3.1 Introduction

Radio astronomy is now exploring two limiting regimes. First, with the construction of ever-larger collecting areas, noise intrinsic to the source (i.e. *self-noise*) can be a major, or even dominant, component of the noise budget. Second, observing systems at decimeter wavelengths can now record baseband data over wide bandwidths and with sufficient bit-rates to effectively capture the full information content of the signal (up to the fundamental limit described by the Nyquist sampling theorem). These advances motivate mathematical descriptions of the new regimes and the development of novel techniques that optimally utilize the signal information.

These considerations prompted a previous work (Johnson & Gwinn, 2012; hereafter JG12), in which we derived the probability density function (PDF) of flux density, sampled at the Nyquist rate, for a scintillating source. We accounted for background noise,² arbitrary temporal averaging, the possibility of decorrelation of the scintillation pattern within the averaging time, and spatially-extended source emission. We also outlined tests to identify self-noise, as well as a mechanism to

²By *background noise*, we mean the sum of all noise other than that of the source (e.g., receiver, spillover, atmosphere, and background sky noise).

detect rapid intrinsic variability of a signal. We then demonstrated the success of this description on 800 MHz observations of the Vela pulsar and, thereby, obtained a spatial resolution of approximately 4 km at the pulsar (Johnson et al., 2012).

We now extend these mathematical results and techniques to interferometric visibility, which preserves much of the statistical framework. This extension involves a pair of stations, which observe independent background noise but correlated scattering kernels and identical source noise. However, these mild modifications lead to substantial changes in the analytical results for the distribution functions. Furthermore, the interferometric visibility is complex, and thus is characterized by a two-dimensional PDF, whereas the flux density is a positive real number. We frequently utilize projections as a natural mechanism for exploring the transition between these domains. We also offer several other close analogs with common metrics for flux-density, and we provide tools to quantify the complex noise in sampled visibilities.

Pulsars are some of the richest targets for interferometry, and we have tailored our treatment to account for their extraordinary variability. In particular, we emphasize results for single-pulse studies with Nyquist-limited resolution. We then connect to traditional limits through asymptotic forms of our results, as the averaging is increased and self-noise becomes negligible. However, our principal goal is to facilitate precision tests using interferometric observations, particularly of pul-

sars, that can robustly distinguish between intrinsic and extrinsic characteristics and can sensitively probe delicate modifications of either.

3.1.1 Assumptions and Strategy for Comparison with Observations

Our scope is deliberately broad, intended to encompass the majority of pulsar observations at meter and decimeter wavelengths. However, to assess the suitability for comparison with any particular observation, we now outline the assumptions underlying our results. Our *physical* requirements are that

- The source emits amplitude-modulated noise (Rickett, 1975).
- The scattering is strong. That is, the diffractive scale $r_d = \lambda/\theta$ is much smaller than the Fresnel scale $r_F = \sqrt{\lambda D}$, where λ is the observing wavelength, θ is the angular size of the scattering disk, and D is the characteristic distance to the scattering material (Cohen & Cronyn, 1974).

The first assumption is quite robust for most, if not all, astrophysical sources, simply because the superposition of many independent radiators will produce a signal of this form. Also, the majority of meter and decimeter pulsar observations fall easily within the regime of strong scattering: $r_d/r_F \ll 1$.

On the other hand, the *instrumental* assumptions that we require are that

- The data explore a large representation of the full ensemble of diffractive scintillation: $(B/\Delta\nu_d)\times(t_{\text{obs}}/\Delta t_d) \gg 1$, where $\{B, t_{\text{obs}}\}$ are the total observational bandwidth and duration, and $\{\Delta\nu_d, \Delta t_d\}$ are the characteristic bandwidth and timescale of the scintillation pattern. If $B/\Delta\nu_d \gg 1$, then intrinsic single-pulse amplitudes may be estimated, allowing a comparison between the data and our models that requires no fitted parameters.
- The data are coherently dedispersed, baseband shifted, and “fringed” with an appropriate phase model.
- The time to form each spectrum, or the *accumulation time* t_{acc} , is much longer than the pulse-broadening timescale t_0 but much shorter than the characteristic scintillation timescale Δt_d .

The last assumption is perhaps the only one that is atypical of modern observations and processing. However, it ensures that the spectra reflect the convolution action of the scattering on the intrinsic pulsar signal with a stochastic “propagation kernel” (Hankins, 1971; Williamson, 1972; Gwinn & Johnson, 2011). For pulsars, a particularly elegant limiting case is the formation of spectra that include *all* the pulsed power. This convolution leads to extremely general results; we do not assume thin-screen scattering or a particular spectrum for the density inhomogeneities of the interstellar medium (ISM), for example.

Our work also addresses the physical possibility of an extended emission region and the instrumental possibility of averaging (or integration) of the calcu-

lated visibilities. For the former, we assume that the source is a small fraction of the magnified diffractive scale (see §3.3); for the latter, we assume that the averaging is of N independent cross-spectra (say, from different pulses), over a timescale much shorter than Δt_d (i.e. the “snapshot image” of Narayan & Goodman (1989)). While frequency averaging is analogous, it inherits additional information from non-stationary signals and requires the specification of individual pulse profiles, whereas a description of temporal averaging requires only the phase-averaged source intensity for each pulse (see Chapter 2 for details). Hereafter, we exclusively use N to denote this degree of temporal averaging.

3.1.2 Relation to Previous Work

For non-scintillating sources, the statistics of interferometric visibility are well-known; see Moran (1976) or Thompson et al. (2001). In particular, the self-noise has been carefully characterized. For example, Kulkarni (1989) analyzed the noise in synthesis imaging for sources of arbitrary strength, while Anantharamaiah et al. (1989) studied the noise, with an emphasis on extremely bright sources.

Scintillation complicates the statistics, and even the noise-free (i.e. infinite-averaging) case warrants careful attention. Narayan & Goodman (1989) and Goodman & Narayan (1989) analyzed this limit via both numerical and analytical techniques, with an emphasis on moments of the distribution of visibility. Also, Gwinn (2001) calculated the full PDF of interferometric visibility for a scin-

tillating source in this limit and accounted for the effects of an extended emission region.

Gwinn et al. (2012a) and Gwinn et al. (2012b) then incorporated the contribution of both self-noise and background noise for modest averaging ($N \gtrsim 20$) by applying the central limit theorem to the averaged visibilities. The present work extends these ideas by adopting a different strategy, following the techniques of Chapter §2. Namely, we establish the statistics for individual spectral samples and then determine the effects of averaging by a convolution of independently drawn samples. This method permits the treatment of data with arbitrary averaging, N , including no averaging (i.e. $N = 1$), and requires no assumptions about the nature of the intrinsic variability or of the scattering material.

To put our results in the context of these earlier efforts, we also present asymptotic forms of our equations for strong signals and high degrees of averaging. However, our principal goal is to facilitate direct comparisons with observations.

3.1.3 Outline of Chapter

In §3.2, we focus on visibility statistics for a scintillating point source. We account for temporal averaging, but assume that the scintillation pattern is fixed within each average. Under these constraints, we first outline the essential statistical framework for the visibility statistics (§3.2.1) and calculate moments and noise of the visibility statistics within a fixed scintillation element (§3.2.2). We then

outline approximation schemes for the PDF of visibility during a fixed scintillation element (§3.2.3) and demonstrate how to calculate the PDF of visibility after including the scintillation ensemble (§3.2.4). We give examples of the visibility statistics in limiting regimes (§3.2.5) and demonstrate that the combination of self-noise and scintillation introduces a “skirt” in the visibility PDF that dominates its asymptotic form, regardless of the source strength or the baseline (§3.2.6). We also provide a prescription for estimating the self-noise (§3.2.7).

Next, in §3.3, we quantify the influence of a spatially-extended emission region on this PDF and discuss the potential of interferometry to resolve the size and anisotropy of such emission. We demonstrate that the effect of a small emission region depends only on two parameters, regardless of the scattering geometry; however, the translation to a dimensionful size at the source depends on the scattering geometry. We also derive a simplified version of the PDF of visibility for the special case of a zero-baseline interferometer.

Finally, in §3.4, we summarize our results and outline some observational prospects.

3.2 PDF of Visibility

We now derive the expected PDF of interferometric visibility arising from a scintillating point source. We allow arbitrary temporal averaging, in sets of N independent cross-spectra, but assume that the scintillation pattern is fixed during

each average. All of our results apply to scalar electric fields (i.e. a single linear or circular polarization) that conform to the assumptions described in §3.1.1.

Our notation follows Chapter 2. Namely, z_x denotes a circular complex Gaussian random variable with unit variance, indexed by x ; G_x denotes an exponential random variable with unit scale. We use $P()$ to generically denote a PDF with respect to the given variables and parameters, and we present PDFs $P(w)$ of complex quantities w with respect to the metric $d\text{Re}[w]d\text{Im}[w]$. Occasionally, we employ the shorthand $w_r \equiv \text{Re}(w)$, $w_i \equiv \text{Im}(w)$.

Furthermore, to help visualize the visibility PDF, we rely on projections. These projections are most enlightening along the real axis $V_r \equiv \text{Re}(V)$, where they emphasize the relative effects of differing baselines. We favor the following two projections:

$$\begin{aligned}
 P(V_r; N) &\equiv \int dV_i P(V; N), \\
 Q(V_r; N) &\equiv \int dV_i V_i^2 P(V; N).
 \end{aligned}
 \tag{3.1}$$

The first projection identifies the concentration of density toward greater real part, which reflects the average visibility; the second (weighted) projection quantifies the imaginary spread of density, which reflects the influence of scintillation and the noise from both the background and the source.

3.2.1 Field Statistics

In §2.3.1, we derived the electric-field statistics for a scintillating point source. These statistics depend on the amplitude-modulated noise of the source, the strong scattering of the ISM, and the receiver noise. We now review the basic ingredients of this description and establish the necessary notation.

For the electric field, the amplitude-modulated noise takes the form $\sqrt{A_j I_s} f_i \epsilon_i$. Here, A_j is a dimensionless amplitude factor, indexed by pulse, that accounts for pulse-to-pulse variations, I_s is a constant characteristic scale of source intensity, f_i is a power-preserving envelope, and ϵ_i is white Gaussian noise of unit variance. Thus, the pulse profile is simply $|f_i|^2$, the gated signal has mean amplitude $A_j I_s$, and ϵ_i accounts for the noiselike nature of the emission. Note that this treatment accommodates arbitrary variability of the pulsar, such as the possibility of correlated pulse-to-pulse variations, log-normal amplitude statistics, or nanosecond-scale bursts (Rickett et al., 1975; Cairns et al., 2001; Kramer et al., 2002).

During a fixed scintillation element, the scattering acts to convolve this intrinsic emission with a stochastic propagation kernel: $g_i \eta_i$. In the strong-scattering limit, the form of this kernel is similar to the emission of the pulsar. Namely, a power-preserving envelope g_i modulates Gaussian noise η_i . This envelope is more commonly described by its squared norm: the pulse-broadening function $|g_i|^2$.

Finally, an observer samples the propagated signal in the presence of white background noise: $\sqrt{I_n}\beta_i$. Here, I_n is a constant, characteristic scale of the background noise, and β_i is white Gaussian noise of unit variance. If the background noise changes significantly with time, then a changing scale may be added, analogous to A_j .

The observed scalar electric-field time series x_i and its Fourier-conjugate spectrum \tilde{x}_i are thus given by

$$\begin{aligned} x_i &= \sqrt{A_j I_s} [(f\epsilon) * (g\eta)]_i + \sqrt{I_n}\beta_i \\ \Rightarrow \tilde{x}_i &= \sqrt{A_j I_s} (\tilde{f} * \tilde{\epsilon})_i (\tilde{g} * \tilde{\eta})_i + \sqrt{I_n}\tilde{\beta}_i, \end{aligned} \quad (3.2)$$

where a tilde denotes a Fourier conjugate variable.

Because $\tilde{\epsilon}_i$, $\tilde{\eta}_i$, and $\tilde{\beta}_i$ are mutually independent (circular complex Gaussian) white noise, a single spectral sample \tilde{x}_i is of the form $\sqrt{A_j I_s} z_f z_g + \sqrt{I_n} z_b$, where $z_f \equiv (\tilde{f} * \tilde{\epsilon})_i$, $z_g \equiv (\tilde{g} * \tilde{\eta})_i$, and $z_b \equiv \tilde{\beta}_i$ are each circular complex Gaussian random variables with unit variance. If the scintillation is held fixed (i.e. $z_g = \text{const.}$), then the intensity $|\tilde{x}_i|^2$ is drawn from an exponential distribution with scale $\bar{I}_j \equiv A_j I_s |z_g|^2 + I_n$.

For interferometric visibility, the observer measures the covariance of the electric fields at two stations, which we denote by unprimed and primed variables: $V_i \equiv \tilde{x}_i \tilde{x}'_i^*$ (Thompson et al., 2001). The electric fields at the two stations arise from identical intrinsic emission, $\tilde{f}' * \tilde{\epsilon}' = \tilde{f} * \tilde{\epsilon}$; however, a difference in sensitivity

or gain between the stations will affect the overall scale: $I_s \neq I'_s$. The background noise is independent ($\langle z_b z_b^* \rangle = 0$) and with different variance ($I_n \neq I'_n$) at the two stations. Finally, the stochastic part of the propagation will also differ, with a baseline-dependent correlation $\rho_g \equiv \langle z_g z_g^* \rangle$.

Hence, the average of N visibilities from different pulses takes the form

$$V = \frac{1}{N} \sum_{j=1}^N \left(\sqrt{A_j I_s} z_{f,j} z_g + \sqrt{I_n} z_{b,j} \right) \left(\sqrt{A_j I'_s} z'_{f,j} z'_g + \sqrt{I'_n} z'_{b,j} \right)^*. \quad (3.3)$$

Even in the zero-baseline limit ($z'_g = z_g$), Eq. 3.3 differs from the corresponding intensity result because of the assumption of independent background noise at the stations.

As Eq. 3.3 shows, the measured visibility is the average of N random variables, each of which is the product of two correlated circular complex Gaussian random variables with respective variances $\bar{I}_j \equiv A_j I_s |z_g|^2 + I_n$ and $\bar{I}'_j \equiv A_j I'_s |z'_g|^2 + I'_n$ and correlation

$$\rho \equiv z_g z_g^* A_j \sqrt{\frac{I_s I'_s}{\bar{I}_j \bar{I}'_j}}. \quad (3.4)$$

This correlation changes with scintillation and is complex because of covariance between the real and imaginary part of electric fields at the two stations.

For pulsar observations, one can examine the mean of the off-pulse and on-pulse spectra at each station to estimate the parameters I_s , I'_s , I_n , I'_n , and A_j . These measurements fully characterize the visibility statistics of Eq. 3.3.

3.2.2 Moments and Noise of Snapshot Visibilities

Using Eq. 3.3, we can evaluate moments of the visibility distribution for a “snapshot image” (i.e. the scintillation variables z_g and z'_g are held fixed). These moments include the effects of pulsar variability and self-noise. For example,

$$\begin{aligned} \langle V \rangle &= \langle A \rangle_N \sqrt{I_s I'_s} z_g z'_g{}^* & (3.5) \\ \langle \text{Re}(V)^2 \rangle &= \frac{I_n I'_n}{2N} + \frac{\langle A \rangle_N}{2N} (I_s I'_n |z_g|^2 + I'_s I_n |z'_g|^2) + \left(\frac{\langle A^2 \rangle_N}{N} + \langle A \rangle_N^2 \right) I_s I'_s \text{Re} [z_g z'_g{}^*]^2 \\ \langle \text{Im}(V)^2 \rangle &= \frac{I_n I'_n}{2N} + \frac{\langle A \rangle_N}{2N} (I_s I'_n |z_g|^2 + I'_s I_n |z'_g|^2) + \left(\frac{\langle A^2 \rangle_N}{N} + \langle A \rangle_N^2 \right) I_s I'_s \text{Im} [z_g z'_g{}^*]^2. \end{aligned}$$

These expressions present ensemble averages over the noise of the pulsar and background, while the set of N pulse amplitudes $\{A_j\}$ and the scintillation factors are held fixed; $\langle \dots \rangle$ denotes the average over noise, whereas $\langle \dots \rangle_N$ denotes the average over the N pulse amplitudes.

We can also quantify the noise using these moments. Within a single scintillation element, the noise takes the form

$$\begin{aligned}
\langle |\delta V|^2 \rangle &\equiv \langle |V - \langle V \rangle|^2 \rangle & (3.6) \\
&= \frac{I_n I'_n}{N} + \frac{1}{N} \left(\left| \frac{z_g}{z'_g} \right| \sqrt{\frac{I_s}{I'_s}} I'_n + \left| \frac{z'_g}{z_g} \right| \sqrt{\frac{I'_s}{I_s}} I_n \right) |\langle V \rangle| + \frac{1}{N} \left(1 + \frac{\langle \delta A^2 \rangle_N}{\langle A \rangle_N^2} \right) |\langle V \rangle|^2 \\
&\equiv 2b_0 + 2b_1 |\langle V \rangle| + b_2 |\langle V \rangle|^2.
\end{aligned}$$

The noise is a quadratic function of the signal; hence, pulsar field statistics are heteroscedastic (Gwinn et al., 2011, 2012a). In particular, this equation demonstrates the contribution of the source to the noise, as originally investigated by Dicke (1946) and described by the familiar radiometer equation. Observe that, for the special case of a zero-baseline interferometer, the noise coefficients, b_i , are independent of the particular scintillation element $\{z_g, z'_g\}$.

We can similarly obtain the variances parallel and perpendicular to the mean visibility:

$$\begin{aligned}
\langle \delta V_{\parallel}^2 \rangle &= b_0 + b_1 |\langle V \rangle| + b_2 |\langle V \rangle|^2, & (3.7) \\
\langle \delta V_{\perp}^2 \rangle &= b_0 + b_1 |\langle V \rangle|.
\end{aligned}$$

Thus, the noise scales quadratically in phase with the signal but only scales linearly at quadrature to the signal. Figure 3.1 illustrates this noise behavior.

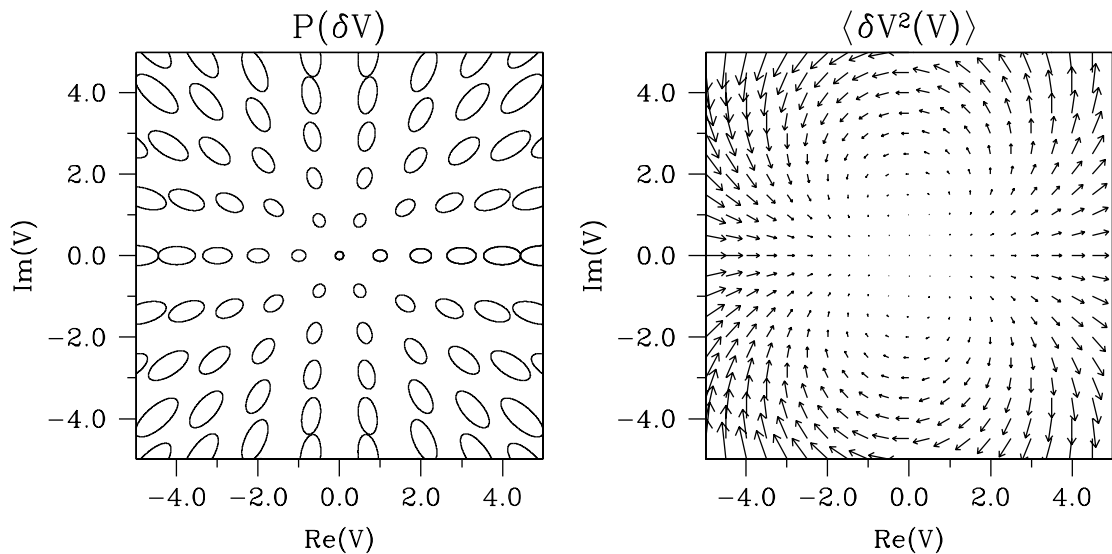


Figure 3.1: Characteristics of complex noise δV for snapshot visibilities. (*left*) Ellipses denote the standard deviation of the Gaussian distribution of noise, centered on the mean visibility. The major axis is oriented with the phase of the visibility and scales quadratically with the signal, while the minor axis scales linearly with the signal (see §3.2.2). The plotted noise corresponds to noise on a short baseline with all source and background intensities unity, and $N = 100$. (*right*) Average complex noise $\langle \delta V^2(V) \rangle$, estimated as described in §3.2.7. The increasing vector length with $|V|$ shows the increasing influence of self-noise, while the change in direction reflects the varying orientation of the noise ellipse.

Because they neatly separate the contributions of the background and source, the noise coefficients provide a valuable mechanism to study and quantify the various types of noise. The self-noise coefficient, b_2 , is particularly useful because it contains information about the intrinsic variability, which does not affect the average spectrum or correlation function (Gwinn & Johnson, 2011). Other types of noise, such as quantization noise (Cole, 1968; Thompson et al., 2001; Jenet & Anderson, 1998), will modify the coefficients but preserve the quadratic form (Gwinn, 2006). In §3.2.7, we describe a procedure to estimate the self-noise.

3.2.3 Approximating the Visibility Statistics within a Scintillation Snapshot

We now derive the PDF of visibility for samples that are collected and averaged within a single scintillation snapshot, characterized by $\{z_g, z'_g\}$. Because the field statistics take a rather general form, $P(V|z_g, z'_g)$ is simply the N -fold convolution of the distribution of the product of correlated complex Gaussian random variables; we relegate the derivation and details of this distribution to the appendix (in particular, §3.5.1).

We also present several approximation strategies, because the convolution of visibilities that are not statistically identical has no convenient analytical form. These strategies provide accuracy that is sufficient for most applications and constitute the analytical foundation for our subsequent results. Moreover, the first approximation that we derive, the i.i.d. approximation, is exact for $N = 1$.

3.2.3.1 The i.i.d. Approximation

We derive our first approximation by assuming that the averaged visibilities for each set of N pulses are independent and identically distributed (i.i.d.). To achieve this condition, we treat the pulse amplitudes as constant for each set of N averaged visibilities: $A_j \mapsto A \equiv \langle A \rangle_N$. Nevertheless, this approximation preserves some

information about the pulsar variability; the i.i.d. approximation is exact when $N = 1$, for instance.

After this replacement, Eq. 3.41 gives the PDF of visibility:

$$\begin{aligned}
P(V; N | z_g, z'_g) &= \frac{N^{N+1}}{2^N \pi (N-1)!} \frac{(1 - |\rho|^2)^N}{a^{N+1}} |V|^{N-1} K_{N-1} \left(N \frac{|V|}{a} \right) \exp \left(N \frac{\text{Re}[V \rho^*]}{a} \right), \\
\rho &\equiv z_g z'_g{}^* A \sqrt{\frac{I_s I'_s}{\bar{I} \bar{I}'}} , & a &\equiv \frac{(1 - |\rho|^2)}{2} \sqrt{\bar{I} \bar{I}'}, \\
\bar{I} &\equiv A I_s |z_g|^2 + I_n, & \bar{I}' &\equiv A I'_s |z'_g|^2 + I'_n.
\end{aligned} \tag{3.8}$$

In this expression, $K_N(x)$ is the modified Bessel function of the second kind. This approximation and its equivalent for intensity (§2.3.2.1) provide convenient tools for analytic work.

3.2.3.2 The Gaussian Approximation

As the number of averaged samples $N \rightarrow \infty$ within a fixed scintillation pattern, the PDF of visibility approaches an elliptical complex Gaussian distribution with mean $V = \langle A \rangle_N \sqrt{I_s I'_s} z_g z'_g{}^*$ and variances determined by Eq. 3.7. Gwinn et al. (2012a,b) described this limit and result, and verified the noise prescription using observations of the Vela pulsar.

In general, the linear term, b_1 , of the noise polynomial depends weakly on the scintillation $\{z_g, z'_g\}$; however, for a short baseline, the noise ellipse depends only on the mean visibility.

3.2.4 The PDF of Visibility

We now derive the PDF of visibility, when the data explore a representative ensemble of the diffractive scintillation. This result relies on both the PDF of visibility within each scintillation snapshot (§3.2.3) and the PDF of the scintillation random variables $\{z_g, z'_g\}$:

$$P(V; N) = \int P(V; N|z_g, z'_g)P(z_g, z'_g)d^2z_gd^2z'_g. \quad (3.9)$$

Now, z_g and z'_g are drawn from a distribution of circular complex Gaussian random variables with some correlation $\rho_g \equiv \langle z_g z'_g{}^* \rangle_S$. Note that we use the subscripted brackets $\langle \dots \rangle_S$ to designate an ensemble average over the scintillation.

Although a single realization of the scintillation pattern has a complex mean visibility $z_g z'_g{}^*$, we assume that the ensemble-averaged mean visibility $\rho_g \equiv \langle z_g z'_g{}^* \rangle_S$ is real. In practice, this assumption merely reflects an appropriate added, constant phase to the delay model. This mean visibility depends on the baseline, scattered image size, and observing wavelength, and can be expressed in terms of the phase structure function $D_\phi(\mathbf{b})$ of the scattering medium (Tatarskii, 1971; Lee & Jokipii, 1975; Rickett, 1990):

$$\rho_g = \exp \left[-\frac{1}{2} D_\phi(\mathbf{b}) \right]. \quad (3.10)$$

The joint PDF $P(z_g, z'_g)$, the standardized bivariate complex Gaussian distribution, follows easily from a distribution of four correlated (real) Gaussian random variables that correspond to the real and imaginary parts of z_g and z'_g ; see Goodman (1963) or Gwinn (2001), for example. In terms of the scintillation norms, $r \equiv |z_g|$ and $r' \equiv |z'_g|$, and their relative phase $\theta \equiv \arg(z_g z'^*_g)$, we have

$$P(r, r', \theta) = \frac{2}{\pi} \frac{rr'}{(1 - \rho_g^2)} \exp \left[-\frac{(r^2 + r'^2 - 2\rho_g rr' \cos \theta)}{(1 - \rho_g^2)} \right]. \quad (3.11)$$

3.2.4.1 The i.i.d. Approximation

For the i.i.d. approximation (§3.2.3.1), we can further reduce the expression for $P(V; N)$ by integrating θ because $\arg(\rho)$ is the only quantity in Eq. 3.2.3.1 that depends on θ . We then obtain

$$P(V; N) = \frac{N^{N+1}}{2^{N-2} \pi (N-1)!} \frac{|V|^{N-1}}{(1 - \rho_g^2)} \int_0^\infty dr dr' \frac{(1 - |\rho|^2)^N}{a^{N+1}} K_{N-1} \left(N \frac{|V|}{a} \right) \quad (3.12)$$

$$\times rr' \exp \left(-\frac{r^2 + r'^2}{1 - \rho_g^2} \right) I_0 \left(\sqrt{\left(\frac{2\rho_g rr'}{(1 - \rho_g^2)} \right)^2 + \left(\frac{N|\rho V|}{a} \right)^2 + \frac{4N\rho_g}{1 - \rho_g^2} |\rho| rr' \frac{\text{Re}(V)}{a}} \right).$$

In this expression, $I_0(x)$ is the modified Bessel function of the first kind. The visibility projections and their generalizations, such as the projected imaginary variance $\int dV_i V_i^2 P(V)$, similarly follow from the results of §3.5.2. Figure 3.2 illustrates the effects of baseline and signal-to-noise on the projections.

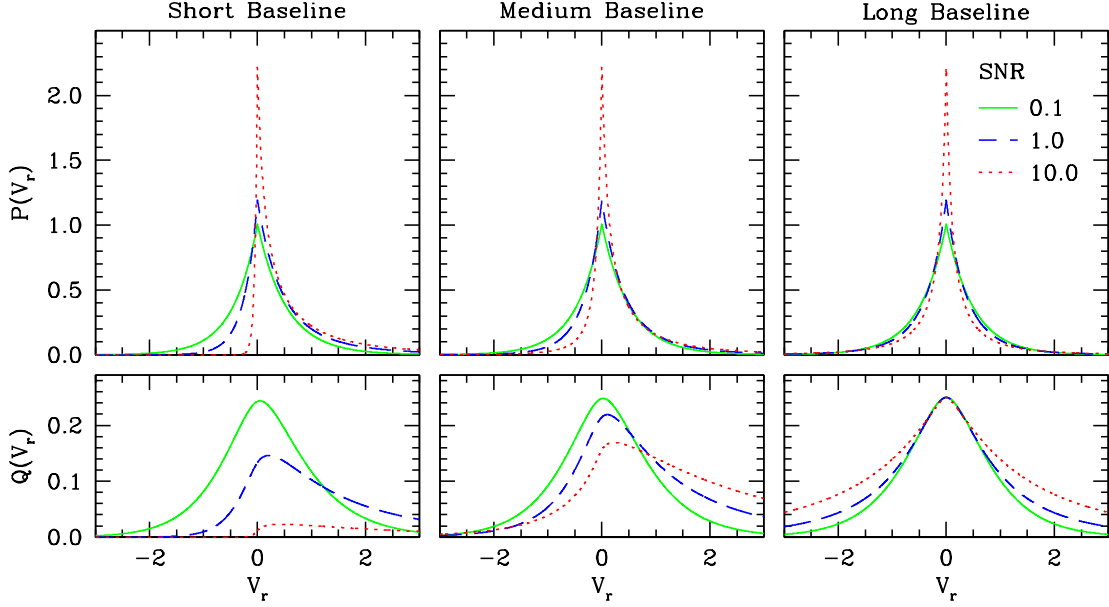


Figure 3.2: Visibility projections as a function of baseline and signal-to-noise (SNR) for $N = 1$. We have set the pulse amplitude A to be unity, the receivers to have identical signal-to-noise ratios ($I_s = I'_s$ and $I_n = I'_n$), and the single-dish intensities to be fixed: $I_s + I_n = 1$. The source contribution can *increase* the variance about the real axis on long baselines as a result of scintillation. This combination of projections demonstrates that, even without averaging, a strong scintillating source may be readily detected regardless of baseline. The short, medium, and long baselines correspond to $\rho_g = 1.0, 0.5,$ and 0.0 , respectively.

3.2.4.2 The Gaussian Approximation

We now include the effects of scintillation for the Gaussian approximation (§3.2.3.2).

The distribution of visibility, after including the scintillation ensemble but before including the effects of noise, can be written (see Eq. 3.39)

$$P(V; N \rightarrow \infty) = \frac{2}{\pi \kappa^2} \frac{1}{(1 - \rho_g^2)} K_0 \left(\frac{2}{(1 - \rho_g^2)} \frac{|V|}{\kappa} \right) \exp \left(\frac{2\rho_g}{(1 - \rho_g^2)} \frac{\text{Re}[V]}{\kappa} \right), \quad (3.13)$$

where $\kappa \equiv \langle A \rangle_N \sqrt{I_s I'_s}$ and $\rho_g \equiv \langle z_g z'_g{}^* \rangle$. Gwinn (2001) described this limit and result.

As noted in §3.2.3.2, the noise only depends on the mean visibility when the baseline is short (relative to the diffractive scale). Hence, the Gaussian approximation, including the scintillation ensemble, becomes

$$P(V; N) \approx \int P(V'; N \rightarrow \infty) P_{\text{noise}}(V - V', V') d^2 V'. \quad (3.14)$$

In this case, $P_{\text{noise}}(V, V_0)$ denotes the elliptical Gaussian distribution of noise centered on V_0 . The orientation of the ellipse is given by the phase of V_0 ; the major and minor axes depend on both V_0 and the noise coefficients $\{b_0, b_1, b_2\}$, as derived in §3.2.2.

From Eq. 3.14, we see that the visibility projections after including the effects of noise can be applied directly to P_{noise} . For example, the real projection is given by

$$P(V_r; N) \approx \int P(V'; N \rightarrow \infty) \left\{ \frac{1}{\sqrt{2\pi}} \frac{1}{\sqrt{b_0 + b_1|V'| + b_2|V'|^2 \cos^2 \phi}} \right. \quad (3.15) \\ \left. \times \exp \left[\frac{-(V_r - V'_r)^2}{2(b_0 + b_1|V'| + b_2|V'|^2 \cos^2 \phi)} \right] \right\} d^2 V',$$

where $\phi \equiv \arg V'$. Gwinn et al. (2012a,b) used these representations to characterize the PDF of visibility for observations of the Vela pulsar.

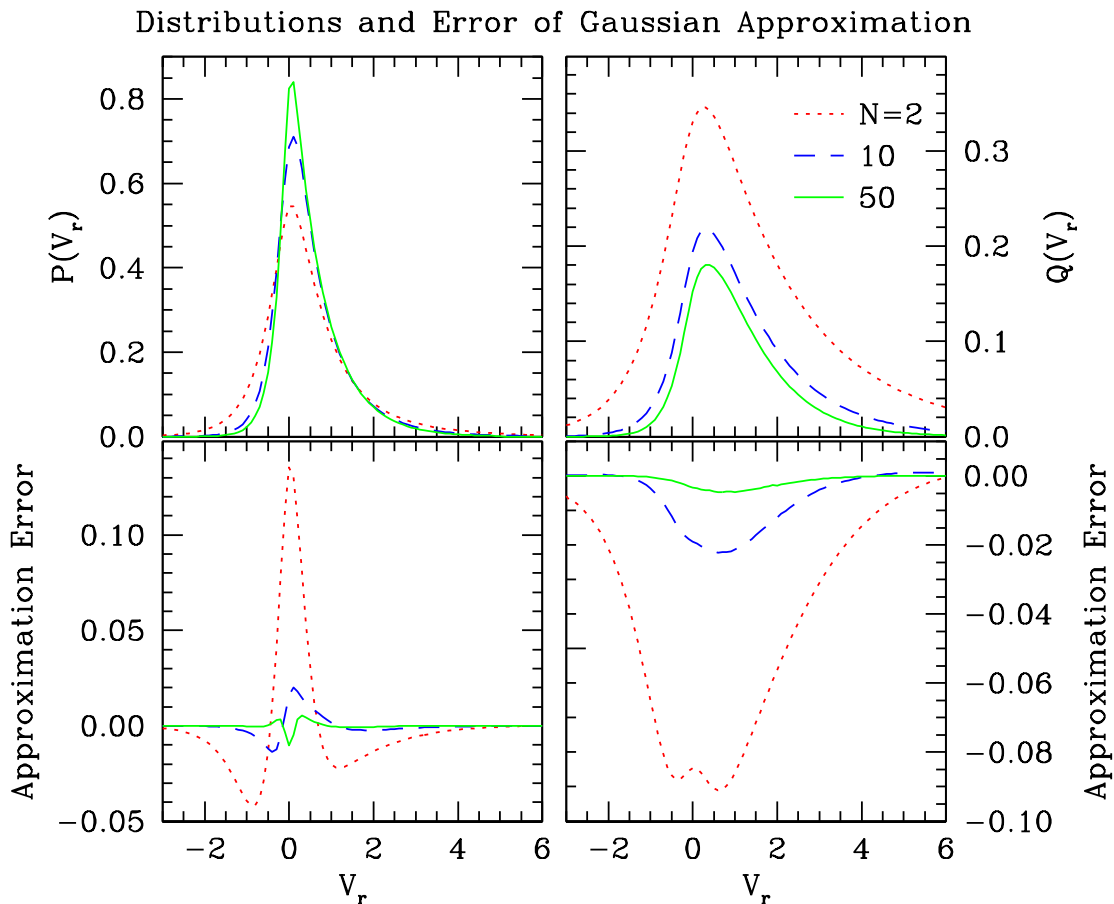


Figure 3.3: Visibility projections $P(V_r)$ and $Q(V_r)$ for $N = 2, 10,$ and $50,$ and the corresponding errors δP and δQ in the Gaussian approximation. We have set the signal-to-noise ratio to unity ($I_s = I'_s = I_n = I'_n = 1$) and assigned a moderate baseline ($\rho_g = 0.5$). We have set all pulse amplitudes to be equal to one, so the i.i.d. approximation is exact.

The Gaussian approximation is also effective on longer baselines, although the noise depends on the scintillation pair $\{z_g, z'_g\}$ rather than just the mean visibility. However, in this case, we simply replace b_1 by its value when $z_g = z'_g$; in this case, the noise only depends on the mean visibility, and Eq. 3.14 applies. Figure 3.3 shows the error in the Gaussian approximation for various degrees of averaging on a moderate baseline.

3.2.5 Examples

Because the form of the visibility PDF is rather opaque, we now refine it for several cases of interest. The zero-baseline interferometer (§3.2.5.1) offers the most substantial reduction of complexity and relates neatly to the analogous results for intensity. At the opposite extreme, an infinite baseline (§3.2.5.2) also leads to a greatly simplified form, albeit with no fundamental decrease in numerical difficulty. Finally, the regime of high signal-to-noise (§3.2.5.3) highlights the influence of self-noise on the PDF and lays the foundation for calculating the asymptotic ($|V| \rightarrow \infty$) dependence (see §3.2.6). For simplicity, we derive all results of this section using the i.i.d. approximation.

3.2.5.1 Zero-Baseline

The zero-baseline limit for visibility is particularly simple: $\rho_g \rightarrow 1$. In this case, $z_g = z'_g$, and the effects of scattering depend only on the scintillation “gain” $G \equiv |z_g|^2$:

$$P(V; N) = \frac{N^{N+1}}{2^N \pi (N-1)!} |V|^{N-1} \quad (3.16)$$

$$\times \int_0^\infty dG \frac{(1 - |\rho|^2)^N}{a^{N+1}} K_{N-1} \left(N \frac{|V|}{a} \right) \exp \left(N \frac{\text{Re}[V\rho^*]}{a} \right) P(G),$$

where $P(G) = e^{-G}$. This representation has two distinct advantages: it requires a single integral, and it can be easily modified to any alternate distribution of scin-

tillation gain, as might occur from an extended emission region or weak scattering, for example.

We can also use the results of §3.5.2 to evaluate projections of the visibility distribution without requiring an additional numerical integral:

$$\begin{aligned}
 P(V_r; N) &= \frac{N}{(N-1)!} \int_0^\infty dG \frac{1}{a} \left[\frac{N}{2} (1-\rho^2) \frac{|V_r|}{a} \right]^N k_{N-1} \left(N \frac{|V_r|}{a} \right) e^{N\rho \frac{V_r}{a}} P(G), \quad (3.17) \\
 Q(V_r; N) &= \frac{2}{N!} \int_0^\infty dG \frac{a}{(1-\rho^2)} \left[\frac{N}{2} (1-\rho^2) \frac{|V_r|}{a} \right]^{N+1} k_N \left(N \frac{|V_r|}{a} \right) e^{N\rho \frac{V_r}{a}} P(G).
 \end{aligned}$$

In these expressions, $k_N(x)$ is the modified spherical Bessel function of the second kind (Arfken & Weber, 2005).

As the averaging increases, the distribution of visibility approaches $P(G)$:

$$P(V; N \rightarrow \infty) = \frac{1}{\langle V \rangle} e^{-\text{Re}[V]/\langle V \rangle} \theta(\text{Re}[V]) \delta(\text{Im}[V]), \quad (3.18)$$

where $\theta(x)$ is the Heaviside function, and $\delta(x)$ is the Dirac delta function.

3.2.5.2 Long-Baseline

On a sufficiently long baseline, the interferometer completely resolves the scattering disk, and the respective propagation kernels at the two stations become completely independent: $\rho_g \rightarrow 0$. Although ground-based VLBI can only marginally achieve this regime for a few of the most heavily scattered pulsars at meter and decimeter wavelengths (e.g. Gwinn et al., 1993a), space VLBI with RadioAstron

can easily resolve the scattering disks of many pulsars (Kardashev, 2009). A precise understanding of the visibility statistics for ultra-long baselines will help to maximize the information that can be gleaned from space VLBI.

In this limit, Eq. 3.12 becomes

$$P(V; N) = \frac{N^{N+1}}{2^{N-2}\pi(N-1)!} |V|^{N-1} \quad (3.19)$$

$$\times \int_0^\infty dr dr' \frac{(1-|\rho|^2)^N}{a^{N+1}} K_{N-1} \left(N \frac{|V|}{a} \right) I_0 \left(N |\rho| \frac{|V|}{a} \right) r r' e^{-(r^2+r'^2)}.$$

Observe that this distribution depends only on $|V|$, as necessitated by the phase invariance of this limit. Although the mean visibility is zero, the effects of scintillation can still be substantial, as Figure 3.2 illustrates.

3.2.5.3 High Signal-to-Noise

In the limit of infinite signal-to-noise, the fields at two stations will exhibit identical noise, multiplied by their respective complex scintillation gains. In terms of the field statistics (§3.2.1), each visibility is the average of N exponential random variables with means $A_j \sqrt{I_s I'_s} z_g z'_g{}^*$.

For simplicity, we apply the i.i.d. approximation. In this case, each averaged visibility is drawn from an Erlang distribution, multiplied by the scintillation gain, which rotates the phase to $\arg(z_g z'_g{}^*)$. Expressed in terms of the magnitude and

phase of the visibility, $V = |V|e^{i\phi}$, this distribution is

$$P(|V|, \phi; N | z_g, z'_g) = \frac{N^N}{(N-1)!} \frac{|V|^{N-1}}{(A\sqrt{I_s I'_s} r r')^N} \exp\left[-N \frac{|V|}{A\sqrt{I_s I'_s} r r'}\right] \delta(\phi - \theta). \quad (3.20)$$

The definitions of r , r' , and θ are equivalent to those in §3.2.3.1. When combined with the scintillation ensemble, θ can be trivially integrated against its delta function to give

$$\begin{aligned} P(|V|, \phi; N) &= \frac{2}{\pi} \frac{N^N}{(N-1)!} \frac{1}{(1-\rho_g^2)} \frac{|V|^{N-1}}{(A\sqrt{I_s I'_s})^N} \quad (3.21) \\ &\times \int_0^\infty dr dr' \frac{1}{(r r')^{N-1}} \exp\left[-\frac{N|V|}{A\sqrt{I_s I'_s} r r'} - \frac{(r^2 + r'^2 - 2\rho_g r r' \cos \phi)}{(1-\rho_g^2)}\right] \\ &= \frac{2N}{\pi(N-1)!} \frac{1}{(1-\rho_g^2)} \frac{1}{A\sqrt{I_s I'_s}} \left(\frac{2N|V|}{A\sqrt{I_s I'_s}}\right)^{\frac{N}{2}} \\ &\times \int_0^{\pi/2} d\psi \frac{1}{\beta(\psi)} \left[\frac{\beta(\psi)}{\sin(2\psi)}\right]^{\frac{N}{2}} K_{N-2}\left(2\sqrt{2N \frac{\beta(\psi)}{\sin(2\psi)} \frac{|V|}{A\sqrt{I_s I'_s}}}\right), \\ \beta(\psi) &\equiv \frac{1 - \rho_g \cos \phi \sin(2\psi)}{1 - \rho_g^2}. \end{aligned}$$

To obtain the second equality, we transformed to polar coordinates $\{r = \ell \cos \psi, r' = \ell \sin \psi\}$ and integrated over ℓ . Thus, as for the zero-baseline case, we have reduced the integration to a single dimension. We next use this form to determine the asymptotic behavior of $P(V)$.

3.2.6 Asymptotic Behavior

We now derive the behavior of $P(V; N)$ as $|V| \rightarrow \infty$. To proceed, we first consider the high signal-to-noise results. At large $|V|$, the Bessel function of Eq. 3.21 approaches an exponential, so we can apply the method of steepest descent to approximate the integral over ψ (Arfken & Weber, 2005):

$$P(|V| \rightarrow \infty, \phi; N) \propto |V|^{\frac{N-1}{2}} \exp \left[-2\sqrt{2N \left(\frac{1 - \rho_g \cos \phi}{1 - \rho_g^2} \right) \frac{|V|}{A\sqrt{I_s I'_s}}} \right]. \quad (3.22)$$

Here, the constant of proportionality is also a function of ϕ .

On the other hand, the distribution of visibility for purely background noise has the asymptotic form (see Eq. 3.41)

$$\begin{aligned} P(|V| \rightarrow \infty, \phi; N, I_s = I'_s = 0) &\propto |V|^N K_{N-1} \left(\frac{2N|V|}{\sqrt{I_n I'_n}} \right) \\ &\sim |V|^{N-1/2} \exp \left(-\frac{2N|V|}{\sqrt{I_n I'_n}} \right). \end{aligned} \quad (3.23)$$

Thus, the stronger, scintillation-induced “skirt” of source power will dominate the PDF of visibility in the asymptotic regime defined by

$$|V| \gg \frac{2}{N} \left(\frac{1 - \rho_g \cos \phi}{1 - \rho_g^2} \right) \frac{I_n I'_n}{A\sqrt{I_s I'_s}}. \quad (3.24)$$

Of course, the projections also reflect this remarkable behavior. For example, the projection onto $V_r \equiv \text{Re}(V)$ follows by applying the method of steepest descent to these asymptotic forms. We thereby obtain

$$\begin{aligned}
P(V_r \rightarrow \pm\infty; N, I_s, I'_s > 0) &\propto |V_r|^{\frac{N}{2}-\frac{3}{4}} \exp \left[-2\sqrt{2N \left(\frac{1}{1 + \text{sign}(V_r)\rho_g} \right) \frac{|V_r|}{A\sqrt{I_s I'_s}}} \right], \\
P(V_r \rightarrow \pm\infty; N, I_s = I'_s = 0) &\propto |V_r|^{N-1} \exp \left(-\frac{2N|V_r|}{\sqrt{I_n I'_n}} \right). \tag{3.25}
\end{aligned}$$

Once again, a scintillating source extends the wings and introduces a baseline-dependent asymmetry. In this case, the constant of proportionality is a function of $\text{sign}(V_r)$, and the asymptotic regime is determined by

$$|V_r| \gg \frac{2}{N} \frac{1}{(1 + \text{sign}(V_r)\rho_g)} \frac{I_n I'_n}{A\sqrt{I_s I'_s}}. \tag{3.26}$$

Figure 3.4 demonstrates this asymptotic behavior of the projections on various baselines.

Observe that both these asymptotic forms have poles for $\rho_g = \pm 1$. This behavior reflects the fact that, in these cases, the signal power is restricted to the real half-line that matches the sign of the mean visibility, so the asymptotic behavior elsewhere corresponds to that of pure background noise.

Perhaps most surprisingly, in the limit $N \rightarrow \infty$ (given by Eq. 3.13), the asymptotic behavior is exponential, regardless of the signal-to-noise. Hence, the

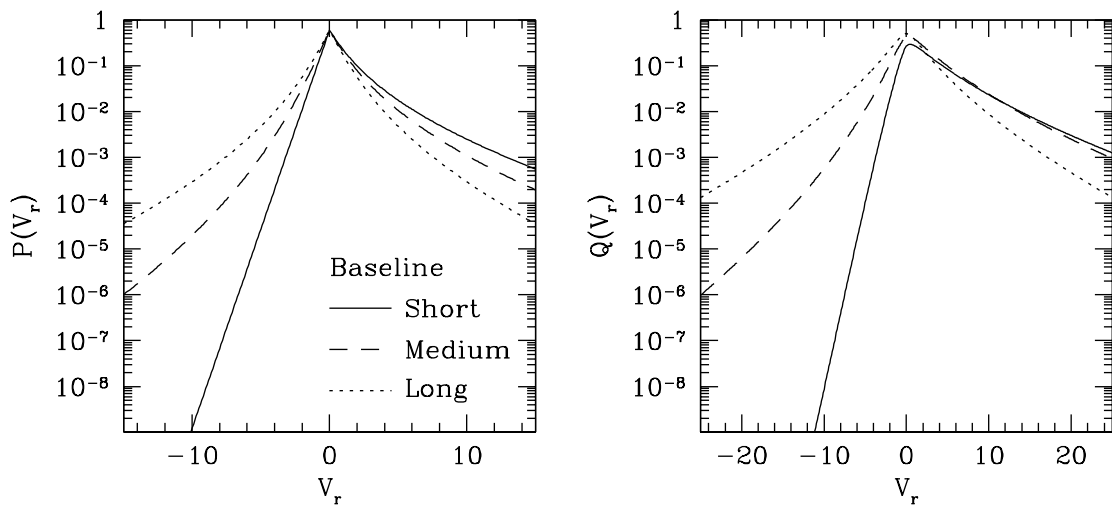


Figure 3.4: Exact projections $P(V_r)$ and $Q(V_r)$ for $N = 1$; the source and background amplitudes are unity. The broad scintillation-induced wings are distinctive at large $|V_r|$. However, for zero-baseline and negative V_r , there is only the exponentially-falling noise contribution, reflecting the absence of source power on that half-line and, mathematically, the singularities in Eqs. 3.22 & 3.25.

broad $\exp(-\sqrt{|V|})$ skirt arises from the delicate interplay of the scintillation and the self-noise.

3.2.7 Estimation of the Self-Noise

As a last application of these visibility statistics, we now present a prescription that can be applied to quantify self-noise. As we have discussed, self-noise provides a powerful diagnostic of a signal, particularly when characterizing intrinsic variability. For example, source variability on timescales shorter than t_{acc} induces correlations in the spectral noise, without modifying the mean spectrum (Gwinn & Johnson, 2011). We now outline one technique that estimates self-noise and thereby facilitates a detection of such correlations.

Our method is similar to its analog for intensity (§2.5.2). Namely, we use pairs of nearby samples to calculate finite estimates of the signal and noise. Each pair of samples is assumed to be within a single scintillation element. We will assume that the pair consists of samples with uncorrelated self-noise (e.g. pairs from different pulses, or from the same pulse with negligible intrinsic modulation). We calculate the noise in pairs of samples as a function of their mean. However, because the visibility is complex, the noise must be treated as a vector quantity as it has different behavior in phase and at quadrature with the signal (see §3.2.2 and Figure 3.1). We find it advantageous to work with analytical expressions of the involved complex quantities and, thus, define

$$\delta V^2(V) \equiv 2 \left\langle \left(V_1 - \frac{V_1 + V_2}{2} \right)^2 \right\rangle, \quad V \equiv \frac{V_1 + V_2}{2}. \quad (3.27)$$

We again work within the i.i.d. approximation. The distribution of visibility is then given by Eq. 3.41, and we obtain,

$$\delta V^2(V) = \frac{V^2}{N + \frac{1}{2}}. \quad (3.28)$$

As for intensity, this method for estimating the self-noise agrees with the exact expression with $N \rightarrow N + 1/2$.

If the averaged visibilities are from different pulses, then pulse-to-pulse variations can contribute additional noise. If the averaged visibilities are from the

same pulses, then intrinsic variations on timescales shorter than t_{acc} induce correlations in self-noise, and thereby decrease the measured noise; if $N > 1$ then pulse-to-pulse variations within the averaging will increase the noise. Gwinn et al. (2011) applied similar tests to infer short-timescale variability ($< 300\mu\text{s}$) of PSR B0834+06.

3.3 Effects of an Extended Emission Region on the Visibility PDF

We now derive the modifications to the PDF of visibility from a spatially-extended emission region. Such emission superimposes many slightly-offset copies of the diffraction pattern at the observer, suppressing the observed scintillation. Optical scintillation provides a familiar demonstration: “Stars twinkle, but planets do not.” Emission extending over a region much larger than the diffractive scale r_d (see §3.1.1) quenches the scintillation, and so diffractive scintillation studies can effectively probe emission scales $\lesssim r_d$.

3.3.1 The Effects of an Extended Emission Region on the Field Statistics

If the emission spans a transverse size $\ll r_d$, then the modification to the field statistics can be derived quite generally. Explicitly, in terms of transverse source

coordinates \mathbf{s} and the notation of §3.2.1, the observed electric field takes the form

$$\tilde{x}_i = \left\{ \int d^2\mathbf{s} \sqrt{A(\mathbf{s})} \overline{I_s} z_f(\mathbf{s}) z_g(\mathbf{s}) \right\} + \sqrt{I_n} z_b. \quad (3.29)$$

We set the origin of the coordinates \mathbf{s} so that $\int d^2\mathbf{s} \mathbf{s} A(\mathbf{s}) = \mathbf{0}$. Because the source intensity $I(\mathbf{s})$ is assumed to be confined within a region $\ll r_d$, $z_g(\mathbf{s})$ will only vary slightly and we may expand to linear order: $z_g(\mathbf{s}) \approx z_g(\mathbf{0}) + (\mathbf{s} \cdot \nabla) z_g|_{s=0}$.

The source term in Eq. 3.29 is then a convolution of three complex Gaussian random variables. Because of our choice of origin for \mathbf{s} , at linear order these three random variables are mutually uncorrelated during a fixed scintillation pattern. In addition, the scintillation random variable, $z_g(\mathbf{s})$, is uncorrelated with its spatial derivatives, so the scales of the three respective variances are also mutually independent at linear order. Combining these characteristics for the pair of receivers then gives the form of the visibility field statistics to leading order:

$$\begin{aligned} V \approx & \frac{1}{N} \frac{1}{1 + \gamma_{s,1} + \gamma_{s,2}} \sum_{j=1}^N \left[\sqrt{A_j I_s} (z_{f,j} z_g + \sqrt{\gamma_{s,1}} z_{f,1,j} z_{g,1} + \sqrt{\gamma_{s,2}} z_{f,2,j} z_{g,2}) + \sqrt{I_n} z_{b,j} \right] \\ & \times \left[\sqrt{A_j I'_s} (z'_{f,j} z'_g + \sqrt{\gamma_{s,1}} z'_{f,1,j} z'_{g,1} + \sqrt{\gamma_{s,2}} z'_{f,2,j} z'_{g,2}) + \sqrt{I'_n} z'_{b,j} \right]^*. \end{aligned} \quad (3.30)$$

Here, the paired scintillation random variables are correlated, $\rho_g \equiv \langle z_g z_g'^* \rangle$ and $\rho_{g,i} \equiv \langle z_{g,i} z_{g,i}'^* \rangle$, but all other pairs of random variables $\{z_x, z_y\}$ are uncorrelated.

We have chosen the scaling prefactor so that the intensity measured by either receiver is unaffected by the extent of the emission. Our expansion parameters, the

dimensionless subsidiary scales $\gamma_{s,i} \ll 1$, contain information about the transverse extent of the source emission. More specifically, these scales are proportional to the spatial standard deviation of *integrated* flux density. For example, spatially-offset, pointlike emission sites need only to emit within the same accumulation time, but not necessarily at the same retarded time, to affect the scintillation statistics. Hence, even for emission that is highly beamed and, thus, instantaneously pointlike, this method can identify a transverse size that relates to the emission altitude; see Johnson et al. (2012).

Within a fixed scintillation pattern, Eq. 3.30 is the N -fold convolution of products of complex circular Gaussian random variables, as for a point source. Thus, applying the i.i.d. approximation, we see that the PDF of visibility within each scintillation snapshot takes the same form as Eq. 3.2.3.1. However, the correlation of each multiplied pair depends on the extended emission region; the subsequent inclusion of the scintillation ensemble is complicated by the different correlations for each scintillation factor: $\rho_g \neq \rho_{g,1} \neq \rho_{g,2}$. The appropriate correlation and respective intensities of the multiplied terms are

$$\begin{aligned} \rho &= \left(\frac{z_g z_g'^* + \gamma_{s,1} z_{g,1} z_{g,1}'^* + \gamma_{s,2} z_{g,2} z_{g,2}'^*}{1 + \gamma_{s,1} + \gamma_{s,2}} \right) A \sqrt{\frac{I_s I_s'}{\bar{I} \bar{I}'}} , & (3.31) \\ \bar{I} &\equiv A I_s \left(\frac{|z_g|^2 + \gamma_{s,1} |z_{g,1}|^2 + \gamma_{s,2} |z_{g,2}|^2}{1 + \gamma_{s,1} + \gamma_{s,2}} \right) + I_n , \\ \bar{I}' &\equiv A I_s' \left(\frac{|z_g'|^2 + \gamma_{s,1} |z_{g,1}'|^2 + \gamma_{s,2} |z_{g,2}'|^2}{1 + \gamma_{s,1} + \gamma_{s,2}} \right) + I_n' . \end{aligned}$$

Also, observe that the mean visibility is weakly diminished by a finite source emission size:

$$\langle V \rangle \equiv \frac{\rho_g + \gamma_{s,1}\rho_{g,1} + \gamma_{s,2}\rho_{g,2}}{1 + \gamma_{s,1} + \gamma_{s,2}} \leq \langle V \rangle_{\gamma_{s,i}=0}. \quad (3.32)$$

3.3.2 The Relation Between the Emission Region and the Dimensionless Size Parameters $\gamma_{s,i}$

The precise correspondence between the source dimensions and $\gamma_{s,i}$ requires knowledge of the distribution of scattering material. The relationship between the correlations $\{\rho_g, \rho_{g,i}\}$ and the observing baseline likewise depends on the scattering assumptions. For example, by assuming a square-law phase structure function, Gwinn (2001) derived the relations

$$\begin{aligned} \gamma_{s,i} &= \left(\frac{D}{R} k \theta_i \sigma_i \right)^2, \\ \rho_{g,i} &\approx [1 - (b_i k \theta)^2] \exp \left[-\frac{1}{2} (|\mathbf{b}| k \theta)^2 \right] = [1 - (b_i k \theta)^2] \rho_g. \end{aligned} \quad (3.33)$$

Here, D is the characteristic observer-scatterer distance, R is the characteristic source-scatterer distance, k is the observing wavenumber, θ_i is the angular size of the scattering disk along \hat{s}_i , and σ_i is the standard deviation of the (integrated) distribution of source intensity along \hat{s}_i . The scintillation correlations also depend on the baseline length $|\mathbf{b}|$ and its projections b_i along \hat{s}_i . Consequently, for

baselines much shorter than the diffractive scale, the three correlations are nearly equal. Thus, the dimensionless size parameters $\gamma_{s,i}$ give the squared size of the source in orthogonal directions \hat{s}_i , in units of the magnified diffractive scale.

3.3.3 Approximate Evaluation of the PDF of Visibility

We now apply the i.i.d. approximation to estimate the PDF of visibility, including the effects of an extended emission region. Namely, we combine the form of the PDF of visibility within each scintillation snapshot, given by Eq. 3.2.3.1, with the distribution of each scintillation random variable:

$$P(V; N, \gamma_{s,1}, \gamma_{s,2}) = \frac{N^{N+1}}{2^N \pi (N-1)!} |V|^{N-1} \int d^3 \mathbf{r} d^3 \mathbf{r}_1 d^3 \mathbf{r}_2 \frac{(1 - |\rho|^2)^N}{a^{N+1}} K_{N-1} \left(N \frac{|V|}{a} \right) \times \exp \left(N \frac{\text{Re}[V \rho^*]}{a} \right) P(r, r', \theta) P(r_1, r'_1, \theta_1) P(r_2, r'_2, \theta_2). \quad (3.34)$$

Here, we have shifted to polar coordinates for each pair of scintillation gains; e.g. $\mathbf{r} \equiv \{r \equiv |z_g|, r' \equiv |z'_g|, \theta \equiv \arg(z_g z'^*_g)\}$. Eq. 3.11 then gives the distribution $P(r, r', \theta)$ of each triplet. Also, ρ , \bar{I} , and \bar{I}' are defined by Eq. 3.31, and a is then as in Eq. 3.2.3.1; these variables depend on the integration variables, which account for the scintillation.

While typical numerical techniques for high-dimensional integrals can evaluate Eq. 3.34, they are computationally expensive and unenlightening. Gwinn et al. (2012b) derived an efficient technique, suitable for $N \gtrsim 20$, using the Gaussian approximation (§3.2.3.2). Their method requires only a one-dimensional integral

and a two-dimensional grid convolution, which accounts for the signal-dependent noise (see §3.2.4.2).

However, because we are interested in small values of averaging, especially $N = 1$, we present an alternative. Namely, for a small source, anisotropic emission size effects ($\gamma_{s,1} \neq \gamma_{s,2}$) only weakly modify those of an equivalent isotropic region. For the analogous effects on intensity, for example, the effects of anisotropy are quadratic in $\gamma_{s,i}$, and so we have worked in terms of an equivalent isotropic size: $\gamma_s \equiv \gamma_{s,1} = \gamma_{s,2}$. For our purposes, a one-dimensional emission region is advantageous to characterize the dominant effects of size because it obviates the integration over $P(z_{g,2}, z'_{g,2})$, thereby reducing the integral of Eq. 3.34 to six dimensions.

In addition, by using the results of §3.5.2, we can evaluate projections of the visibility distribution without increasing the number of required integrations. For example, the distribution of $V_r \equiv \text{Re}(V)$ is

$$\begin{aligned}
 P(V_r; N, \gamma_{s,1}, \gamma_{s,2}) &= \frac{N^{N+1}}{2^N (N-1)!} |V_r|^N \int d^3 \mathbf{r} d^3 \mathbf{r}_1 d^3 \mathbf{r}_2 \frac{\sqrt{1 - \rho_i^2}}{a} \left(\frac{1 - |\rho|^2}{a \sqrt{1 - \rho_i^2}} \right)^N \quad (3.35) \\
 &\times k_{N-1} \left(N \sqrt{1 - \rho_i^2} \frac{|V_r|}{a} \right) e^{N \rho_r \frac{V_r}{a}} P(r, r', \theta) P(r_1, r'_1, \theta_1) P(r_2, r'_2, \theta_2).
 \end{aligned}$$

Here, and elsewhere, the subscripts r and i denote the real and imaginary part, respectively.

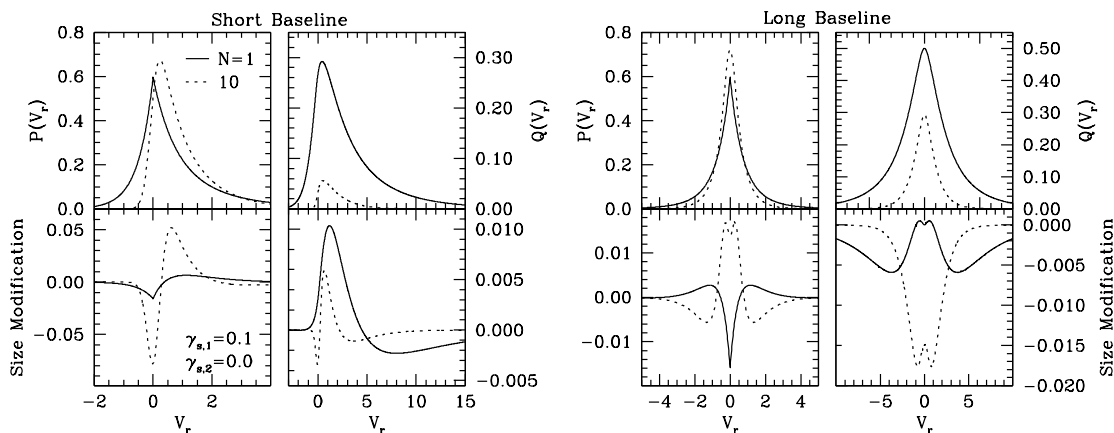


Figure 3.5: Visibility projections for a point source and their modifications (e.g. $P(V_r; \gamma_{s,i}) - P(V_r; \gamma_{s,i} = 0)$) corresponding to an elongated emission region with $\gamma_{s,1} = 0.1$ and $\gamma_{s,2} = 0.0$. The source and background intensities are unity, as are all the pulse amplitude factors A_j . The modest averaging, $N = 10$, reveals the W-shaped signature of emission size observed by Gwinn et al. (2012b).

Figure 3.5 shows the effects of an extended emission region on the visibility projections $P(V_r)$ and $Q(V_r)$, for both short and long baselines.

3.3.4 The Short Baseline Limit

The special case of a short baseline vastly simplifies the effects of an extended emission. In this case, the quantities in Eq. 3.31 only depend on the single scintillation “gain” \mathcal{G} :

$$\mathcal{G} \equiv \frac{|z_g|^2 + \gamma_{s,1}|z_{g,1}|^2 + \gamma_{s,2}|z_{g,2}|^2}{1 + \gamma_{s,1} + \gamma_{s,2}}. \quad (3.36)$$

This quantity is the convolution of three independent exponential random variables. The PDF of \mathcal{G} is then (see Eq. 2.31)

$$P(\mathcal{G}) = \sum_{j=1}^3 \left(\frac{\lambda_j}{\prod_{\substack{\ell=1 \\ \ell \neq j}}^3 (\lambda_j - \lambda_\ell)} \right) e^{-\mathcal{G}/\lambda_j}, \quad (3.37)$$

$$\{\lambda_1, \lambda_2, \lambda_3\} \equiv \frac{1}{1 + \gamma_{s,1} + \gamma_{s,2}} \{1, \gamma_{s,1}, \gamma_{s,2}\}.$$

The PDF of visibility is then given by Eq. 3.16, with the substitution $G \rightarrow \mathcal{G}$, and the projections follow likewise. In fact, because $\rho \in \mathbb{R}$, the projections become especially tractable:

$$P(V_r) = \frac{N}{(N-1)!} \int_0^\infty d\mathcal{G} \frac{1}{a} \left[\frac{N}{2} (1 - \rho^2) \frac{|V_r|}{a} \right]^N k_{N-1} \left(N \frac{|V_r|}{a} \right) e^{N\rho \frac{V_r}{a}} P(\mathcal{G}), \quad (3.38)$$

$$Q(V_r) = \frac{2}{N!} \int_0^\infty d\mathcal{G} \frac{a}{(1 - \rho^2)} \left[\frac{N}{2} (1 - \rho^2) \frac{|V_r|}{a} \right]^{N+1} k_N \left(N \frac{|V_r|}{a} \right) e^{N\rho \frac{V_r}{a}} P(\mathcal{G}).$$

Figure 3.5 illustrates how an extended emission region modifies these projections. Increased averaging tends to pronounce the effects on the real projection but not the projected imaginary variance because of the decreasing variance with averaging. Thus, $P(V_r)$ tends to be a more sensitive indicator of size than $Q(V_r)$, as noted by Gwinn et al. (2012b).

3.4 Summary

We have derived the PDF of visibility for a strongly-scintillating source, with particular attention to spectral resolution at or near the Nyquist limit. We have incorporated background- and self-noise, source variability, the possibility of spatially-extended source emission, and arbitrary temporal averaging. We have also demonstrated that the visibility statistics exhibit several remarkable characteristics. For example, the combination of scintillation and self-noise introduces a broad “skirt” in the distribution of visibility that dominates asymptotic statistics, regardless of the baseline or the signal-to-noise. Finally, we have given simplifications of this PDF in various regimes, such as the zero-baseline interferometer, as well as results for various projections of the PDF.

Our results facilitate scintillation studies of pulsars in statistically-delicate regimes and studies of pulsar emission regions using interferometry. In particular, our description of Nyquist-limited statistics can provide a sensitive and robust detection of an extended emission region, which does not require any assumptions about the nature or distribution of the scattering material and can be applied to estimate the emission sizes of individual pulses.

3.5 Appendix: Mathematical Results

3.5.1 Product of Correlated Complex Gaussian Random Variables

Let w_1 and w_2 be a pair of correlated circular complex Gaussian random variables with standard deviations σ_i and correlation $\rho \equiv \langle w_1 w_2^* \rangle / (\sigma_1 \sigma_2)$. Gwinn (2001) derived the PDF for the product (i.e. the “visibility”) $V \equiv w_1 w_2^*$ for $\rho \in \mathbb{R}$. We generalize his result in two directions: by allowing $\rho \in \mathbb{C}$ and by accounting for the averaging of N i.i.d. visibilities. The first extension is simply a complex rotation of the PDF for real ρ :

$$\begin{aligned} P(V; \sigma_1, \sigma_2, \rho) &= \frac{2}{\pi} \frac{1}{(1 - |\rho|^2) \sigma_1^2 \sigma_2^2} K_0 \left(\frac{2}{(1 - |\rho|^2) \sigma_1 \sigma_2} |V| \right) \exp \left(\frac{2}{(1 - |\rho|^2) \sigma_1 \sigma_2} \operatorname{Re}[V \rho^*] \right) \\ &\equiv \frac{1}{2\pi} \frac{(1 - |\rho|^2)}{a^2} K_0 \left(\frac{|V|}{a} \right) \exp \left(\frac{\operatorname{Re}[V \rho^*]}{a} \right). \end{aligned} \quad (3.39)$$

Here, we have introduced the scale parameter $a \equiv \frac{(1 - |\rho|^2)}{2} \sigma_1 \sigma_2$ for convenience.

The PDF is written with respect to the standard complex metric $d\operatorname{Re}[V] d\operatorname{Im}[V]$.

The characteristic function of this visibility PDF is then given by

$$\varphi(k_r, k_i; a, \rho) = \frac{1 - |\rho|^2}{1 + (ak_r - i\operatorname{Re}[\rho])^2 + (ak_i - i\operatorname{Im}[\rho])^2}, \quad (3.40)$$

where k_r and k_i are conjugate variables to $\operatorname{Re}[V]$ and $\operatorname{Im}[V]$, respectively.

We can calculate the PDF of the average of N i.i.d. visibilities by inverting the product of their characteristic functions:

$$P(V; a, \rho, N) = \frac{1}{2^N \pi (N-1)!} \left(\frac{N}{a}\right)^{N+1} (1 - |\rho|^2)^N |V|^{N-1} \quad (3.41)$$

$$\times K_{N-1} \left(N \frac{|V|}{a}\right) \exp\left(N \frac{\text{Re}[V\rho^*]}{a}\right).$$

If the averaged visibilities are not statistically isotropic, then we can still obtain a useful reduction using Feynman parameters to symmetrize the product of characteristic functions. These parameters $\{s_i\}$ are defined and applied as (Srednicki, 2007):

$$\frac{1}{A_1 \dots A_N} = \int dF_N (s_1 A_1 + \dots + s_N A_N)^{-N}, \quad (3.42)$$

$$\int dF_N = (N-1)! \int_0^1 ds_1 \dots ds_N \delta(s_1 + \dots + s_N - 1).$$

The result of Eq. 3.41 can then be applied to the symmetrized integrand.

Because the visibility is complex, the convolution of N visibilities requires a $2(N-1)$ -dimensional integral. However, to symmetrize the convolution requires a single Feynman parameter for each visibility. The Feynman parameters also have an overall δ -function constraint, so the convolution is reduced to an $(N-1)$ -dimensional integral. If some pairs of visibilities are i.i.d., then the dimensionality of the integral can be further reduced. Gwinn et al. (2012b) applied this reduction, in conjunction with the Gaussian approximation (§3.2.3.2), to evaluate the effects

of an extended emission region on the PDF of visibility; they thereby reduced the dimensionality of the necessary numerical integration from four dimensions to one.

3.5.2 Visibility Projections

We now calculate the real and imaginary projections of the visibility PDF (Eq. 3.41). We again utilize the characteristic function: the conjugate projected variable is set to zero, and the remaining function is inverted with respect to the unprojected variable. If the averaged visibilities are i.i.d., we obtain

$$P(V_r; a, \rho, N) = \frac{N}{(N-1)!} \frac{\sqrt{1-\rho_i^2}}{a} \left[\frac{N}{2} \left(\frac{1-|\rho|^2}{\sqrt{1-\rho_i^2}} \right) \frac{|V_r|}{a} \right]^N \quad (3.43)$$

$$\times k_{N-1} \left(N \sqrt{1-\rho_i^2} \frac{|V_r|}{a} \right) e^{N\rho_r \frac{V_r}{a}}.$$

Here, $\rho_r \equiv \text{Re}(\rho)$, $\rho_i \equiv \text{Im}(\rho)$, $V_r \equiv \text{Re}(V)$, and $k_N(x)$ is the modified spherical Bessel function of the second kind (Arfken & Weber, 2005). The imaginary projection $P(V_i; a, \rho, N)$ follows from the substitutions $\rho_r \leftrightarrow \rho_i$ and $V_r \rightarrow V_i$. Setting $N = 1$ and $\rho \in \mathbb{R}$ recovers the results given in the appendix of Gwinn (2001).

We also present the projected imaginary variance: $Q(V_r) \equiv \int V_i^2 P(V_r, V_i) dV_i$. For this calculation, we again use the characteristic function, but take two derivatives with respect to k_i and multiply the result by -1 before zeroing k_i and

inverting with respect to k_r :

$$\begin{aligned}
 Q(V_r; a, \rho, N) &= \frac{2}{N!} \frac{a}{(1 - |\rho|^2)} \left[\frac{N(1 - |\rho|^2)}{2} \frac{|V_r|}{\sqrt{1 - \rho_i^2}} \frac{1}{a} \right]^{N+1} \\
 &\times \left[N \rho_i^2 \frac{|V_r|}{a} k_{N+1} \left(N \sqrt{1 - \rho_i^2} \frac{|V_r|}{a} \right) + \sqrt{1 - \rho_i^2} k_N \left(N \sqrt{1 - \rho_i^2} \frac{|V_r|}{a} \right) \right] e^{N \rho_r \frac{V_r}{a}}.
 \end{aligned} \tag{3.44}$$

Additional projections can be performed similarly.

Chapter 4

Constraining the Vela Pulsar's Radio Emission Region

In this chapter, we will apply the statistical techniques developed in Chapter 2 to analyze observations of the Vela pulsar at 760 MHz.¹ This analysis particularly benefits from the high-quality data enabled by the Green Bank Ultimate Pulsar Processing Instrument (GUPPI) at the Green Bank Telescope, which can record raw baseband voltages over a 200 MHz bandwidth. In addition to this capability, GUPPI ultimately digitizes the signal with eight bits (two is typical), which minimizes quantization artifacts (see Chapter 6).

We will demonstrate that our simplest derived model, which requires no fitted parameters and no assumptions about the nature or distribution of the scattering material, is consistent with the data to the fundamental limit of $\sim 0.01\%$ determined by the Poisson noise of the Nyquist-limited spectral samples. This agreement enables constraints on the characteristic size of the emission region of

¹This chapter is adapted from Johnson et al. (2012).

only a few kilometers at the pulsar – an angular size of 100 picoarcseconds.² We will also derive constraints on the emission regions of individual pulses.

Moreover, these measurements can shed light on the emission altitude, since relativistic beaming of the radio emission implies that the spatial displacement of an emission site depends on the field-line curvature. We will establish the relationship between the characteristic transverse size and the emission altitude for an arbitrary pulsar orientation, and will relate our emission altitude inferences to those of complementary methods.

4.1 Introduction

4.1.1 Pulsar Emission and Scintillation

Owing to their extraordinary emission, pulsars are invaluable probes of a vast array of extreme physics, from the supranuclear density interiors and the $\sim 10^{12}$ G magnetospheres of neutron stars, to the turbulent plasma of the interstellar medium (ISM). The regularity of their time-averaged emission has been applied to sensitive tests of general relativity (Taylor & Weisberg, 1989; Kramer et al., 2006), and the achieved timing precision holds promise for direct observation of gravitational waves (Detweiler, 1979; Jenet et al., 2006; Hobbs et al., 2010). Yet, remarkably, no consensus exists for the precise origin of this emission; its geometry, stabil-

²For comparison, the diameter of the polar cap for the Vela pulsar is approximately 1 km, while the light-cylinder diameter is $\sim 10^4$ km. However, the apparent characteristic size is strongly affected by relativistic beaming, so the interpretation requires some delicacy; see §4.6.

ity, and physical mechanism remain enigmatic, even after nearly a half-century of study (Melrose, 2004; Verbiest et al., 2009). The incredible compactness of the pulsar and its surrounding plasma prohibit traditional imaging of the emission process, but a number of methods can achieve the requisite resolution, using the interstellar plasma as an effective “lens” (Lovelace, 1970; Backer, 1975; Cordes et al., 1983; Cornwell & Narayan, 1993; Gwinn et al., 1998; Shishov, 2010).

Variations of this stochastic lens give rise to the observed scintillation, and statistics of these variations convey information about the spatial structure of the emission. Longer observing wavelengths enhance the signature of this structure because the stronger scattering effectively enlarges the aperture. However, the increased spatial resolution comes at the expense of spectral resolution, and it becomes difficult to decouple the scintillation from source noise and variability. Indeed, the pulse-broadening timescale can easily exceed that of intrinsic pulsar variation.

We can circumvent these difficulties by constructing spectra over accumulation times that include *all* pulsed power. Intrinsic sub-pulse variability then affects the correlation of spectral noise but not the mean spectrum or single-channel statistics (Gwinn & Johnson, 2011). Furthermore, we can distinguish the effects of extended source geometry from the scattering evolution and pulsar variability by varying the degree of temporal averaging; with no averaging, only the source emission structure contributes. Additionally, we can identify the emission sizes of individual

pulses. We have presented a detailed mathematical treatment separately (Johnson & Gwinn, 2012; hereafter JG12).

We constructed spectra in this way and then compared histograms formed from the spectral samples with appropriate models for a strongly scintillating source. Such models benefit from minimal assumptions about the nature and distribution of both the scattering material and the underlying emission; this generality is achieved at the expense of resolution in pulse phase. The inferred emission size is therefore a characteristic size of the emission region, quantified via a dimensionless parameter γ_s , which depends on the spatial standard deviation of source intensity, weighted by integrated flux density. Translating γ_s to physical units at the pulsar additionally requires specification of the scattering geometry.

4.1.2 Comparison with Previous Work

Several previous investigations have also quantified scintillation statistics in order to estimate the size of the Vela pulsar’s emission region. In general, for a strongly scattered point source, the scintillation acts upon intensity as a multiplicative gain \mathcal{G} that is the squared modulus of a complex random walk. The probability density function (PDF) of \mathcal{G} is therefore exponential, $P(\mathcal{G}) = e^{-\mathcal{G}}$, with an associated modulation index of unity: $m^2 \equiv \langle \mathcal{G}^2 \rangle / \langle \mathcal{G} \rangle^2 - 1 = 1$. A spatially-extended emission region smoothes this variation, and so the modified $P(\mathcal{G})$ or reduced

modulation index can be used to estimate the emission size (Salpeter, 1967; Cohen et al., 1967; Gwinn et al., 1998).

The principal difficulty in detecting these modifications is the additional noise that arises from the noiselike nature of the source, known as *self-noise*, and from the background. Pulsars are particularly challenging targets because their dramatic intrapulse and interpulse variations also contribute modulation. All of these sources of noise can easily imitate or mask the signature of an extended emission region. Previous efforts have attempted to minimize these sources of noise by spectral averaging in both frequency and time. In contrast, the present technique fully accounts for the effects of self-noise and intrinsic pulsar variability.

For example, Gwinn et al. (1997) sought to detect the modification of $P(\mathcal{G})$ through the PDF of the correlation function amplitude on the Tidbinbilla-Parkes baseline at 2.3 GHz. Because this baseline was much shorter than the scale of the diffraction pattern, the observational setup was effectively a zero-baseline interferometer. Their best-fitting model corresponded to an emission region with a FWHM of 460 ± 110 km. Gwinn et al. (2000) then extended this analysis to three gates across the pulse, also at 2.3 GHz. They improved the model PDF and quantified the effects of their averaging in frequency and time. They estimated a declining size of the emission region from 440 ± 90 km to less than 200 km across the pulse.

Rather than analyzing distribution functions, Macquart et al. (2000) used the modulation index to quantify the effects of emission size for single-dish data. They measured $m^2 \approx 0.9$ at 660 MHz and thereby inferred the extent of source emission to be no more than 50 km (FWHM = 120 km). Including the contribution of self-noise leads to an inferred FWHM of the emission region of ~ 200 km (see §2.5.1).

More recently, Gwinn et al. (2012b) analyzed visibilities on the Tidbinbilla-Mopra baseline at 1.65 GHz and fit models to the projections of the real part and imaginary variance. They found the size of the emission region to be large both early and late in the pulse (~ 400 km and ~ 800 km, respectively) but near zero in the central portion, where the pulse is strong.

An analysis at lower frequencies has the advantage of increasing the signature of size but the disadvantage of incurring more mixing between the scintillation and the pulsar noise. We demonstrate that this difficulty is not prohibitive, and that a careful statistical description of observed power spectra at low frequencies can yield fresh insight into the physics of both interstellar scattering and pulsar emission.

4.1.3 Outline of Chapter

In §4.2, we briefly review the theoretical descriptions of pulsar emission and interstellar scintillation. Then, in §4.3, we describe our observations and the subsequent construction of both the observed and model PDFs of intensity; we also

present the expected residual structure arising from an extended emission region and outline the model fitting procedure. Next, in §4.4, we give our analysis for various pulse selection cuts and derive our estimates for the size of the emission region. In §4.5, we quantify possible biases and systematic errors in our inferences of the size of the emission region. Then, in §4.6, we interpret our measurements in terms of beamed, dipolar emission, and derive the corresponding emission altitudes. Finally, in §4.7, we summarize our results, their impact on our understanding of pulsar magnetospheres, and the prospects for future work.

4.2 Theoretical Background

4.2.1 Pulsar Radio Emission

A full understanding of pulsar emission is elusive, but proposed scenarios typically invoke a relativistic electron-positron plasma that flows outward from the pulsar polar caps to the light cylinder (Goldreich & Julian, 1969). This outflow then generates radio emission via coherent curvature radiation (Sturrock, 1971; Ruderman & Sutherland, 1975; Mitra et al., 2009). The emission is beamed, ducted, and refracted as it propagates through the upper magnetosphere (Barnard & Arons, 1986; Arons & Barnard, 1986; Lyutikov & Parikh, 2000).

The precise altitude at which the emission is generated is uncertain, and various analyses suggest emission heights from a few stellar radii (Arons & Scharlemann, 1979) to hundreds of stellar radii (Karastergiou & Johnston, 2007) for

Vela-like pulsars. In the classification and interpretation of Rankin (1990), the Vela pulsar is a core-single (\mathbf{S}_t) pulsar, with emission arising effectively at the stellar surface.

4.2.2 Interstellar Scattering

4.2.2.1 Scintillation Physics

Density inhomogeneities in the dilute, turbulent plasma of the ISM scatter the radio emission, leading to multipath propagation. At 760 MHz, the Vela pulsar is deep within the regime of ‘strong’ scattering, for which the Fresnel scale is much larger than the diffractive scale. Furthermore, the timescale for evolution of the diffraction pattern at the observer is several seconds, so each scintillation element is effectively static for the duration of a single pulse (~ 5 ms). The scattering then acts to convolve the pulsar signal with a stochastic propagation kernel, which reflects the scintillation and temporal broadening (Hankins, 1971; Williamson, 1972; Gwinn & Johnson, 2011).

The spatial extent of the emission region influences the scintillation. A pair of dimensionless parameters, $\{\gamma_{s,1}, \gamma_{s,2}\}$, quantify the emission region and give its squared characteristic size in an orthogonal, transverse basis $\{\hat{\mathbf{x}}_1, \hat{\mathbf{x}}_2\}$, in units of

the magnified diffractive scale (Gwinn et al., 1998):

$$\gamma_{s,i} = \left(\frac{D}{R} \frac{\sigma_i}{\frac{1}{2\pi} \frac{\lambda}{\theta_i}} \right)^2. \quad (4.1)$$

Here, D is the characteristic observer-scatterer distance, R is the characteristic source-scatterer distance, λ is the observing wavelength, θ_i is the angular size of the scattering disk along \hat{x}_i , and σ_i is the standard deviation of the distribution of source intensity along \hat{x}_i . This representation accommodates anisotropy of both the source emission and the distribution of scattering material.

Nevertheless, the effects of anisotropy in the emission and scattering only manifest at quadratic order in γ_s ; thus, we use $\gamma_s \equiv (\gamma_{s,1} + \gamma_{s,2})/2$ to avoid parameter degeneracy. Likewise, we state our results in terms of the standard deviation $\sigma_c \equiv \sigma_1 = \sigma_2$ of a circular Gaussian intensity profile. The FWHM of such a profile is $2\sqrt{\ln 4}\sigma_c \approx 2.35\sigma_c$.

4.2.2.2 Interpretation of the Inferred Emission Size

The emission size that we infer from γ_s reflects the full extent of the emission region. Explicitly, we observe the spatial standard deviation of the emitting region, weighted by integrated flux density (see Chapter 2). Thus, even if the instantaneous emission is pointlike, if the received radiation arises from spatially offset emission sites then $\gamma_s > 0$. We derive the effective emission size of beamed, dipolar emission in §4.6.

4.2.2.3 Scattering Geometry of the Vela Pulsar

The conversion of γ_s to a physical size at the pulsar requires measurements of the location, scale, and nature of the scattering. Using VLBI parallax, Dodson et al. (2003) estimated a distance of 287^{+19}_{-17} pc to the Vela pulsar. Combined with the angular and temporal broadening of the pulsar, this distance identifies the characteristic location of the scattering material (Gwinn et al., 1993b). Gwinn et al. (1997) measured the angular broadening to be $(3.3 \pm 0.2 \text{ mas}) \times (2.0 \pm 0.1 \text{ mas})$ (FWHM) at 2.8 GHz. Combined with the temporal broadening, as calculated via the decorrelation bandwidth $\Delta\nu_d = 66 \text{ kHz}$ at 2.3 GHz, these measurements suggest a characteristic fractional distance of $\frac{D}{D+R} \approx 0.72$ to the scattering material and an effective magnification of $D/R \approx 2.9$ (Gwinn et al., 2000). Thus, if the source emits a circular Gaussian intensity profile, then $\sigma_c \approx \left(\frac{\nu_{\text{MHz}}}{800 \text{ MHz}}\right) \times 440\sqrt{\gamma_s} \text{ km}$.

Different models of the scattering medium or emission geometry will update this conversion but will not affect our model PDFs or measurements of γ_s . For example, we quantify the effect of the phase structure function of the scattering material in §4.5.3.

4.3 Observation and Data Reduction

4.3.1 Observation and Baseband Recording

We observed the Vela pulsar for one hour on 22 October 2010 and one hour on 25 October 2010 using the Robert C. Byrd Green Bank Telescope (GBT) and the recently built Green Bank Ultimate Pulsar Processing Instrument (GUPPI). For flux calibration, we also observed 3C 190 (0758+143) for approximately 20 minutes prior to each pulsar observation.

We used GUPPI in 8-bit, 200 MHz mode, and our observation spanned 723.125-923.125 MHz. Rather than utilizing the standard real-time dedispersion of GUPPI, we recorded the channelized complex baseband voltages directly to disk for offline processing. The collected data constitute approximately 8 TB.

4.3.2 Coherent Dedispersion and Formation of Spectra

We processed the baseband data using the digital signal processing software library DSPSR (van Straten & Bailes, 2011), which first performed coherent dedispersion and then formed dynamic spectra via a *phase-locked filterbank*. This technique constructs each spectrum from a fixed-length time-series beginning at the corresponding pulse phase, rather than windowing the pulse into a fixed number of temporal phase bins. Our spectra had 262,144 channels per 25 MHz, corre-

sponding to 95.4 Hz resolution. The ~ 10.5 ms spectral accumulation time easily contained all of the power in one pulse.

We exported the coherently-dedispersed spectra from DSPSR into PSRFITS format and then performed flux calibration for each polarization using the software suite PSRCHIVE (Hotan et al., 2004). Subsequent processing utilized the PSRCHIVE libraries, which we integrated into our custom software.

Although reversing the Faraday rotation is straightforward, we chose to analyze the measured linear polarization streams without modification in order to avoid introducing possible artifacts from calibration errors and mixing. Consistency of our results between the two polarizations is, therefore, a meaningful and encouraging indication that our inferences reflect properties of the pulsar rather than instrumental limitations.

4.3.3 Data Excision and Bandpass Correction

4.3.3.1 RFI Excision

We iteratively excised RFI using a median smoothed difference criterion, similar to that implemented in PSRCHIVE. Specifically, we compared the estimated background noise in each frequency channel with the noise in its surrounding 250 kHz sub-band; we rejected channels that differed from the sub-band median by more than three times the sub-band standard deviation. Such rejections typically constituted a tiny fraction of the data ($\sim 0.3\%$, as expected from the 3σ cut). Also, to

reject impulsive RFI, we dropped all pulses for which the off-pulse mean differed from a three-minute moving average of the off-pulse region by more than 5%.

4.3.3.2 Background Noise and Bandpass Shape Estimation

GUPPI divided the observed 200 MHz frequency band into 32 filterbank sub-bands, each of 6.25 MHz. Because of spectral roll-off, we only analyzed the central 3.2 MHz of each filterbank sub-band; each such segment was analyzed independently.

We estimated both the background noise level and the bandpass shape by analyzing the off-pulse spectra. The off-pulse region excluded the 10.5 ms on-pulse spectra, as well as a frequency-dependent phase range of width 0.15 that contained negatively-dedispersed power leaked from the interleaved sampling.

Next, we normalized the bandpass. We determined the bandpass shape for each three-minute block using a $(3 \text{ minute}) \times (100 \text{ kHz})$ moving average of the off-pulse data, or $\sim 2 \times 10^6$ samples for each spectral channel. The bandpass variations across each 3.2 MHz sub-band were typically a few percent; thus, they contributed minimally to the observed statistics because of their small variance.

4.3.3.3 Rejection of Pulses with Quantization Saturation

Because the Vela pulsar is both bright and variable, particularly when coupled with scintillation, some of the strongest pulses saturated our quantization thresholds. Moreover, because the quantization levels were fixed across the band, the strong linear polarization of the pulsar (combined with Faraday rotation) and the

receiver bandpass shape caused the prevalence of saturation to vary substantially across the 200 MHz observing bandwidth.

Accordingly, we implemented a five-level ‘guard zone’ at the positive and negative thresholds (of 256 total levels); we excluded any pulse that included a quantized value $|x| > 122$. This criterion rejected $\gtrsim 75\%$ of pulses for the stronger linear polarization near 850 MHz, but rejected $\lesssim 1\%$ of pulses, regardless of polarization, at frequencies $\lesssim 775$ MHz. To avoid a selection bias against strong pulses, we preferentially draw later examples from the lower-frequency sub-bands.

4.3.4 Observed PDF of Intensity

4.3.4.1 Histogram Formation

We constructed a histogram of measured intensities for every (1 hour) \times (3.2 MHz) block of on-pulse data ($\sim 10^9$ spectral samples). Histogram bins had uniform widths of 0.05, in units where the mean background intensity was unity because of the bandpass normalization. We then normalized each histogram by the total number of samples and the bin width; we will refer to this normalized histogram as the ‘observed PDF’ of intensity.

4.3.4.2 Effects of Finite Histogram Resolution

In order to compare a theoretical PDF $P(I)$ with an observed PDF, we must account for the finite bin width of the histogram. Specifically, the theoretical

(normalized) histogram value $H(I; \Delta I)$ for a bin of width ΔI centered on I is given by

$$H(I; \Delta I) = \frac{1}{\Delta I} \int_{I-\Delta I/2}^{I+\Delta I/2} P(I') dI'. \quad (4.2)$$

Expanding $P(I')$ about I and replacing the second derivative with its discrete representation gives

$$H(I; \Delta I) \approx P(I) + \frac{P(I + \Delta I) - 2P(I) + P(I - \Delta I)}{24}. \quad (4.3)$$

This approximation corrects for the finite bin width to quadratic order in ΔI , while only requiring calculation of the theoretical PDF at the histogram bin centers. For our data, the next order correction, $\Delta I^4 P^{(4)}(I)/1920$, was well below our Poisson noise. The effects of the finite bin width were small when $N = 1$ (typically $\lesssim 0.005\%$ of the PDF amplitude), but they became appreciable for larger N .

4.3.5 Model PDF of Intensity

We independently constructed observed PDFs for each scalar electric field (i.e. each linear polarization) and with various degrees of temporal averaging N , bandwidth, and pulse selection cuts. In all of these cases, the mean source and background intensities of the pulses parametrized the point-source model PDF of intensity; this parametrization accounted for the intrinsic pulse-to-pulse variability

as well as the quasistatic evolution of receiver gain and noise levels. Because this treatment incorporated the observed set of pulse amplitudes rather than appealing to assumptions about their distribution, our models were robust to arbitrary pulse-to-pulse variations, including strongly correlated behavior such as nulling or heavy-tailed distributions of pulse amplitude, as are observed for some pulsars (Lundgren et al., 1995; Cairns et al., 2001).

4.3.5.1 Model PDF Parameter Estimation

We estimated the single-pulse source and background amplitudes using the mean of all the on-pulse or off-pulse channels in the analyzed sub-band that had not been flagged for RFI. For a 3.2 MHz sub-band, this estimate included $\sim 30,000$ samples for the on-pulse region and $\sim 200,000$ samples for the off-pulse region of each pulse. This average effectively isolated the intrinsic pulsed power from scintillation because each averaged sub-band contained many independent scintillation elements ($\Delta\nu_d \sim 1$ kHz). However, these estimates were subject to both bias and noise, and we determine the effects of such errors in §4.5.

4.3.5.2 Construction of the Model PDF

We now describe the basis and formation of our model PDFs of intensity. First, consider N consecutive pulses with gated source intensities $A_1 I_s, \dots, A_N I_s$ and mean background intensity I_n . After averaging the N spectra formed from these

pulses, the PDF of intensity is given by (see Eq. 2.3):

$$P(I; N) = N \int_0^\infty dG \frac{e^{-G}}{(I_s G)^{N-1}} \sum_{j=1}^N \frac{(A_j I_s G + I_n)^{N-2}}{\prod_{\substack{\ell=1 \\ \ell \neq j}}^N (A_j - A_\ell)} e^{-\frac{NI}{(A_j I_s G + I_n)}}. \quad (4.4)$$

The integral over G arises because we assume that each spectrum effectively explores the full scintillation ensemble.

We calculated this theoretical PDF for every sequence of N pulses that contributed to an observed PDF, using the estimated model parameters $\{A_j I_s, I_n\}$. We then averaged these distributions to yield the ‘model PDF’ of intensity. Note that the model PDF required no fitted parameters and was independently constructed for each observed PDF.

4.3.6 Expected Residual Structure

The PDF residual $\mathcal{R}(I)$ (i.e. the observed minus model PDF) contains signatures of extended emission size, decorrelation of the scintillation within the averaging time, and errors in the model parameters $\{A_j I_s, I_n\}$. These perturbations have nearly identical shape, so a single fitted parameter quantifies their combined effect. We can break this degeneracy by varying the reduction parameters such as N and the analyzed bandwidth. For example, the temporal decorrelation of the scintillation pattern does not contribute when $N = 1$.

We approximate the expected cumulative residual arising from the emission size and the temporal decorrelation as (Eq. 2.9, 2.10, 2.18)

$$\mathcal{R}(I) \approx - \left[2\gamma_s + \frac{\sum_{i<j} (1 - \Gamma_{ij})}{N(N+1)} \right] \int_0^\infty dG G e^{-G} \frac{\partial^2 P(I; N|G)}{\partial G^2}. \quad (4.5)$$

This general form expresses the influence of the temporal autocorrelation function of the scintillation pattern:

$$\Gamma_{ij} \equiv \frac{\langle [I(t_i, f) - I_n(t_i, f)] [I(t_j, f) - I_n(t_j, f)] \rangle}{\langle I(t, f) - I_n(t, f) \rangle^2} - 1. \quad (4.6)$$

We will quantify alternative sources of residual structure, such as parameter errors, in terms of their incurred bias on γ_s . As was required for the model PDF, this model residual was calculated for every sequence of N pulses that contributed to the corresponding observed PDF and subsequently averaged.

If the N averaged intensities are drawn from consecutive pulses, then the scale \mathcal{R}_0 of the residual structure can be approximated as

$$\mathcal{R}_0 \equiv \gamma_s + \frac{\sum_{i<j} (1 - \Gamma_{ij})}{2N(N+1)} \approx \gamma_s + \frac{1}{24} \frac{N(N-1)}{\Delta\tau_d^2}, \quad (4.7)$$

where $\Delta\tau_d \gg N$ is the decorrelation timescale in pulse periods, and we have assumed the standard square-law autocorrelation $\Gamma_{ij} = e^{-|(i-j)/\Delta\tau_d|^2}$. Thus, the rela-

tive influence of temporal decorrelation to emission size is approximately quadratic in N .

4.3.7 Fitting the Residual Structure

For each observed PDF, we calculated the corresponding model PDF and residual shape. We then performed a weighted least-squares fit to the measured residual after correcting for the finite histogram resolution; we assigned weights by assuming that the histogram errors reflected Poisson noise. The only fitted parameter was the amplitude scale \mathcal{R}_0 of the residual. In some cases, we performed multiple reductions on the same set of pulses by varying the averaging (N) or the lag between the averaged pulses ($\Delta\tau$); we then fit all these reductions simultaneously to the pair of parameters $\{\gamma_s, \Delta t_d\}$ by assuming a square-law autocorrelation structure.

4.4 Analysis

We now describe our analysis and subsequent inference, in successively tighter pulse cuts. We began by analyzing statistics of each polarization, when pulses were all analyzed concurrently (§4.4.1). Then, we analyzed PDFs formed by averaging pairs of intensities with varying temporal lag, to demonstrate that our description of the effects of temporal decorrelation is correct (§4.4.2). Next, we segregated pulses into quantiles by pulse strength to investigate the possible co-

variance between the size of the emission region and pulse shape (§4.4.3). Finally, we examined the statistics of each individual pulse (§4.4.4).

We did not detect the effects of a finite emission region in any of these cases, regardless of frequency or polarization. Thus, our chosen examples are merely those that yield the tightest constraints on γ_s . For this purpose, we favor one filterbank sub-band centered on 757.5 MHz, for which the polarization position angle of the pulsar was nearly aligned with that of the receiver, the pulsar rarely saturated the quantization thresholds, the leaked power from the interleaved sampling was far off-pulse, and there was no evidence for substantial RFI contamination. To achieve our tightest limit on the size of the emission region, we jointly analyze this sub-band with the adjacent sub-bands. The full frequency evolution of our observations is a powerful probe of the scattering, on the other hand, as we analyze separately (Johnson et al., 2013b).

4.4.1 All Pulses

To utilize the full statistical content of our observations, we first analyzed all pulses concurrently, in groups only determined by frequency and polarization. We constructed each observed PDF from a (1 hour) \times (3.2 MHz) on-pulse block of data: $\sim 10^9$ spectral samples and $\sim 40,000$ pulses. The scintillation pattern evolved substantially over both the span of time and frequency; each observed PDF contained samples from $\sim 10^6$ independent scintillation elements.

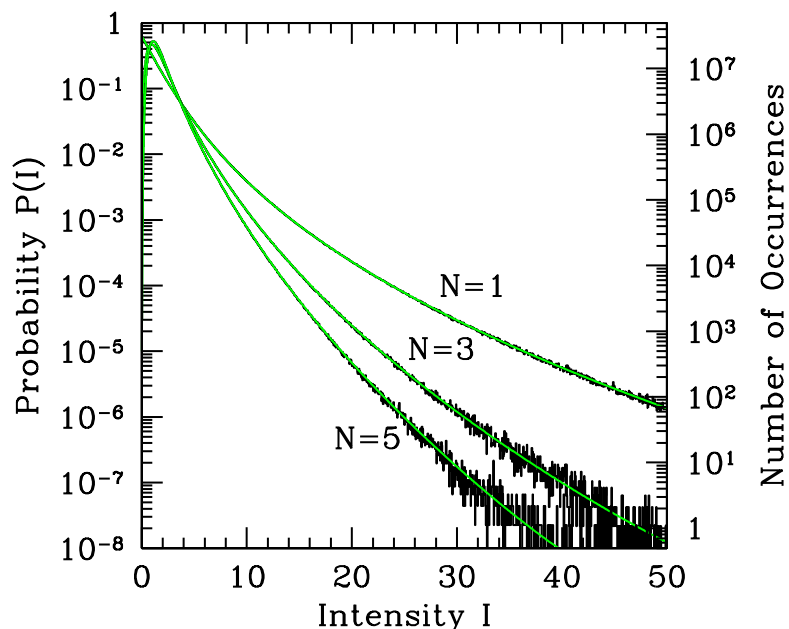


Figure 4.1: Observed and model PDFs of intensity for three degrees of averaging: $N = 1, 3,$ and 5 . There are no fitted parameters. The mean intensities of the source and background are $I_s \langle A \rangle = 0.87$ and $\langle I_n \rangle = 1.00$, respectively; the plot therefore extends to ~ 27 times the mean signal.

Figure 4.1 demonstrates one example of the comparison of our model and observed PDFs of intensity; the plotted data correspond to the stronger linear polarization for the 3.2 MHz sub-band centered on 757.5 MHz. The agreement extends over the nearly eight decades spanned. The tail of the distribution arises from the combined effects of intrinsic variability, noise, and scintillation; the success of the model indicates that it correctly accounts for each effect.

Our models also correctly characterize the effects of temporal averaging, N . The decorrelation timescale in pulse periods is $\Delta\tau_d \sim 50$, so the correction for temporal decorrelation is quite small for the plotted reductions: $N=1, 3,$ and 5 (see Eq. 4.7).

For $N = 1$, the residual structure in the stronger polarization has an amplitude of $\lesssim 10^{-4}$, which is comparable to the Poisson noise in the histogram. A weighted linear least-squares fit to the lowest 200 samples ($I < 10$) in the observed PDF estimates $\gamma_s = (2.0 \pm 1.0) \times 10^{-4}$ with reduced chi-squared $\chi_{\text{red}}^2 = 1.13$; the standard deviation of χ_{red}^2 is $\sqrt{2/200} = 0.1$. Furthermore, because intrinsic modulation correlates noise in adjacent spectral channels, Poisson weights underestimate the histogram errors, so $\chi^2 \gtrsim 1$ is expected. Thus, a conservative upper-bound on the effects of size from this single sub-band is $\gamma_s \lesssim 5 \times 10^{-4}$, which is equivalent to $\sigma_c \approx 8$ km at the pulsar with the conversion of §4.2.2.3.

For the adjacent sub-bands (centered on 751.25 MHz and 763.75 MHz), the fits give $\gamma_s = (-2.2 \pm 1.1) \times 10^{-4}$ and $\gamma_s = (-1.2 \pm 1.0) \times 10^{-4}$. Combining these results refines the 3σ size upper-bound to approximately 4 km at the pulsar. Narrower sub-bands give similar results, with larger errors because of the increased Poisson noise and a larger bias from the finite bandwidth (see §4.5.1). In all cases, our results suggest a characteristic size of $\lesssim 10$ km for the emission region.

4.4.2 $N = 2$ with Temporal Lag $\Delta\tau$

We next examined effects dominated by temporal decorrelation of the scintillation pattern. We constructed PDFs with $N = 2$ that averaged pairs of pulses separated by $\Delta\tau$ pulse periods; the amplitude of the residual structure (Eq. 4.5) then depends roughly quadratically on $\Delta\tau$. We approximated the autocorrelation

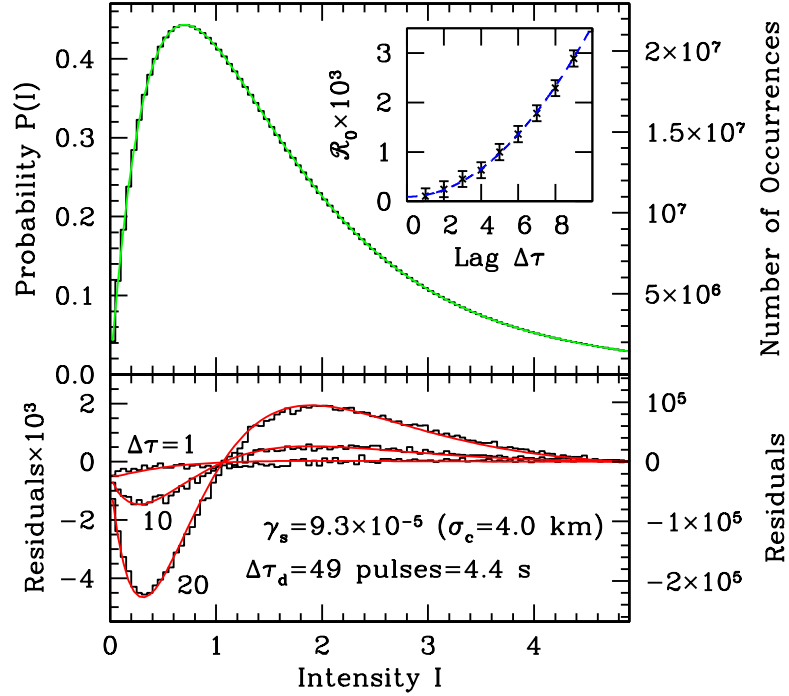


Figure 4.2: Observed and model PDFs of intensity with their corresponding residual structure; $N = 2$. Three cases are plotted, corresponding to averaged pairs of intensities that are separated by $\Delta\tau = 1, 10,$ and 20 pulses. The residuals are concurrently fit to the decorrelation timescale Δt_d and dimensionless size γ_s . The inset shows the fitted residual scale \mathcal{R}_0 with 3σ errorbars as a function of $\Delta\tau$, along with the best-fitting prediction (see Eqs. 4.5 and 4.7).

function as Gaussian, $\Gamma(\Delta\tau) = e^{-(\Delta\tau/\Delta\tau_d)^2}$, to simultaneously fit all lags to the pair of parameters, $\{\gamma_s, \Delta\tau_d\}$.

The residuals match their expectations quite well; Figure 4.2 shows one example, again from the stronger linear polarization for the 3.2 MHz sub-band centered on 757.5 MHz. This excellent agreement demonstrates the quality of our analytical representation of decorrelation of the scintillation pattern within the averaging time. The fits estimate $\gamma_s = (9.3 \pm 5.4) \times 10^{-5}$ giving a 3σ upper-bound on the size of the emission region as ~ 7 km.

4.4.3 Quantiles

Individual pulse profiles for the Vela pulsar show marked dependence on their strength (Krishnamohan & Downs, 1983). To examine covariance between pulse strength and emission size, we segregated the pulses into quantiles by their mean flux density and then analyzed each subset independently.

This approach has several utilities. Because the resolving power improves with the SNR, a subset of strong pulses can maximize the potential resolution. Furthermore, many instrumental biases vary differently with pulse strength than their effects on the inferred size do (see §4.5.2); the variation of γ_s between quantile subsets can therefore suggest the presence of such a bias.

We established deciles by pulse strength. Figure 4.3 shows the PDFs and their residual structure for the top and bottom decile; the mean gated signal-to-noise $\langle A_j I_s / I_n \rangle$ in these deciles is 1.39 and 0.48, respectively. The two residuals are comparable, and both suggest an emission size that is substantially smaller than the magnified diffractive scale. The limit is most stringent for the pulses in the top decile because of their higher SNR: $\gamma_s = (1.1 \pm 1.8) \times 10^{-4}$, or an 11 km upper-bound on the characteristic emission size at a 3σ confidence level. For the bottom decile, we obtain $\gamma_s = (-7.9 \pm 5.5) \times 10^{-4}$, which gives a 12 km upper-bound at the same confidence.

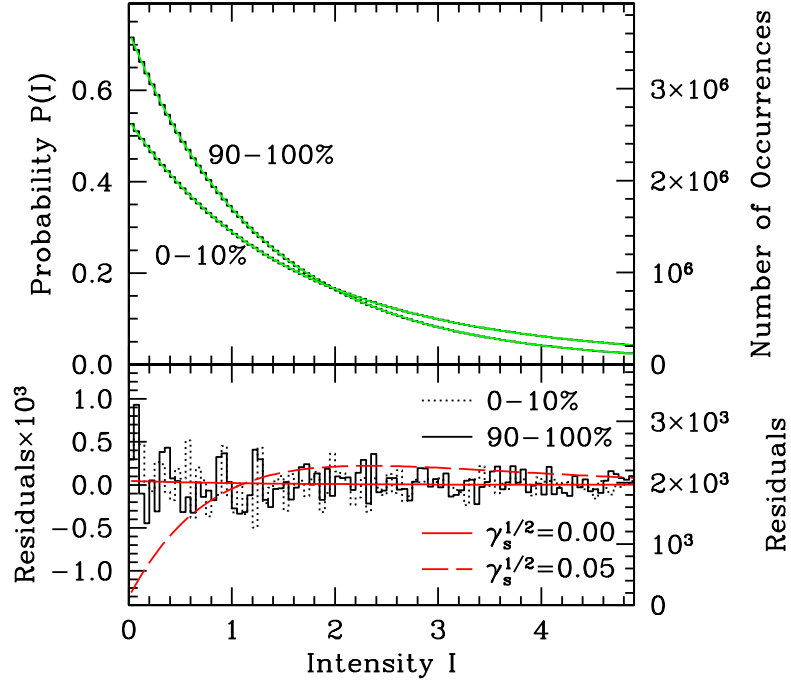


Figure 4.3: Observed and model PDFs of intensity for the subsets of pulses in the top and bottom decile by pulse intensity. Theoretical residual curves are plotted for a point source (the slight variation is from finite histogram resolution) and for a source that extends over 5% of the magnified diffractive scale (i.e. $\sigma_c \approx 20$ km); the latter is clearly inconsistent with the observed statistics.

4.4.4 Single-Pulse Statistics

Lastly, we examined the statistics for individual pulses. For each pulse, our model requires only two parameters to describe the spectral statistics: the mean intensities of the background (I_n) and gated signal (AI_s). Poisson noise generally limits each estimate of emission size to a sizeable fraction of the magnified diffractive scale; the standard error $\delta\gamma_s$ in the fitted γ_s is well-approximated by (see Eq. 2.26)

$$\delta\gamma_s \approx \frac{1.3}{\sqrt{N_{\text{tot}}S}} \exp [0.4 + 0.18 (\ln S)^2 + 0.01 (\ln S)^3]. \quad (4.8)$$

Here, N_{tot} is the total number of points used to estimate the observed PDF, and $S \equiv A_j I_s / I_n$ is the gated signal-to-noise ratio. Thus, for a strong pulse ($S \sim 2$), γ_s can be determined to within ± 0.006 ; whereas, for a weak pulse ($S = 0.1$), γ_s can only be established to within ± 0.2 . Interestingly, for observations of highly variable pulsars, the resolution afforded by strong single pulses may exceed that of the entire pulse ensemble analyzed jointly.

Figure 4.4 shows the fitted sizes for $\sim 30,000$ individual pulses as a function of their gated signal-to-noise; values from both linear polarizations are plotted. This sample of pulses included several ‘micro-giant’ pulses, as well as tens of pulses with the late ‘bump’ component identified by Johnston et al. (2001). We measured no confident detection of emission size effects; the inferred values of γ_s are consistent with the expected standard errors for observations of a source with point-like emission, as given by Eq. 4.8.

4.5 Sources of Bias in the Estimated Emission Size

Many practical limitations can bias the inferred emission size (see §2.4.4). For instance, the model parameters A_j and I_n are random variates estimated via finite averages of on-pulse and off-pulse spectra; they are therefore subject to noise, which is unbiased, and instrumental limitations such as quantization, which can introduce bias. Both of these types of errors can mimic the effects of an extended emission region. Here, we estimate the bias to γ_s resulting from each of these

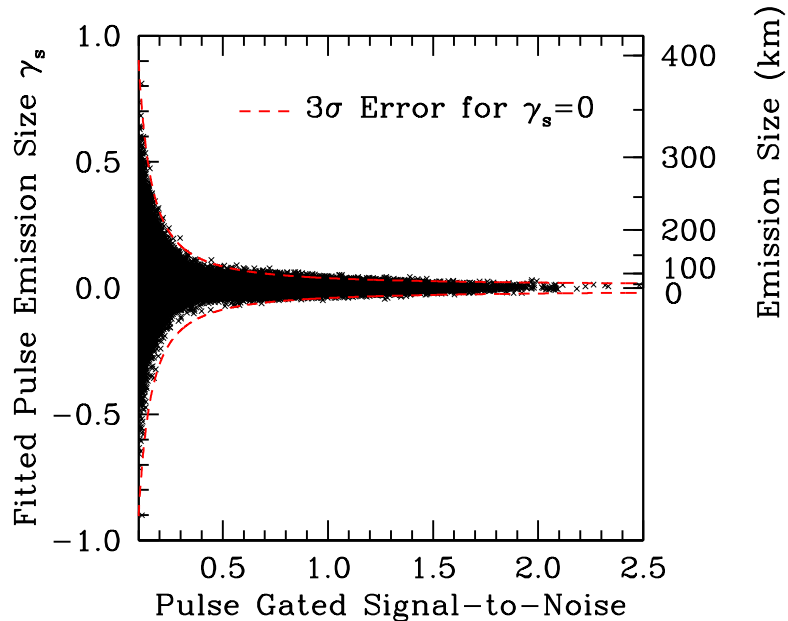


Figure 4.4: Inferred emission sizes of individual pulses as a function of their gated signal-to-noise S ; both linear polarizations are plotted. Because S determines the standard error for each measurement to excellent accuracy, we omit errorbars and instead show the expected $\pm 3\sigma$ errors about $\gamma_s = 0$. We do not obtain a statistically significant detection of emission size for any pulse.

effects. We also account for uncertainties in the detailed distribution and nature of the scattering material.

4.5.1 Effects of Noise in Model Parameters

Noise in the model parameters introduces spurious modulation. Subsequent fits to the spectral statistics will then exhibit a positive bias in γ_s to quench this excess modulation. Fortunately, we can readily characterize the expected noise δA_j and δI_n and can therefore anticipate the influence of such a bias.

For example, the noise δA_j in the source amplitudes is dominated by the finite sampling of the scintillation pattern for a single spectrum; in §2.4.4.2 we

demonstrated that the corresponding bias is $\gamma_s \rightarrow \gamma_s + 1/(4N_{\text{scint}})$, where N_{scint} is the number of averaged scintillation elements used to estimate A_j .

On the other hand, because the background noise is white and approximately stationary, δI_n only depends on the number of samples N_b that are averaged to estimate I_n . However, the incurred bias to γ_s also depends on the gated signal-to-noise ratio S : $\gamma_s \rightarrow \gamma_s + 1/(4S^2N_b)$.

For each 3.2 MHz sub-band, we had $N_{\text{scint}} \sim (3.2 \text{ MHz})/\Delta\nu_d \approx 3,000$, and $N_b \sim 10^5$. Both biases to γ_s were therefore within our quoted confidence. Furthermore, each bias scales as the reciprocal of the analyzed bandwidth. We observed no evolution in the inferred values of γ_s for 1.6 MHz and 0.8 MHz sub-bands and thus confidently established that this class of parameters error did not substantially influence our results.

4.5.2 Effects of Bias in Model Parameters

Instrumental limitations can also lead to errors in the model parameters. For example, interleaved sampling results in a negatively-dedispersed pulse ‘echo’; for highly dispersed pulsars, such as the Vela pulsar, this process can therefore leak pulsed power into the off-pulse region, leading to a positive bias in the estimated background noise: $I_n \rightarrow I_n + \delta I_n$. Alternatively, quantization introduces signal-dependent noise (Jenet & Anderson, 1998; Gwinn, 2006); the off-pulse region then underestimates the effective on-pulse noise.

Of course, any bias in the estimated background noise incurs a corresponding bias in the estimated source amplitude, and vice versa: $\delta I_n = -\delta A_j I_s$. These errors then affect the inferred emission size as $\gamma_s \rightarrow \gamma_s - \delta I_n / (2A I_s)$. Because the dependence of emission size with pulse strength may vary differently than the noise bias, segregating pulses by their gated signal-to-noise can identify the influence of this type of bias. Because we did not observe variation in γ_s between decile subsets, this type of parameter error is unlikely to have significantly corrupted our emission size inference.

We further tested for the presence of a noise bias by comparing the estimates of I_n as a function of pulse strength. Leaked power, for instance, would have introduced a bias that was positively correlated with pulse strength. We detected a slight *negative* trend in our estimates of I_n with pulse strength; the variation in $\langle I_n \rangle$ between the top and bottom deciles (as shown in Figure 4.3) is approximately 0.15%. If this variation reflects a bias in the estimated noise, then the incurred contribution to γ_s is at approximately the 3σ errors we quote. However, the covariance between the fitted values of γ_s and $\langle I_n \rangle$ is marginal, suggesting that this variation in $\langle I_n \rangle$ is not responsible for any appreciable bias in the emission size inference. The variation may instead reflect noise in I_n , which weakly anti-correlates with the gated signal-to-noise of the corresponding pulse. Then, for the full pulse ensemble, the error estimates of §4.5.1 are still appropriate, although the segregation into quantiles will somewhat exaggerate this effect.

Overall, these tests suggest that our 8-bit quantization scheme and high-quality backend (GUPPI) effectively controlled any systematic errors in the model parameters. Remarkably, the determination of γ_s is then limited by the Poisson noise in the observed PDF of intensity (constructed from $\sim 10^9$ samples). Because the transverse size at the source is proportional to $\sqrt{\gamma_s}$, our resolving power scales as the fourth root of the observing duration and bandwidth.

4.5.3 Effects of Modified Scattering Assumptions

Thus far, we have assumed thin-screen scattering with a square-law phase structure function, as is observationally motivated for the Vela pulsar (Williamson, 1972; Komesaroff et al., 1972; Roberts & Ables, 1982; Johnston et al., 1998; Johnson et al., 2013b). However, even with relaxed scattering assumptions, the same form of Eq. 4.1 still applies, with modified scaling.

For example, the translation to a general power-law structure function $D_\phi(\mathbf{x}) \propto |\mathbf{x}|^\alpha$ is given by (see Appendix B)

$$\gamma_{s,\alpha} = \left[\frac{2^{3-\alpha}}{\alpha \Gamma\left(\frac{\alpha}{2}\right)} \gamma_s \right]^{2/\alpha}. \quad (4.9)$$

Hence, if the phase structure function is Kolmogorov ($\alpha = 5/3$), then the effects of a small emission size $\gamma_s \ll 1$ will be somewhat more pronounced than for square-law scattering. The inferred transverse sizes will therefore be *smaller* if we assume $\alpha = 5/3$ than those if we assume $\alpha = 2$. Our given limits $\gamma_{s,\alpha=2} \lesssim 10^{-4}$ translate

to $\gamma_{s,\alpha=5/3} \lesssim 2.3 \times 10^{-5}$, so this alternative scattering environment roughly halves our inferred limits.

The translation from γ_s to a dimensionful emission size also depends on the bulk scattering geometry (see Eq. 4.1). In this case, the uncertainty in the magnification D/R directly affects the inferred emission size. However, the excellent determination of both the temporal and angular broadening of the Vela pulsar lead to relatively small uncertainties for the magnification (Gwinn et al., 2000), and thus the uncertainties for the inferred emission size are within the standard errors from Poisson noise.

4.5.4 Effects of Proper Motion

Because γ_s represents a characteristic size of the emission region, effects such as the proper motion of the pulsar can be important. However, the Vela pulsar has a transverse velocity of only ~ 60 km/s in its local environment (Dodson et al., 2003) – quite slow relative to other young pulsars and the typical neutron star birth velocity (Lyne & Lorimer, 1994). Over our 10 ms accumulation time, the pulsar travels only 600 m. Moreover, since size effects are weighted by pulse amplitude, the relevant timescale is the mean width of individual pulses, typically ~ 2 ms, contributing an effective displacement of ~ 100 m – much smaller than our present detection threshold.

4.6 Interpretation

The simple, conventional picture of pulsar radio emission beamed along lines of a dipolar field provides contact between our measurements and those of traditional approaches to estimate the emission altitude r_{em} . Specifically, this picture enables a translation between the effective transverse size of the emission region, σ_c , and r_{em} . Our measurements of σ_c imply tight limits on r_{em} , in the context of this simple model, while obviating many assumptions of complementary techniques.

In §4.6.1, we review the basic geometric model for pulsar emission. Then, in §4.6.2, we demonstrate how this model relates the transverse size of the emission region to the emission altitude. Next, in §4.6.3, we compare this technique and its result with traditional methods and their conclusions. Finally, in §4.6.4, we discuss possibilities for the discrepancy between our result and previous scintillation analyses of the Vela pulsar.

4.6.1 Geometric Model for Pulsar Emission

A highly-simplified, conventional model describes the geometry of pulsar emission at centimeter and longer wavelengths. Dyks et al. (2004) provide an overview of this model, with a discussion of its assumptions and parameters. We now outline the salient features for completeness. The model assumptions include a dipolar magnetic field, radio-wave emission tangent to field lines, and a single

emission altitude for identifiable features of the average-pulse profile. This model follows from theoretical predictions of an ultra-relativistic electron-positron wind, streaming along the open dipolar field lines in the co-rotating frame (Goldreich & Julian, 1969; Ruderman & Sutherland, 1975; Melrose, 2004), so we assume that the emission is beamed tangent to the field lines into an infinitesimal solid angle. In this case, an observer receives radiation from a single point in the pulsar’s magnetosphere at each pulse phase. The variations of the spatial displacement of this point with pulse phase then determine the apparent size of the emission region.

Because we merely seek a rough correspondence between the size and altitude of the emission region, we ignore effects of relativistic terms, modifications to the dipolar field structure, and magnetospheric ducting and reprocessing (Blaskiewicz et al., 1991; Phillips, 1992; Kapoor & Shukre, 1998; Hibschan & Arons, 2001; Arons & Barnard, 1986; Lai et al., 2001).

A pair of parameters define the orientation of the pulsar: the inclination of the observer relative to the rotational axis (ζ) and the impact angle of the magnetic pole with the line of sight (β). We also employ standard angular coordinates: the longitude or rotational phase of the pulsar (ϕ) and the angle between the point of emission and the magnetic pole ($\theta_{\text{em}}(\phi)$). For a fixed emission altitude r_{em} , the spatial displacement of the point of emission $\vec{D}_{\text{em}}(\phi)$ then follows from the dipolar geometry: $|\vec{D}_{\text{em}}| \approx r_{\text{em}} \tan^{-1}(\theta_{\text{em}}/2)$. The cosine formula of spherical trigonome-

try relates θ_{em} to pulse longitude ϕ and the orientation parameters $\{\beta, \zeta\}$, and the well-known formula for the swing of position angle with ϕ gives the direction of \vec{D} (Komesaroff, 1970). Lyne & Graham-Smith (1998; Figure 16.14) and Lorimer & Kramer (2004; Figure 3.4) provide useful figures and discussion.

The Vela pulsar benefits from several features that permit confident inferences of the orientation parameters. Fits to the X-ray emission from its pulsar wind nebula yield $\zeta \approx 63^\circ$ (Ng & Romani, 2004, 2008). In addition, the swing of the position angle of polarization across the pulse indicates that $\beta \approx -6.5^\circ$ (Radhakrishnan & Cooke, 1969; Johnston et al., 2005). Thus, the Vela pulsar is a nearly-orthogonal rotator, with the line of sight close to the plane of rotation. Note that the duty cycle of the Vela pulsar is quite small. The full angular extent of the emission is only $\rho \approx 16^\circ$ (Johnston et al., 2001), and the effective angular extent, expressed as the standard deviation in pulse phase weighted by flux density, is only $\rho_{\text{eff}} = 3.0^\circ$, from our measurements.

4.6.2 Emission Altitude from Effective Transverse Size

We now relate the effective emission size σ_c to r_{em} , within the context of this geometrical model. A perfectly orthogonal rotator ($\beta = 0$) provides an enlightening demonstration. In this case, the standard deviation of the transverse spatial displacement, weighted by flux-density, is $\sigma_{\text{eff}} \approx \rho_{\text{eff}} r_{\text{em}}/3$. The factor of 1/3 reflects that the angular difference between the tangent and radial directions of

the dipolar field is roughly one third the colatitude of the tangent direction. The translation to an effective circular emission region σ_c then incurs an additional factor: $\sigma_{\text{eff}} = \sqrt{2}\sigma_c$. Applying our most stringent limits for the size of the emission region, $\sigma_c < 4$ km, we obtain $r_{\text{em}} < 3\sqrt{2}\sigma_c/\rho_{\text{eff}} \approx 320$ km.

Applying the measured geometry for a nearly-orthogonal rotator, appropriately weighted by the individual pulse profiles for the stronger linear polarization at 757.5 MHz, we find $r_{\text{em}} \approx 86\sigma_c < 340$ km. Moreover, if we assume that the phase structure function of the scattering medium is Kolmogorov (see §4.5.3), then we obtain $r_{\text{em}} < 170$ km.

4.6.3 Comparison with Previous Emission Altitude Estimates

Our results are comparable with the typical conclusions derived from pulse profile analysis and polarimetry. For example, Kijak & Gil (1997) calculated pulsar emission heights by measuring pulse profile widths at 0.4 and 1.4 GHz and assuming that the emission spanned the open field-line region at a single altitude. For the Vela pulsar at 757.5 MHz, their model predicts $r_{\text{em}} \approx 360$ km.

More generally, the emission may arise from field lines that span only a portion of the open field-line region. Researchers typically characterize this possibility with the fractional colatitude of active field lines $f_\theta \approx \theta_{\text{max}}\sqrt{R_{\text{LC}}/r_{\text{em}}}$. The inferred emission altitude is quite sensitive to the assumed emission structure,

scaling as $\sim f_\theta^{-2}$. However, with strict symmetry assumptions, f_θ can be inferred in pulsars with clearly delineated core and cone components (Gupta & Gangadhara, 2003; Dyks et al., 2004). Such measurements suggest that f_θ generally lies within the range 0.2–0.8 for conal emission.

Alternatively, the aberrational shift in position angle indicates the emission height (Blaskiewicz et al., 1991; Phillips, 1992; Hibschan & Arons, 2001). This shift is insensitive to f_θ and thus gives a robust r_{em} without constraining f_θ . For the Vela pulsar, the position angle offset indicates $r_{\text{em}} \sim 100$ km (Johnston et al., 2001).

A measurement of σ_c concurrently determines f_θ and r_{em} , regardless of the profile morphology or the scatter-broadening. Thus, it can probe the emission structure at low frequencies, where both the size of the emitting region and the effects on the scintillation are most pronounced.

4.6.4 Comparison with 1.66 GHz and 2.3 GHz Scintillation Studies

The sizes that we infer for the emission region are substantially smaller than those found by the previous scintillation analyses discussed in §4.1.2; however, our lack of resolution in pulse phase precludes a direct comparison. For example, if the emitting regions are largest when the pulsar is weak, then the effects of emission size will be diminished. Indeed, the phase-resolved analysis at 1.66 GHz sug-

gests precisely this scenario. Furthermore, our observations span lower frequencies than previous analyses. Although the radius-to-frequency mapping (Ruderman & Sutherland, 1975; Cordes, 1978) suggests that the emission height decreases with increasing frequency, the Vela pulsar possibly does not conform to this picture. Alternatively, the pulse profile shows considerable intrinsic evolution at 1 GHz, and the disparity between the measured emission size may indicate the introduction of a new, offset emission component at these higher frequencies. Pending observations should resolve this intriguing discrepancy.

4.7 Summary

We have analyzed flux-density statistics of the Vela pulsar at 760 MHz. In particular, we examined the observed PDF of intensity in various cuts determined by frequency, polarization, and pulse strength. Based on single pulse estimates of the background noise and gated signal-to-noise, we constructed model PDFs in order to identify the signature arising from a spatially-extended emission region.

The predicted form for point-source emission showed excellent agreement with the data ($\chi_{\text{red}}^2 \approx 1$), good to $\sim 0.01\%$ over the low to moderate intensity regions of the PDF, in which the effects of an extended emission region are the most pronounced. This type of comparison requires no fitted parameters and arises from minimal assumptions about the characteristics of both the scattering (i.e.

strong and slowly evolving) and source emission (i.e. amplitude-modulated noise with small spatial extent). Our inferences are therefore extremely robust.

We did not detect any effects arising from an extended emission region. We achieved the tightest limit by jointly analyzing all pulses in three 3.2 MHz sub-bands, centered on 751.25, 757.5, and 763.75 MHz; this limit corresponds to a characteristic size of the emission region of $\sigma_c \lesssim 4$ km at the pulsar at 3σ confidence. This limit involved information about the nature and distribution of the scattering material. If the phase structure function of the scattering material is Kolmogorov, for instance, then the limit decreases to $\sigma_c \lesssim 2$ km.

The inferred size, σ_c , reflects the spatial extent of all the emitting regions during a pulse and, therefore, also gives an upper-bound on the instantaneous emission size, which we assume is pointlike in our derivation of the emission altitude. Explicitly, σ_c corresponds to the standard deviation of a circular Gaussian distribution of intensity that yields equivalent scintillation statistics as those observed. Conversion to an emission altitude also involves the effective angular pulse width, weighted by flux density, which provides a natural mapping to lateral emission structure. We thereby obtained constraints on the emission altitude: $r_{\text{em}} < 340$ km (square-law) or $r_{\text{em}} < 170$ km (Kolmogorov).

We also individually tested pulses for the signature of an extended emission region, again without a statistically significant detection. For the strongest pulses we obtained limits $\lesssim 50$ km, and for the majority of pulses we obtained limits

$\lesssim 200$ km. However, even for the strongest pulses, this bound only marginally constrained the emission to be generated within the light cylinder. Nevertheless, our results demonstrate the application and reliability of this technique.

Our upper bound on the size of the emission region improves previous estimates using scintillation statistics by over an order of magnitude. Without invoking symmetry constraints or assumptions about the distribution of emission within the open field-line region, we achieve estimates of the emission altitude that are comparable with alternative techniques that analyze profile widths and polarization characteristics. Thus, even for incredibly compact ‘core’ emission, scintillation statistics now have the ability to refine and extend the information conveyed by bulk polarimetry.

The excellent agreement between our data and models demonstrates that our technique can be similarly applied to other pulsars without fear of spurious inference. In particular, the quality of our data appears to have controlled the systematic uncertainties to be within the fundamental restriction set by Poisson noise. Thus, future observations, perhaps at lower frequencies or of other pulsars with favorable scattering geometries, may confidently measure a spatially-extended emission region and thereby greatly enrich our empirical understanding of pulsar radio emission.

Chapter 5

The Effects of Refractive Substructure on Ultra-Long-Baseline Visibilities

5.1 Refractive Scintillation and Noise

Thus far, this dissertation has focused on diffractive scintillation. We have noted that, for strongly scattered sources, a sufficiently wide bandwidth will sample an excellent representation of the diffractive scintillation. However, as discussed in Chapter 1, *refractive* scintillation imparts an additional, gentle modulation, which is coherent over fractional bandwidths of order unity and timescales of weeks to months.

Refractive scintillation arises from large-scale correlations across the scattering screen, which steer and focus the scattered radiation. Refractive effects are much less sensitive to an extended emission region and only become quenched when the size of the source emission region is comparable to that of the scattering disk. Hence, refractive variations are an important consideration for sources such as

AGN. In some cases, a lack or suppression of refractive variations can be used to infer the source brightness temperature (e.g. Ozernoi & Shishov, 1979; Gwinn et al., 1991). For smaller sources, such as pulsars, refractive variations can provide information about the scattering material, particularly the large-scale correlations in density fluctuations.

Yet, characterizing refractive effects is quite challenging, requiring observations that extend over many months. In addition, decoupling intrinsic variability from refractive variations generally requires additional assumptions about both (see, for instance, Macquart & Bower, 2006).

In this chapter, we will develop a different type of refractive metric: the noise measured by an interferometer on baselines that are many times the scale of the diffraction pattern. Narayan & Goodman (1989; hereafter NG89) and Goodman & Narayan (1989; hereafter GN89) demonstrated that the refractive contribution to noise, which arises from substructure within the scattering disk, can dominate measurements on such long baselines. Moreover, this noise can be easily decoupled from intrinsic variability and can provide information about the source and scattering properties without sampling a refractive ensemble. It therefore provides a robust and rapid mechanism for quantifying refractive effects.

Hence, we will extend the analytical treatment of GN89 in several directions. We account for source emission structure and scattering geometry. In addition, we provide results for both one-dimensional and two-dimensional distributions of

scattering material, as is observationally motivated. We also include the possibility of anisotropy in the scattering material and demonstrate that refractive noise is quite sensitive to anisotropy. We establish the full PDF of refractive noise, on the basis of simulations, thereby quantifying how a single measurement varies among observing epochs.

We conclude this chapter by outlining the possibilities for utilizing refractive noise as a source of fresh insight into the intrinsic structure of heavily-scattered objects and the nature of the ionized ISM.

5.2 Scattering and Scintillation

We now extend the discussion of the phase structure function given in §1.3.1. In §5.2.1, we describe the various regimes of the phase structure function and present a generic functional form. Next, in §5.2.2 we establish the three averaging regimes and their relation to noise and scintillation.

5.2.1 The Phase Structure Function

As we have discussed in §1.3.1, for a statistically homogeneous medium with density fluctuations that correspond to a Gaussian random field, the phase structure function $D_\phi(\mathbf{x})$ contains all the information needed to describe the effects of scattering. Radio astronomical observations indicate that the structure function exhibits a power-law over many orders of magnitude, suggestive of a turbulent

cascade between some inner, dissipation scale r_{in} and an outer, injection scale r_{out} (e.g. Armstrong et al., 1995). Between these scales, $D_\phi(r) \propto r^\alpha$.¹ On shorter scales, the phase fluctuations are smooth, so $D_\phi(r) \propto r^2$, while on longer scales, D_ϕ is constant (Tatarskii, 1971). For the remainder of this chapter, we will assume that the outer scale is much larger than the size of the scattering disk and, thus, is inconsequential.

To encompass this behavior in a simple functional form, we will use the following expression (GN89):

$$\begin{aligned}
 D_\phi(\mathbf{r}) &= C \left[(r^2 + r_{\text{in}}^2)^{\alpha/2} - r_{\text{in}}^\alpha \right] \\
 &= \frac{(r^2 + r_{\text{in}}^2)^{\alpha/2} - r_{\text{in}}^\alpha}{(r_0^2 + r_{\text{in}}^2)^{\alpha/2} - r_{\text{in}}^\alpha}.
 \end{aligned}
 \tag{5.1}$$

Here, we introduce a frequency-dependent constant $C \propto \nu^{-2}$, reflecting the behavior of the index of refraction for frequencies much greater than the plasma frequency (see Eq. 1.4), and the phase coherence length r_0 , defined by $D_\phi(r_0) \equiv 1$. Observe that, with the inclusion of an inner scale, r_0 has no simple scaling with frequency.

¹In this section, we assume that the scattering is statistically isotropic. For anisotropic scattering, see §5.4.2.4.

As in GN89, we will focus on two limiting cases. For a negligible inner scale, $r_{\text{in}} \ll r_0$, we have

$$D_\phi(r) \approx \left(\frac{r}{r_0}\right)^\alpha. \quad (5.2)$$

On the other hand, if $r_{\text{in}} \gg r_0$ then

$$D_\phi(r) \approx \begin{cases} \left(\frac{r}{r_0}\right)^2 & \text{if } r \ll r_{\text{in}}, \\ \frac{2}{\alpha} \left(\frac{r_{\text{in}}}{r_0}\right)^{2-\alpha} \left(\frac{r}{r_0}\right)^\alpha & \text{if } r \gg r_{\text{in}}. \end{cases} \quad (5.3)$$

Note that this form corrects a slight omission in Eq. 3.1.3 of GN89. While the power-law form at large r is equivalent in the two cases, the correspondence between the C and r_0 is affected by an inner scale:

$$C \approx \begin{cases} r_0^{-\alpha} & \text{if } r_{\text{in}} \ll r_0, \\ \frac{2}{\alpha} \left(\frac{r_{\text{in}}}{r_0}\right)^{2-\alpha} r_0^{-\alpha} & \text{if } r_{\text{in}} \gg r_0. \end{cases} \quad (5.4)$$

5.2.2 The Averaging Regimes for Interferometric Visibility

The phase structure function is intimately related to interferometric visibility, albeit in a typically inaccessible regime because, in practice, noise related to the scattering significantly affects measured visibilities. This noise is dominated by two distinct branches, and, following GN89, we will consider three types of en-

semble averages for the visibility. A *snapshot visibility*, V_{ss} , averages over source and background noise for a single realization of the scintillation pattern. An *average visibility*, V_a , averages also over diffractive scintillation but not refractive scintillation. An *ensemble-average visibility*, V_{ea} , averages over both diffractive and refractive scintillation. We also use these subscripts on averages (e.g. $\langle \dots \rangle_{ss}$) to denote the appropriate ensemble.

While individual observations of compact, scintillating objects can often readily probe the snapshot and average-image regimes (see, e.g., Chapter 4), the ensemble-average requires a series of measurements taken over months or years.

5.3 Interferometric Visibility from Kirchoff Diffraction

In this section, we will derive the relationship between the phase structure function and the ensemble-average visibility. Of course, this relationship is well-known, but it serves to establish our notation and assumptions for later calculations. We begin by introducing the representation of the scalar electric field from Kirchoff diffraction; we then evaluate the ensemble-average visibility and relate it to the phase structure function.

5.3.1 The Scalar Electric Field

Because we are ultimately interested in both one- and two- dimensional scattering geometries, we first consider d -dimensional scattering. Applying Kirchoff diffrac-

tion theory, we write the scalar electric field at the observer as (see, for instance, Gwinn et al., 1998)

$$\psi(\mathbf{b}) = \frac{1}{(\sqrt{2\pi}r_F)^d} \int_{\text{screen}} d^d \mathbf{x} e^{i\left[\left(\frac{k}{2D}\right)|\mathbf{b}-\mathbf{x}|^2 + \phi(\mathbf{x})\right]} \int_{\text{source}} d^d \mathbf{s} e^{i\left(\frac{k}{2R}\right)|\mathbf{x}-\mathbf{s}|^2} \psi_{\text{source}}(\mathbf{s}), \quad (5.5)$$

Here, \mathbf{b} is a transverse coordinate in the observing plane, and $\phi(\mathbf{x})$ is the screen phase (see §1.3.1). As in other chapters, D is the characteristic Earth-scatterer distance, R is the characteristic source-scatterer distance, k is the wavenumber, and r_F is the Fresnel scale, defined by²

$$r_F \equiv \sqrt{\frac{DR}{D+R} \frac{1}{k}}. \quad (5.6)$$

We have chosen the prefactor of Eq. 5.5 so that $\langle |\psi(\mathbf{b})|^2 \rangle_{\text{ea}} = 1$. We will write most subsequent equations in terms of r_F and the effective magnification $M \equiv D/R$ of the scattering screen. We will also employ the scaled baseline $\mathbf{B} \equiv (1+M)^{-1}\mathbf{b}$.

²We caution that this definition of the Fresnel scale differs slightly from that of previous chapters.

5.3.2 The Ensemble-Average Visibility

For a spatially-incoherent source, the snapshot visibility on a baseline \mathbf{b} is

$$\begin{aligned}
 V_{\text{ss}}(\mathbf{b}) &\equiv \overline{\psi(-\mathbf{b}/2)\psi^*(\mathbf{b}/2)} \\
 &= \frac{1}{(2\pi r_{\text{F}}^2)^d} \int d^d \mathbf{x}_1 d^d \mathbf{x}_2 e^{i\frac{1}{2}r_{\text{F}}^{-2}[(1+M)(x_1^2-x_2^2)+\mathbf{b}\cdot(\mathbf{x}_1+\mathbf{x}_2)]} e^{i[\phi(\mathbf{x}_1)-\phi(\mathbf{x}_2)]} \\
 &\quad \times \int d^d \mathbf{s} e^{i\frac{k}{R}(\mathbf{x}_2-\mathbf{x}_1)\cdot\mathbf{s}} I_{\text{source}}(\mathbf{s}).
 \end{aligned} \tag{5.7}$$

To obtain the ensemble-average visibility, we must average over many realizations of the scattering screen, defined by the Gaussian random field $\phi(\mathbf{x})$. To calculate this average, the characteristic function of a zero-mean Gaussian random variable provides a convenient identity: $\langle e^{i[\phi(\mathbf{x}_1)-\phi(\mathbf{x}_2)]} \rangle_{\text{ea}} = e^{-\frac{1}{2}\langle [\phi(\mathbf{x}_1)-\phi(\mathbf{x}_2)]^2 \rangle_{\text{ea}}} = e^{-\frac{1}{2}D_\phi(\mathbf{x}_1-\mathbf{x}_2)}$. We can then change the integration variables to $\mathbf{u} \equiv \mathbf{x}_1 - \mathbf{x}_2$ and $\mathbf{v} \equiv (\mathbf{x}_1 + \mathbf{x}_2)/2$ to obtain

$$V_{\text{ea}}(\mathbf{b}) = \frac{1}{(2\pi r_{\text{F}}^2)^d} \int d^d \mathbf{u} d^d \mathbf{v} e^{ir_{\text{F}}^{-2}[(1+M)\mathbf{u}+\mathbf{b}]\cdot\mathbf{v}} e^{-\frac{1}{2}D_\phi(\mathbf{u})} \int d^d \mathbf{s} e^{i\frac{k}{R}\mathbf{u}\cdot\mathbf{s}} I_{\text{source}}(\mathbf{s}). \tag{5.8}$$

Integration over \mathbf{v} is trivial, using the identity $\int d^d \mathbf{v} e^{i\mathbf{y}\cdot\mathbf{v}} = (2\pi)^d \delta^d(\mathbf{y})$. Thus,

$$V_{\text{ea}}(\mathbf{b}) = e^{-\frac{1}{2}D_\phi(\mathbf{b})} \int d^d \mathbf{s} e^{i\left(\frac{M}{1+M}\right)r_{\text{F}}^{-2}\mathbf{b}\cdot\mathbf{s}} I_{\text{source}}(\mathbf{s}). \tag{5.9}$$

Hence, we recover the usual result that the visibility is the product of the point source visibility and the Fourier transform of the source intensity distribution. In fact, the effects of an extended emission region are equivalent to integration over the observing plane with an appropriate apodizer.

As a concrete example, suppose that $I_{\text{source}}(\mathbf{s})$ is a circular Gaussian distribution with variance $\langle s^2 \rangle = d \cdot \sigma$. Then,

$$V_{\text{ea}}(\mathbf{b}) = e^{-\frac{1}{2}D_\phi(\mathbf{b})} e^{-\frac{1}{2}\left(\frac{M}{1+M}\frac{\sigma B}{r_F^2}\right)^2}. \quad (5.10)$$

Because we are interested in comparisons with observables, consider the measurable quantity b_0 , defined by $V_{\text{ea}}(b_0) \equiv 1/\sqrt{e}$. Then, for isotropic square-law scattering or for $r_{\text{in}} \gg r_0$,

$$V_{\text{ea}}(b) = e^{-\frac{1}{2}\left(\frac{b}{b_0}\right)^2}, \quad (5.11)$$

$$b_0 \equiv \frac{(1+M)r_0}{\sqrt{1+\gamma_{\text{s,R}}}},$$

where we have introduced the dimensionless refractive size parameter $\gamma_{\text{s,R}}$

$$\gamma_{\text{s,R}} \equiv \left(\frac{M}{M+1}\frac{r_0\sigma}{r_F^2}\right)^2. \quad (5.12)$$

Recall that in previous chapters, we used the dimensionless parameter γ_{s} – the squared source emission size in units of the magnified diffractive scale. We see

that $\gamma_{s,R}$ is instead the squared source emission size in units of the appropriately magnified refractive scale.

Now, since the angular broadening $\theta \sim 1/(kb_0)$, the effects of source size and scattering add at quadrature. Because of the steep ($\propto \nu^{-(1+\alpha/2)}$) variation of angular broadening with frequency, multifrequency observations can readily distinguish the effects of scattering from those of intrinsic structure (e.g. Doeleman et al., 2008).

5.4 Refractive Noise

We now calculate the variance of the refractive noise, which is simply the noise $\Delta V_a \equiv V_a - V_{ea}$ in the average visibility. We begin, in §5.4.1, by calculating the second moment of the snapshot visibility modulus: $\langle |V_{ss}|^2 \rangle_{ea}$. Next, in §5.4.2, we identify the contribution of refractive noise to this moment by isolating the contribution of the ensemble-average visibility and of diffraction noise; we also give analytical approximations to the refractive noise in various regimes and quantify the influence of anisotropic scattering. Finally, in §5.4.3, we estimate the full distribution of refractive noise.

5.4.1 The Second Moment of $|V_{ss}|$

To calculate the variance of the snapshot visibility modulus, we square Eq. 5.7 before evaluating the ensemble average over the screen phases. Next, we again

apply the identity for the exponential of a Gaussian random variable to obtain

$$\begin{aligned} \left\langle e^{i[\phi(\mathbf{x}_1)-\phi(\mathbf{x}_2)-\phi(\mathbf{x}_3)+\phi(\mathbf{x}_4)]} \right\rangle_{\text{ea}} &= e^{-\frac{1}{2}\langle(\phi(\mathbf{x}_1)-\phi(\mathbf{x}_2)-\phi(\mathbf{x}_3)+\phi(\mathbf{x}_4))^2\rangle_{\text{ea}}} \\ &= e^{-\frac{1}{2}[D_\phi(\Delta\mathbf{x}_{13})+D_\phi(\Delta\mathbf{x}_{24})+D_\phi(\Delta\mathbf{x}_{12})-D_\phi(\Delta\mathbf{x}_{14})-D_\phi(\Delta\mathbf{x}_{23})+D_\phi(\Delta\mathbf{x}_{34})]}, \end{aligned} \quad (5.13)$$

where $\Delta\mathbf{x}_{ij} \equiv \mathbf{x}_i - \mathbf{x}_j$. Using the Hadamard transform, we can then change variables to exploit this pairwise representation:

$$\begin{pmatrix} \mathbf{y}_1 \\ \mathbf{y}_2 \\ \mathbf{y}_3 \\ \mathbf{y}_4 \end{pmatrix} = \frac{1}{2} \begin{pmatrix} 1 & 1 & 1 & 1 \\ 1 & -1 & 1 & -1 \\ 1 & 1 & -1 & -1 \\ 1 & -1 & -1 & 1 \end{pmatrix} \begin{pmatrix} \mathbf{x}_1 \\ \mathbf{x}_2 \\ \mathbf{x}_3 \\ \mathbf{x}_4 \end{pmatrix}. \quad (5.14)$$

Note that the structure functions of Eq. 5.13 can be written using only $\{\mathbf{y}_{2,3,4}\}$.

Finally, we can apply the identity $x_1^2 - x_2^2 - x_3^2 + x_4^2 = 2(\mathbf{y}_1 \cdot \mathbf{y}_4 + \mathbf{y}_2 \cdot \mathbf{y}_3)$ to obtain

$$\begin{aligned} \langle |V_{\text{ss}}(\mathbf{b})|^2 \rangle_{\text{ea}} &= \frac{1}{(2\pi r_{\text{F}}^2)^{2d}} \int d^2\mathbf{y}_i e^{ik[(\mathbf{y}_1 \cdot \mathbf{y}_4 + \mathbf{y}_2 \cdot \mathbf{y}_3)(\frac{1}{D} + \frac{1}{R}) + \frac{1}{D}\mathbf{b} \cdot \mathbf{y}_3]} \\ &\times e^{-\frac{1}{2}[D_\phi(\Delta\mathbf{x}_{13})+D_\phi(\Delta\mathbf{x}_{24})+D_\phi(\Delta\mathbf{x}_{12})-D_\phi(\Delta\mathbf{x}_{14})-D_\phi(\Delta\mathbf{x}_{23})+D_\phi(\Delta\mathbf{x}_{34})]} \\ &\times \int d^2\mathbf{s}_1 d^2\mathbf{s}_2 e^{i(\frac{k}{R})[-(\mathbf{y}_2 + \mathbf{y}_4) \cdot \mathbf{s}_1 - (\mathbf{y}_4 - \mathbf{y}_2) \cdot \mathbf{s}_2]/(2R)} I_{\text{source}}(\mathbf{s}_1) I_{\text{source}}(\mathbf{s}_2). \end{aligned} \quad (5.15)$$

Observe that the source integrals factorize.

Now, we can integrate over \mathbf{y}_1 to obtain $\frac{4\pi^2}{k^2} \left(\frac{1}{D} + \frac{1}{R}\right)^{-2} \delta(\mathbf{y}_4)$ and then integrate over \mathbf{y}_4 to leave

$$\begin{aligned} \langle |V_{\text{ss}}(\mathbf{b})|^2 \rangle_{\text{ea}} &= \frac{1}{(2\pi r_{\text{F}}^2)^d} \int d^d \mathbf{y}_{2,3} e^{ir_{\text{F}}^{-2}[\mathbf{y}_2 + \mathbf{B}] \cdot \mathbf{y}_3} e^{-\frac{1}{2}[2D_\phi(\mathbf{y}_3) + 2D_\phi(\mathbf{y}_2) - D_\phi(\mathbf{y}_2 + \mathbf{y}_3) - D_\phi(\mathbf{y}_2 - \mathbf{y}_3)]} \\ &\quad \times \left| \int d^d \mathbf{s} e^{i\frac{k}{R}\mathbf{s} \cdot \mathbf{y}_2} I_{\text{source}}(\mathbf{s}) \right|^2. \end{aligned} \quad (5.16)$$

5.4.2 Refractive Noise

Three effects contribute to a snapshot visibility: diffractive noise, refractive noise, and $V_{\text{ea}}(b)$. However, each arises from a different region of the integral for the second moment, expressed in Eq. 5.16.

For $\alpha < 2$, the dominant contributions to the integral have at least one of $\{y_2, y_3\} \lesssim r_0$. The region $\{y_2 \gg r_0, y_3 \lesssim r_0\}$ gives the diffractive noise, as is evident by its suppression from an extended source.

The remaining region of the integral gives the second moment of $|V_{\text{a}}|$. To isolate the noise ΔV_{a} , note that the contribution of V_{ea} can be written as

$$\begin{aligned} \frac{1}{(2\pi r_{\text{F}}^2)^d} \int d^d \mathbf{y}_{2,3} e^{ir_{\text{F}}^{-2}[\mathbf{y}_2 + \mathbf{B}] \cdot \mathbf{y}_3} e^{-D_\phi(\mathbf{y}_2)} \left| \int d^d \mathbf{s} e^{i\frac{k}{R}\mathbf{s} \cdot \mathbf{y}_2} I_{\text{source}}(\mathbf{s}) \right|^2 \\ = e^{-D_\phi(\mathbf{B})} \left| \int d^d \mathbf{s} e^{i\frac{k}{R}\mathbf{s} \cdot \mathbf{B}} I_{\text{source}}(\mathbf{s}) \right|^2 = |V_{\text{ea}}(\mathbf{b})|^2. \end{aligned} \quad (5.17)$$

Moreover, we will ignore the phase variations $e^{ir_F^{-2}\mathbf{y}_2\cdot\mathbf{y}_3}$ in Eq. 5.16, which are small over the region that dominates the refractive contribution.³ For simplicity, we will again assume an isotropic source with spatial variance $\sigma \cdot d$. Hence, the refractive noise is given by

$$\begin{aligned} \langle |\Delta V_a|^2 \rangle_{\text{ea}} &\approx \frac{1}{(2\pi r_F^2)^d} \int_{\substack{y_2 \lesssim r_0 \\ y_3 \gg r_0}} d^d \mathbf{y}_{2,3} e^{ir_F^{-2}\mathbf{B}\cdot\mathbf{y}_3} e^{-D_\phi(\mathbf{y}_2)} e^{-\gamma_{s,R}\left(\frac{y_2}{r_0}\right)^2} \\ &\times \left[\exp \left\{ -\frac{1}{2} [2D_\phi(\mathbf{y}_3) - D_\phi(\mathbf{y}_2 + \mathbf{y}_3) - D_\phi(\mathbf{y}_2 - \mathbf{y}_3)] \right\} - 1 \right]. \end{aligned} \quad (5.18)$$

At this point, it is simpler to proceed by examining the cases $d = 1$ and $d = 2$ separately.

5.4.2.1 One-Dimensional, Isotropic Scattering

We now calculate the refractive noise for one-dimensional isotropic scattering. For clarity, we will first determine the noise for a point source. The appropriate modification for an extended emission region is given in §5.4.2.3.

We begin by expanding the exponential of the structure functions for $|y_2| \ll |y_3|$:

$$\exp \left\{ -\frac{1}{2} [2D_\phi(y_3) - D_\phi(y_2 + y_3) - D_\phi(y_2 - y_3)] \right\} - 1 \approx \frac{1}{2} y_2^2 D_\phi''(y_3). \quad (5.19)$$

³These phase variations give an $\mathcal{O}(r_0/\mathcal{B})^2$ correction to our derived results.

With this approximation, the integral factorizes:

$$\begin{aligned} \langle |\Delta V_a|^2 \rangle &\approx \frac{1}{4\pi r_F^2} \left[\int dy_3 D_\phi''(y_3) e^{i\mathcal{B}y_3/r_F^2} \right] \left[\int dy_2 y_2^2 e^{-D_\phi(y_2)} \right] \\ &= \frac{1}{4\pi r_F^2} \left(\frac{\mathcal{B}}{r_F^2} \right)^2 \left[- \int dy_3 D_\phi(y_3) e^{i\mathcal{B}y_3/r_F^2} \right] \left[\int dy_2 y_2^2 e^{-D_\phi(y_2)} \right]. \end{aligned} \quad (5.20)$$

The second integral is dominated by $y_2 \lesssim r_0$ and, thus, depends on whether the inner scale influences the phase variations in that regime:

$$\int dy_2 y_2^2 e^{-D_\phi(y_2)} = r_0^3 \times \begin{cases} \sqrt{\pi}/2 & r_{\text{in}} \gg r_0, \\ \frac{2}{\alpha} \Gamma\left(\frac{3}{\alpha}\right) & r_{\text{in}} \ll r_0. \end{cases} \quad (5.21)$$

Meanwhile, the first integral is related to the power spectrum of the phase fluctuations and has a closed-form solution in our representation:

$$- \int dy_3 D_\phi(y_3) e^{i\mathcal{B}y_3/r_F^2} = C \frac{2^{(3+\alpha)/2} \sqrt{\pi}}{\Gamma(-\alpha/2)} \left(\frac{r_{\text{in}} r_F^2}{\mathcal{B}} \right)^{\frac{\alpha+1}{2}} K_{\frac{\alpha+1}{2}} \left(\frac{r_{\text{in}} \mathcal{B}}{r_F^2} \right), \quad (5.22)$$

where $K_n(x)$ is the modified Bessel function of the second kind. Expanding the Bessel function to leading order gives an excellent approximation when $\frac{r_{\text{in}} \mathcal{B}}{r_F^2} \ll 1$:

$$- \int dy_3 D_\phi(y_3) e^{i\mathcal{B}y_3/r_F^2} \approx 2C\Gamma(\alpha+1) \sin\left(\frac{\pi\alpha}{2}\right) \left(\frac{r_F^2}{\mathcal{B}} \right)^{\alpha+1}. \quad (5.23)$$

This expression is, of course, equivalent to only considering the asymptotic power-law portion of $D_\phi(r \gg r_{\text{in}})$.

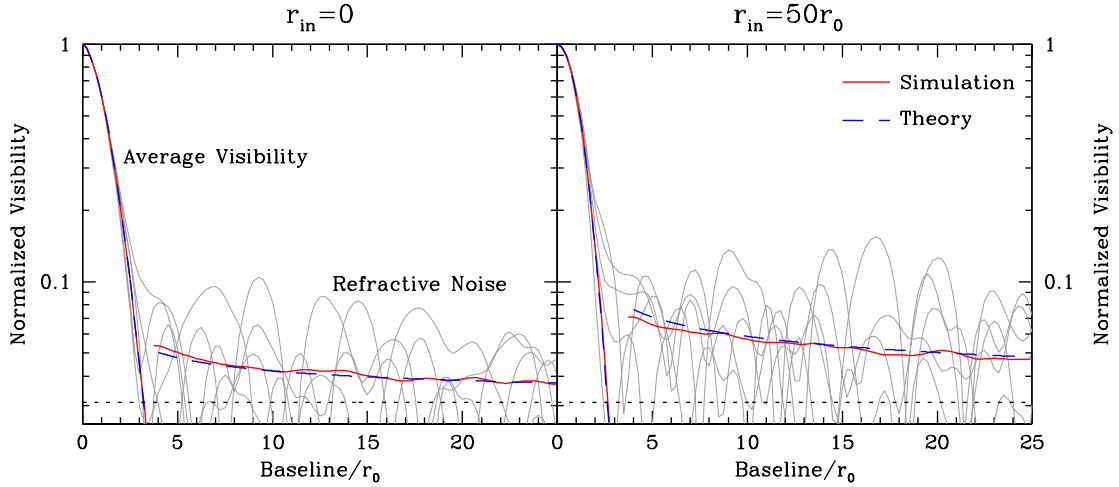


Figure 5.1: The ensemble average and noise for average visibilities from simulations and theory for a one-dimensional scattering screen. The scattering parameters are $\alpha = 5/3$, $r_0 = 2$. Each simulation uses a scattering screen determined by $2^{20} \approx 10^6$ correlated phases; we generated 1000 independent realizations of the scattering screen to determine ensemble averages. The left plot is for $r_{\text{in}} = 0$, while the right has $r_{\text{in}} = 50r_0$. The noise includes both a diffractive and a refractive contribution. The black dotted line shows the diffractive contribution, which is constant with baseline and is added at quadrature to the refractive contribution, which decreases with baseline. The gray curves show example visibility curves for individual scattering screens.

Putting everything together gives

$$\langle |\Delta V_a|^2 \rangle \approx \frac{1}{\pi} \Gamma(\alpha) \sin\left(\frac{\pi\alpha}{2}\right) \left(\frac{r_0}{r_F}\right)^{2(2-\alpha)} \left(\frac{\mathcal{B}}{r_0}\right)^{1-\alpha} \times \begin{cases} \Gamma(3/\alpha) & r_{\text{in}} \ll r_0, \\ \frac{\sqrt{\pi}}{2} \left(\frac{r_{\text{in}}}{r_0}\right)^{2-\alpha} & r_{\text{in}} \gg r_0. \end{cases} \quad (5.24)$$

Hence, a large inner scale will increase the RMS refractive noise by a factor of $\sim (r_{\text{in}}/r_0)^{1-\alpha/2}$. See Figure 5.1 for comparisons of this expected noise with the results of simulations.

5.4.2.2 Two-Dimensional, Isotropic Scattering

Once again, we first consider emission from a point source. We outline the effects of an extended emission region in §5.4.2.3.

For a two-dimensional, isotropic structure function and $y_2 \ll y_3$,

$$D_\phi(\mathbf{y}_2 + \mathbf{y}_3) + D_\phi(\mathbf{y}_2 - \mathbf{y}_3) \approx 2D_\phi(y_3) + \frac{y_2^2}{y_3} \sin^2(\theta) D'_\phi(y_3) + y_2^2 \cos^2(\theta) D''_\phi(y_3), \quad (5.25)$$

where θ is the angle between \mathbf{y}_2 and \mathbf{y}_3 . We can now substitute Eq. 5.25 into Eq. 5.18, keeping in mind the assumption that $y_2 \ll y_3$. Then,

$$\begin{aligned} \langle |\Delta V_a|^2 \rangle_{\text{ea}} &= \frac{1}{8\pi^2 r_F^4} \int d^2 \mathbf{y}_2 d^2 \mathbf{y}_3 \left[\frac{1}{y_3} \sin^2(\theta) D'_\phi(y_3) + \cos^2(\theta) D''_\phi(y_3) \right] \quad (5.26) \\ &\quad \times e^{i\mathbf{B} \cdot \mathbf{y}_3 / r_F^2} y_2^2 e^{-D_\phi(y_2)}. \end{aligned}$$

We can immediately integrate θ but, for clarity, we will simply make the substitution $\sin^2 \theta, \cos^2 \theta \rightarrow 1/2$ and retain the two-dimensional integrals, which then factorize:

$$\begin{aligned} \langle |\Delta V_a|^2 \rangle_{\text{ea}} &= \frac{1}{16\pi^2 r_F^4} \left\{ \int d^2 \mathbf{y}_3 \left[\frac{1}{y_3} D'_\phi(y_3) + D''_\phi(y_3) \right] e^{i\mathbf{B} \cdot \mathbf{y}_3 / r_F^2} \right\} \left\{ \int d^2 \mathbf{y}_2 y_2^2 e^{-D_\phi(y_2)} \right\} \\ &= \frac{1}{8\pi r_F^4} \left\{ \int dy_3 d\theta_3 [D'_\phi(y_3) + y_3 D''_\phi(y_3)] e^{iB y_3 \cos \theta_3 / r_F^2} \right\} \left\{ \int_0^\infty dy_2 y_2^3 e^{-D_\phi(y_2)} \right\}. \quad (5.27) \end{aligned}$$

Here, θ_3 is the polar angle of \mathbf{y}_3 .

The second integral once again depends only on the behavior of the structure function for $r \lesssim r_0$:

$$\int_0^\infty dy_2 y_2^3 e^{-D_\phi(y_2)} = r_0^4 \times \begin{cases} 1/2 & r_{\text{in}} \gg r_0 \\ \frac{1}{\alpha} \Gamma\left(\frac{4}{\alpha}\right) & r_{\text{in}} \ll r_0. \end{cases} \quad (5.28)$$

Meanwhile, as we saw for the one-dimensional case, the first integral can be estimated by only considering the power-law character in the asymptotic region $D_\phi(r \gg r_{\text{in}})$. Putting everything together, we obtain

$$\langle |\Delta V_{\text{a}}|^2 \rangle_{\text{ea}} \approx 2^{\alpha-2} \frac{\Gamma(\alpha/2 + 1)}{\Gamma(1 - \alpha/2)} \left(\frac{r_0}{r_{\text{F}}}\right)^{2(2-\alpha)} \left(\frac{\mathcal{B}}{r_0}\right)^{-\alpha} \times \begin{cases} \Gamma(4/\alpha) & r_{\text{in}} \ll r_0, \\ \left(\frac{r_{\text{in}}}{r_0}\right)^{2-\alpha} & r_{\text{in}} \gg r_0. \end{cases} \quad (5.29)$$

5.4.2.3 The Effects of an Extended Emission Region

An extended emission region only modifies the behavior of the integral over \mathbf{y}_2 (see Eq. 5.18). Because this integral is regulated by $\exp[-D_\phi(y_2)]$, numerical evaluation presents no difficulties, even for arbitrary source emission geometry. However, to facilitate intuition for the effects of an extended emission region, we now give analytical results in limiting cases.

Evidently, the effects of size depend only on the region $y_2 \lesssim r_0$. In both cases that we have considered, the behavior of $D_\phi(r)$ in this range is a power-law.

Moreover, we see that the effects of size are to induce a change in the overall amplitude of the refractive noise – to leading order, this change will not vary with baseline.

For $\gamma_{s,R} \ll 1$, we can expand the exponential that accounts for source size. We see that, for $r_{\text{in}} \ll r_0$, the variance $\langle |\Delta V_a|^2 \rangle_{\text{ea}}$ is suppressed by a constant factor:

$$\langle |\Delta V_a(\gamma_{s,R})|^2 \rangle_{\text{ea}} \approx \langle |\Delta V_a(\gamma_{s,R} = 0)|^2 \rangle_{\text{ea}} \times \begin{cases} 1 - \frac{\Gamma(5/\alpha)}{\Gamma(3/\alpha)} \gamma_{s,R} & d = 1, \\ 1 - \frac{\Gamma(6/\alpha)}{\Gamma(4/\alpha)} \gamma_{s,R} & d = 2. \end{cases} \quad (5.30)$$

On the other hand, if $r_{\text{in}} \gg r_0$, then the results are equivalent, with the substitution $\alpha = 2$:

$$\langle |\Delta V_a(\gamma_{s,R})|^2 \rangle_{\text{ea}} \approx \langle |\Delta V_a(\gamma_{s,R} = 0)|^2 \rangle_{\text{ea}} \times \begin{cases} 1 - \frac{3}{2} \gamma_{s,R} & d = 1, \\ 1 - 2 \gamma_{s,R} & d = 2. \end{cases} \quad (5.31)$$

5.4.2.4 The Effects of Anisotropy

We have seen that the refractive noise for a one-dimensional scattering geometry exceeds that of a two-dimensional scattering geometry by a factor of $\sim \mathcal{B}/r_0$. This significant increase on long baselines suggests that anisotropy in a two-dimensional screen may strongly influence the resulting refractive noise. We will now demonstrate that this suggestion is indeed the case.

For simplicity, we will assume that the source emission is pointlike. Then, consider an anisotropic structure function $D_{\phi,A}$ determined by the coordinate transformation $\{x \rightarrow A_x x, y \rightarrow A_y y\}$ on a corresponding isotropic structure function D_ϕ . The ensemble-averaged visibility then becomes

$$\begin{aligned}\langle V(b_x) \rangle_{\text{ea}} &= e^{-\frac{1}{2}D_\phi\left(\frac{A_x b_x}{1+D/R}\right)}, \\ \langle V(b_y) \rangle_{\text{ea}} &= e^{-\frac{1}{2}D_\phi\left(\frac{A_y b_y}{1+D/R}\right)}.\end{aligned}\tag{5.32}$$

Hence, the anisotropy of the scattering disk is simply $A_x:A_y$, with the parameters $A_{x,y}$ acting to linearly stretch the scattering disk in their respective directions.

Because the noise in the snapshot visibility is still given by Eq. 5.18, the refractive noise satisfies

$$\begin{aligned}\langle |\Delta V_a|^2 \rangle_{\text{ea}} &\approx \frac{1}{(2\pi r_F^2)^2} \int_{\substack{y_2 \lesssim r_0 \\ y_3 \gg r_0}} d^2 \mathbf{y}_{2,3} e^{ir_F^{-2} \mathbf{B} \cdot \mathbf{y}_3} e^{-D_{\phi,A}(\mathbf{y}_2)} \\ &\quad \times \left\{ e^{-\frac{1}{2}[2D_{\phi,A}(\mathbf{y}_3) - D_{\phi,A}(\mathbf{y}_2 + \mathbf{y}_3) - D_{\phi,A}(\mathbf{y}_2 - \mathbf{y}_3)]} - 1 \right\} \\ &= \frac{1}{(2\pi r_F^2)^2} \frac{1}{A_x^2 A_y^2} \int_{\substack{y_2 \lesssim r_0 \\ y_3 \gg r_0}} d^2 \mathbf{y}'_{2,3} e^{ir_F^{-2} \mathbf{B}' \cdot \mathbf{y}'_3} e^{-D_\phi(y'_2)} \\ &\quad \times \left\{ e^{-\frac{1}{2}[2D_\phi(y'_3) - D_\phi(|\mathbf{y}'_2 + \mathbf{y}'_3|) - D_\phi(|\mathbf{y}'_2 - \mathbf{y}'_3|)]} - 1 \right\},\end{aligned}\tag{5.33}$$

where the primed coordinates are simply scaled by $A_{x,y}$ in the respective directions, and $\mathbf{B}' \equiv \{A_x^{-1} \mathbf{B}_x, A_y^{-1} \mathbf{B}_y\}$. We can immediately evaluate the integral using the

results in §5.4.2.2 derived for an isotropic structure function. For example, if $r_{\text{in}} \ll r_0$, then for a baseline along $\hat{\mathbf{x}}$ we have

$$\begin{aligned} \langle |\Delta V_{\text{a,x}}|^2 \rangle_{\text{ea}} &= 2^{\alpha-2} \frac{\Gamma(\alpha/2 + 1)\Gamma(4/\alpha)}{\Gamma(1 - \alpha/2)} \frac{1}{A_x^2 A_y^2} \left(\frac{r_0}{r_{\text{F}}} \right)^{2(2-\alpha)} \left(\frac{\mathcal{B}_x}{r_0 A_x} \right)^{-\alpha} \\ &= 2^{\alpha-2} \frac{\Gamma(\alpha/2 + 1)\Gamma(4/\alpha)}{\Gamma(1 - \alpha/2)} \left(\frac{A_x}{A_y} \right)^2 \left(\frac{r_0/A_x}{r_{\text{F}}} \right)^{2(2-\alpha)} \left(\frac{\mathcal{B}_x}{r_0/A_x} \right)^{-\alpha}. \end{aligned} \quad (5.34)$$

Observe that if $A_x = A_y \equiv A$, then the noise follows with $r_0 \rightarrow r_0/A$, which mirrors the scaling in the ensemble average. However, along the major/minor axis of an anisotropic scattering disk, the noise is enhanced/reduced – the RMS noise is multiplied by the axial ratio of the scattering disk along the respective axis.

5.4.3 The Distribution of Refractive Noise

We have derived the variance of refractive noise. Yet, to obtain the full distribution of refractive noise, we rely on scattering simulations. These simulations indicate that the refractive noise is approximately a zero-mean complex Gaussian random variable. Consequently, the distribution of $r \equiv |\Delta V_{\text{a}}|$ is close to a Rayleigh distribution:

$$P(r > 0) \approx \frac{2}{\sigma^2} r e^{-\left(\frac{r}{\sigma}\right)^2}, \quad (5.35)$$

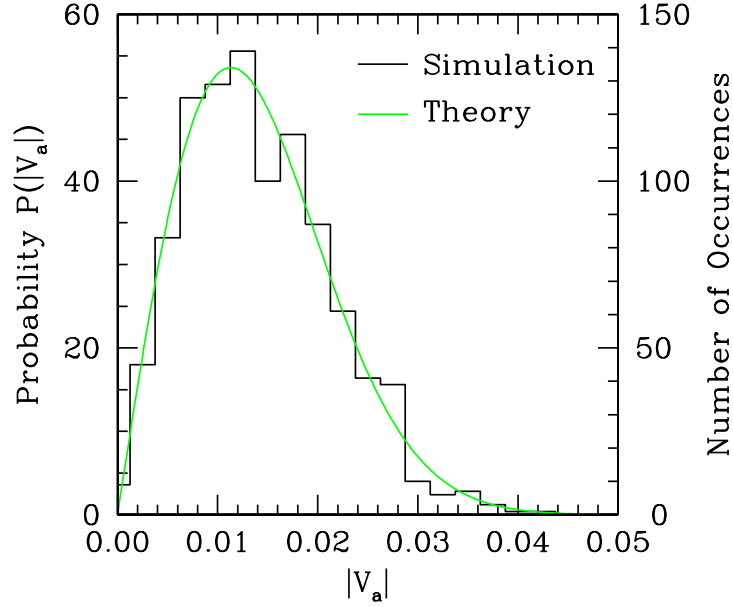


Figure 5.2: The distribution of refractive noise from simulations compared with the expected Rayleigh distribution (Eq. 5.35). Again, the scattering parameters are $\alpha = 5/3$ with a negligible inner scale; samples of the average visibility were calculated on a baseline of $40r_0$. The simulation histogram corresponds to the results from 1000 realizations of a scattering screen determined by 2^{24} correlated phases. In this case, the diffractive noise and the self noise are negligible.

where $\sigma^2 \equiv \langle |\Delta V_a|^2 \rangle_{\text{ea}}$. See Figure 5.2 for a comparison of this PDF with the refractive noise in 1000 iterations of a one-dimensional scattering simulation.

For this distribution, the refractive noise satisfies $\langle |\Delta V_a| \rangle_{\text{ea}} = \frac{\sqrt{\pi}}{2} \langle |\Delta V_a|^2 \rangle_{\text{ea}}^{1/2}$. Moreover, the cumulative distribution function quickly saturates – there is only a $\sim 2\%$ probability of sampling a $\geq 2\sigma$ realization of the noise and a $\sim 0.01\%$ probability of sampling a $\geq 3\sigma$ realization of the noise.

5.5 The Utility of Refractive Noise

Our work is well-suited to several applications. For example, the emission sizes of pulsars are negligible fractions of their scattering disks, so long baseline measurements of pulsars are a rich source of information about the scattering material. The advent of space VLBI with RadioAstron now extends accessible baselines by an order of magnitude – up to the distance of the moon. Since the diffractive scales of pulsars at decimeter wavelengths can be a few thousand kilometers, these ultra-long baselines are excellent for isolating the contribution of refractive substructure in the scattered image.

For all but a few of the most strongly scattered pulsars (such as B1641-45 and the Vela pulsar), the inner scale of the turbulence is probably significantly smaller than the phase coherence length. In this case, three parameters affect the refractive noise: the power-law index α , the fractional distance to the scattering material, and the anisotropy of the scattering disk. Of these, the refractive noise is most sensitive to anisotropy and α , and observations at a range of baselines could potentially determine both.

Another intriguing target is Sgr A*, for which refractive noise might effectively probe the emission size. Indeed, its angular broadening suggests considerable evolution in the intrinsic size at millimeter wavelengths, perhaps from stratified emission within the accretion flow (Doeleman et al., 2001; Shen et al., 2005; Doe-

man et al., 2008). At longer wavelengths, the anisotropic scattering disk quickly dominates the observed size. Also, because of the hyperstrong scattering near the galactic center, the inner scale of the turbulence may significantly exceed the phase coherence length at these wavelengths (Lazio & Cordes, 1998). For $\alpha = 5/3$ and $r_{\text{in}} = 100r_0$, the RMS variations of the average visibility would be doubled relative to those of a source with negligible inner scale, for example. Moreover, although V_{ea} is negligible on long baselines, the refractive noise would remain a valuable probe of source structure and could reflect intrinsic variations in source structure on shorter timescales than the refractive timescale. Over longer timescales, the PDF of noise would represent the cumulative effects of refractive variations (as in §5.4.3) and intrinsic source variations, and could still distinguish them.

Chapter 6

Optimal Correlation Estimators for Quantized Signals

In this chapter, we shift our focus and instead consider how to maximally utilize signal information from an instrumental perspective.¹ Here, the typical limiting factor is the aggressive *quantization* of measured voltages – a process that simply replaces a measured voltage $V \in \mathbb{R}$ by one of a finite number of possible quantization states. For example, a one-bit quantization scheme maps each voltage to its sign, while a two-bit quantization scheme also encodes whether $|V|$ is above or below a predetermined threshold. These two possibilities describe the majority of currently implemented quantization schemes. Indeed, the ability to recover the spectrum or cross-spectrum of a signal with high efficiency even after reducing each sample to only its sign is quite remarkable.

The Nobel laureate John Hasbrouck Van Vleck conducted the first investigations of one-bit correlation as part of a radar jamming project in the Second World War (Van Vleck & Middleton, 1966). The results were declassified after

¹This chapter is adapted from Johnson et al. (2013a).

the War and then quickly applied to the problem of estimating the spectra of digitized signals, especially in radio astronomy (e.g. Faran & Hills, 1952; Weinreb, 1963). Many of the considerations remain relevant – even for next-generation phased arrays, such as the Square-Kilometer Array, the cost of signal transmission necessitates low-bit schemes (Dewdney et al., 2009). Moreover, the application of correlation estimators for quantized signals extends far beyond radio astronomy. An mathematically equivalent situation, for example, arises in a correlation analysis of responses to a multiple-choice survey.

Traditional methods for estimating the correlation after quantization rely on the sample covariance, as historically dictated by cost and hardware constraints. Perhaps surprisingly, the efficiency of this procedure has never been thoroughly analyzed. Hence, in this chapter, we will demonstrate that this scheme achieves the minimum noise of *any* unbiased correlation estimator, if the correlation is small.

Yet, when the correlation is large, this traditional estimator performs quite poorly and exhibits rather paradoxical features. For instance, the correlation noise *increases* with the number of quantization levels. To amend these deficiencies, we derive a general strategy, based on a maximum-likelihood criterion, that achieves optimal performance regardless of the number of bits or the correlation. We demonstrate that this strategy is equivalent to conventional estimators for one-

bit quantization. Applying this strategy will maximize the signal-to-noise and minimize the distortion in applications that utilize multi-bit quantization schemes.

6.1 Introduction

Because astrophysical sources emit Gaussian noise, the information in astrophysical observations lies in signal covariances. These are familiar as power spectra and cross spectra (see, for example, Thompson et al., 2001). The estimation of these covariances is subject to bias and noise, and techniques to minimize both are therefore fundamental to radio astronomy.

This estimation is complicated by the typically aggressive quantization of the received signal. Even for next-generation phased arrays, such as the Square-Kilometer Array, the cost of signal transmission necessitates low-bit quantization (Dewdney et al., 2009). This procedure distorts the spectrum but preserves much of the underlying statistical information. In fact, several authors have noted the ability of quantization to *improve* estimates of correlation $\rho \in [-1, 1]$, especially for strong correlation $|\rho| \rightarrow 1$ (Gwinn, 2004). Indeed, Cole (1968) found that the standard two-level correlation scheme has lower noise than four- and six-level schemes in this limit, and that all of these estimates have lower noise than the correlation estimates for unquantized signals. We demonstrate that this paradoxical behavior arises from two causes: comparisons with unquantized correlation estimates are incomplete, and typical quantization schemes are not optimal.

To amend these deficiencies, we present a correlation estimator for unquantized data that is appropriately suited to define a quantization efficiency, and we derive optimal correlation estimators for quantized signals via a maximum-likelihood criterion. With the recent advent of digital correlators in radio astronomy, such as DiFX (Deller et al., 2007), implementing these techniques is straightforward.

6.1.1 Terminology and Notation

In spite of the many treatments of quantized correlation, no standard terminology has been adopted, so we first outline some basic assumptions and definitions. Throughout this work, we use $\{x_i, y_i\}$ to designate sets of pairs independently drawn from a zero-mean bivariate Gaussian distribution. For simplicity, we will assume that the standard deviations σ_x and σ_y are unity.

We denote ensemble averages by unsubscripted angular brackets $\langle \dots \rangle$. We will make use of the *correlation* $\rho \equiv \langle xy \rangle / (\sigma_x \sigma_y)$ and the *covariance* $\langle xy \rangle$.

We denote finite averages, over N sampled points, by subscripted angular brackets $\langle \dots \rangle_N$. For example, we frequently use the *sample covariance* $r_\infty \equiv \langle xy \rangle_N = N^{-1} \sum_{i=1}^N x_i y_i$. We also use this terminology to refer to an average product after quantization. Because most applications of correlation in radio astronomy involve many samples N , we focus on the large- N regime.

Our work focuses on estimators of ρ , given a set of N samples $\{x_i, y_i\}$, possibly after quantization. We use the variable r , with subscripted identifiers, to indicate

such estimators. Finally, we generically use $P(\dots)$ to denote a probability density function (PDF) with respect to the given variables and parameters.

6.1.2 Relation to Previous Work

Previous analyses of quantized correlation have assumed that the correlation should be estimated via a form of sample covariance for the quantized signals; they have then optimized the performance of the correlation by choosing an appropriate quantization scheme. Furthermore, these efforts generally focus on the small correlation regime: $|\rho| \ll 1$.

For example, Jenet & Anderson (1998) provide an approximate prescription for correcting the bias from quantization in sample covariance. However, this prescription still suffers from severely sub-optimal performance when $\rho \neq 0$, in terms of the noise.

In contrast, we provide a new mechanism for estimating correlation and demonstrate that it provides the lowest RMS error of *any* post-quantization correlation strategy for a large number of samples. We also demonstrate this this strategy is equivalent to traditional approaches as $\rho \rightarrow 0$, and we give a rigorous justification for the optimal quantization weights that are typically quoted.

6.1.3 Outline of Chapter

In §6.2, we briefly review the basic mathematical framework of parameter estimation theory, and we define the sense in which a particular strategy can be “optimal.” Then, in §6.3, we consider the case of unquantized signals and present the corresponding optimal estimators for correlation. Next, in §6.4, we summarize the details of the quantization procedure, outline the traditional correlation estimators via sample covariance, and derive the maximum-likelihood estimate of correlation for quantized signals. In §6.5, we give specific examples for common quantization schemes, and compare the performance of the maximum-likelihood estimate to that of traditional estimates. Then, in §6.6, we demonstrate the critical property that traditional correlation schemes are optimal for small $|\rho|$. Finally, in §6.7, we summarize our findings and discuss the possibilities for implementation.

6.2 Mathematical Background

We begin by reviewing some essential concepts and terminology in parameter estimation theory. For a comprehensive discussion of these ideas with a rigorous description of the assumptions and constraints, see Kendall & Stuart (1979) or Lehmann & Casella (1998).

6.2.1 Optimal Estimators and Maximum Likelihood

We first ascribe a precise meaning to the term “optimal” estimator. For this purpose, we must consider both the bias and noise in an estimator. We seek estimates of correlation that converge to the exact correlation as $N \rightarrow \infty$; such estimates are said to be *consistent*. We refer to a consistent estimator with the minimum noise (i.e. the minimum mean squared error) as the optimal estimator.

If the parameters to be estimated correspond to a known class of distributions, then a particularly simple estimator can be defined. Namely, consider a set of observations \mathbf{x} drawn from a distribution that is specified by a set of parameters $\boldsymbol{\theta}_0$. One parameter estimation strategy determines the parameters that maximize the likelihood function $\mathcal{L}(\boldsymbol{\theta}|\mathbf{x})$, defined as the probability of sampling \mathbf{x} given the distribution specified by $\boldsymbol{\theta}$. If \mathcal{L} has a unique maximum at some $\hat{\boldsymbol{\theta}}_{\text{ML}}$, then this point is defined to be the *maximum-likelihood estimator* (MLE) of $\boldsymbol{\theta}_0$ for the sampled points \mathbf{x} .

Often, the sample data \mathbf{x} can be greatly reduced to some simplified statistic $\mathbf{T}(\mathbf{x})$, which carries all the information related to the parameters $\boldsymbol{\theta}_0$. In this case, $\mathbf{T}(\mathbf{x})$ is said to be a *sufficient* statistic for $\boldsymbol{\theta}_0$. For example, if samples are drawn from a normal distribution with known variance but unknown mean, then the sample mean is a sufficient statistic for the mean. The *factorization criterion* states that a necessary and sufficient condition for $\mathbf{T}(\mathbf{x})$ to be sufficient for a family

of distributions parametrized by $\boldsymbol{\theta}_0$ is that there exist non-negative functions g and h such that $P(\mathbf{x}; \boldsymbol{\theta}_0) = g[\mathbf{T}(\mathbf{x}); \boldsymbol{\theta}_0]h(\mathbf{x})$.

Under weak regularity conditions, the likelihood function also determines the minimum noise that *any* unbiased estimator can achieve. This minimum, the Cramér-Rao bound (CRB), can be expressed in terms of derivatives of \mathcal{L} . For example, the minimum variance of any unbiased estimator $\hat{\theta}$ of a single parameter θ_0 is the inverse of the *Fisher information*, and can be written

$$\langle \delta\hat{\theta}^2 \rangle \geq \left\langle \left(\left. \frac{\partial \ln \mathcal{L}(\mathbf{x}; \theta)}{\partial \theta} \right|_{\theta=\theta_0} \right)^2 \right\rangle^{-1} \equiv \delta\hat{\theta}_{\text{CR}}^2. \quad (6.1)$$

Here, $\langle \dots \rangle$ denotes an ensemble average over sets of measurements \mathbf{x} . An unbiased estimator with noise that matches the CRB is said to be *efficient*.

Under general conditions, the MLE is both consistent and asymptotically (as $N \rightarrow \infty$) efficient. In the present work, we present the MLE of correlation for both unquantized and quantized signals, and we compare these correlation strategies with traditional schemes.

6.2.2 Distribution of Correlated Gaussian Variables

Astrophysical observations measure zero-mean, Gaussian noise. Under rather broad assumptions, pairs of such samples $\{x, y\}$ are drawn from a bivariate Gaussian distribution. In addition to the respective standard deviations, $\sigma_x \equiv \sqrt{\langle x^2 \rangle}$ and $\sigma_y \equiv \sqrt{\langle y^2 \rangle}$, this distribution depends on the correlation $\rho \equiv \langle xy \rangle / (\sigma_x \sigma_y) \in$

$[-1, 1]$. Because our present emphasis is correlation, we assume that $\sigma_x = \sigma_y = 1$, in which case the PDF is given by

$$P(x, y; \rho) = \frac{1}{2\pi\sqrt{1-\rho^2}} \exp\left[-\frac{x^2 + y^2 - 2\rho xy}{2(1-\rho^2)}\right]. \quad (6.2)$$

For small $|\rho|$, this distribution takes the following approximate form:

$$P(x, y; \rho) \approx \frac{1}{2\pi} (1 + \rho xy) e^{-\frac{1}{2}(x^2+y^2)}. \quad (6.3)$$

See Chapter 8 of Thompson et al. (2001) (hereafter TMS) for some additional representations and discussion.

6.3 Correlation Estimators for Unquantized Signals

We now analyze several correlation estimators for unquantized signals. These estimators serve two relevant purposes: they provide a point of reference to ascribe an efficiency to a quantization scheme, and they suggest closed-form strategies for correlation estimates of quantized signals that have a large number of bits.

First, in §6.3.1, we consider the estimate of correlation via sample covariance, denoted r_∞ . Next, in §6.3.2, we present Pearson's estimate of correlation, r_p , which serves as the optimal estimator when no information about the signal is known. Last, in §6.3.3, we give details of the MLE of correlation when the signal

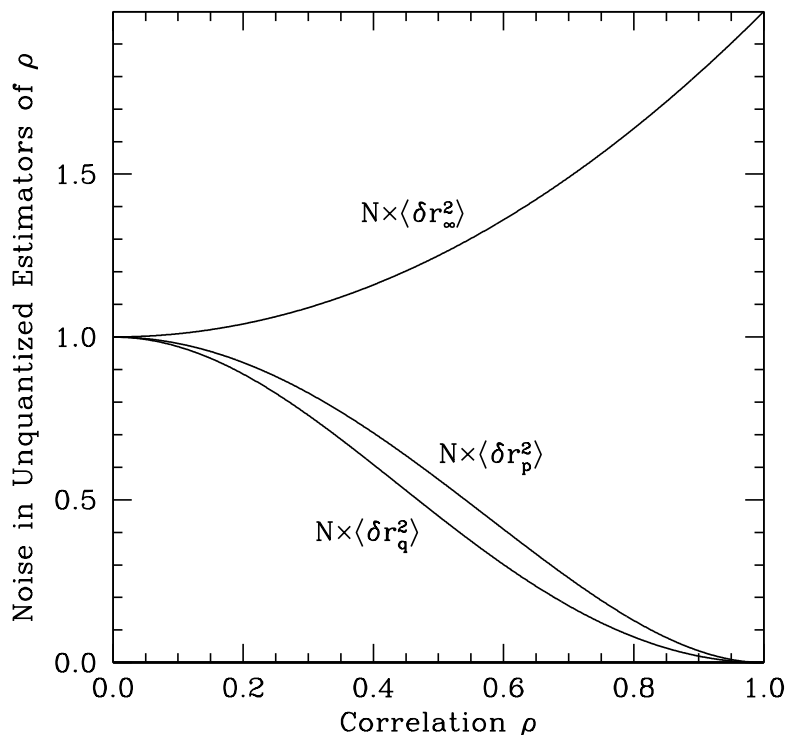


Figure 6.1: Asymptotic noise in estimators r_∞ , r_p , and r_q of ρ for unquantized signals. Because the noise is a symmetric function of ρ , only the positive values are shown.

variances are known, which we denote r_q . Figure 6.1 compares the asymptotic noise in these three estimates, as given in the following sections.

6.3.1 Correlation via Sample Covariance: r_∞

The simplest estimate of correlation follows from the relationship between correlation and covariance. Namely, suppose that the means $\{\mu_x, \mu_y\}$ and standard deviations $\{\sigma_x, \sigma_y\}$ of the signals x_i and y_i are known. In this case, the signals may be standardized to have zero mean and unit variance. Their covariance is then equal to their correlation: $\langle xy \rangle = \rho$. This correspondence immediately suggests a simple estimator for the correlation: $r_\infty \equiv \langle xy \rangle_N = N^{-1} \sum_{i=1}^N x_i y_i$.

This estimator is unbiased and consistent but has large variance: $N\langle\delta r_\infty^2\rangle \equiv N\langle(r - \rho)^2\rangle = (1 + \rho^2)$ (TMS; Eq. 8.13). This equation highlights a peculiar feature: r_∞ is the noisiest when the correlation is *strongest*.

6.3.2 Optimal Correlation: r_p

Many researchers have studied improved estimators of correlation (see Hotelling (1953) and Anderson (1996) for interesting perspectives). The most common estimator is known as ‘‘Pearson’s r ’’ and is given by

$$r_p \equiv \frac{\langle(x - \langle x \rangle_N)(y - \langle y \rangle_N)\rangle_N}{\sqrt{\langle(x - \langle x \rangle_N)^2\rangle_N \langle(y - \langle y \rangle_N)^2\rangle_N}}. \quad (6.4)$$

In addition to being unbiased and consistent, r_p is asymptotically efficient. The asymptotic noise can be derived using the Fisher transformation (Fisher, 1915, 1921): $\lim_{N \rightarrow \infty} N\langle\delta r_p^2\rangle = (1 - \rho^2)^2$, which is indeed the CRB.

Note that substituting the exact means and variances into r_p returns the original estimate r_∞ and, remarkably, *decreases* the quality of the estimate. As a simple example, three randomly generated samples with correlation $\rho = 0.999$ are $\{x_i\} = \{0.998, 1.712, -0.992\}$, $\{y_i\} = \{1.01, 2.01, -0.980\}$. In this case, we obtain estimates $r_\infty = 1.81$, $r_p = 0.997$. Indeed, for perfect correlation, $\delta r_p^2 = 0$, whereas $\delta r_\infty^2 = 2/N$. Pearson’s estimate accounts for the sample variance, which contributes much of the noise in r_∞ . However, for a small correlation, $\rho \rightarrow 0$, the noise in r_∞ and r_p is identical (we further discuss this feature in §6.6).

Hence, when the correlation is large, simply averaging products poorly approximates the correlation relative to other schemes. Even if the exact variance is known, the sample variance must still be incorporated to optimally estimate the correlation.

6.3.3 Optimal Correlation with Known Signal Variance:

$$r_q$$

Nevertheless, an exact knowledge of the variance can be used to effectively improve the estimate of correlation. In fact, this knowledge is often implicit in radio astronomical analyses. For example, automatic gain control usually sets the variances $\langle x^2 \rangle = \langle y^2 \rangle = 1$, and quantization schemes use the “known” variance to determine the appropriate level settings. Errors in the signal estimate are then a source of both bias and noise, so for non-stationary signals such as pulsars, the quantization weights must be dynamically adjusted (see Jenet & Anderson, 1998). For a more complete discussion of quantization noise, see Gwinn (2004) and Gwinn (2006).

More generally, whenever the timescale of variation of ρ is shorter than that of variation in the standard deviation σ of x and y , there will be improved measures of correlation.

For example, if the standard deviations of x and y are known to be unity, then the MLE of correlation, denoted r_q , is determined by the real solution of

$$r_\infty (1 + r_q^2) - r_q (\langle x^2 \rangle_N + \langle y^2 \rangle_N - (1 - r_q^2)) = 0. \quad (6.5)$$

In §6.8, we derive this result, give an approximate form for r_q , and demonstrate that the noise in this estimate achieves the CRB as $N \rightarrow \infty$, as expected for an MLE: $\lim_{N \rightarrow \infty} N \langle \delta r_q^2 \rangle = (1 - \rho^2)^2 / (1 + \rho^2)$. The advantage of r_q relative to r_p increases with $|\rho|$, and gives a factor of two improvement in the estimator variance at high correlation. Moreover, the bias in r_q is $\mathcal{O}(N^{-2})$.

6.4 Correlation Estimators for Quantized Signals

In practice, data are digitized, which involves quantization according to a prescribed scheme. The merit of the quantization, reduction of data volume, must be carefully weighed against its drawback, degraded signal information.

We first review the details of quantization and the traditional estimators of correlation, which rely on the sample covariance after quantization. We then derive the MLEs of correlation for arbitrary quantization schemes and give expressions for the noise in these estimators.

6.4.1 The Quantization Transfer Function

The process of quantization maps each element in a time series $x_i \in \mathbb{R}$ to a set of $L = 2^b$ discrete values: $x_i \mapsto \hat{x}_{L,i}$, where b is the number of bits in the quantization scheme. This transfer function involves $L - 1$ thresholds, which partition \mathbb{R} into L subsets, and L respective weights for these subsets.

6.4.2 Quantized Correlation via Sample Covariance

The traditional correlation estimator for quantized signals matches the form of the continuous covariance estimator, r_∞ , to the quantized signals $\hat{r}_L \equiv \langle \hat{x}_L \hat{y}_L \rangle_N$ (Van Vleck & Middleton, 1966; Cole, 1968; Cooper, 1970; Hagen & Farley, 1973).

In some cases, this result is then appropriately transformed to account for bias.

This correlation strategy is optimized through the particular thresholds and weights that determine the transfer function of the quantization.

6.4.3 The MLE of Correlation for Quantized Signals

We now derive the MLE of correlation $r_{L,ML}$ for quantized signals, which is both consistent and asymptotically efficient. In particular, the likelihood function \mathcal{L} for a set of N independent and identically distributed (i.i.d.) pairs of samples $\{\hat{x}_{L,i}, \hat{y}_{L,i}\}$ drawn from a bivariate normal distribution and then quantized in a

scheme with L levels is

$$\begin{aligned}\mathcal{L}(\rho, \sigma | \{\hat{x}_{L,i}, \hat{y}_{L,i}\}) &= \prod_{i=1}^N P(\hat{x}_{L,i}, \hat{y}_{L,i}; \rho, \sigma) \\ \Rightarrow \ln \mathcal{L}(\rho, \sigma | \{\hat{x}_{L,i}, \hat{y}_{L,i}\}) &= \sum_{\ell} \mathcal{N}_{\ell} \ln \mathcal{P}_{\ell}(\rho, \sigma).\end{aligned}\tag{6.6}$$

In this expression, ℓ runs over the L^2 possible quantized pairs $\{\hat{x}_L, \hat{y}_L\}$; \mathcal{N}_{ℓ} is the total number of samples in each such category; and $\mathcal{P}_{\ell}(\rho, \sigma)$ corresponds to the probability of a sampled pair $\{\hat{x}_L, \hat{y}_L\}$ falling in that category.

To determine the MLE, this log-likelihood must be maximized with respect to ρ , if σ is assumed to be known, or with respect to ρ and σ , if σ is unknown. Although we have assumed symmetry $\sigma_x = \sigma_y$, the generalization is straightforward.

The MLE thus requires an evaluation of each probability \mathcal{P}_{ℓ} :

$$\mathcal{P}_{\ell} = S_{\ell} \int_{R_{\ell}} dx dy P(x, y; \rho, \sigma).\tag{6.7}$$

In this expression, $P(x, y; \rho, \sigma)$ is given by Eq. 6.2, $R_{\ell} \subset \mathbb{R}^2$ corresponds to the set of unquantized values that map to each quantized state, and $S_{\ell} \in \mathbb{Z}$ is an optional symmetry factor, to account for the symmetry under inversion, $P(\hat{x}_{L,i}, \hat{y}_{L,i}) = P(-\hat{x}_{L,i}, -\hat{y}_{L,i})$, and transposition, $P(\hat{x}_{L,i}, \hat{y}_{L,i}) = P(\hat{y}_{L,i}, \hat{x}_{L,i})$. In a few instances, such as the quadrant integrals that arise in one-bit correlation, Eq. 6.7 has a

simple, closed-form representation. More generally, it can be reduced to a one-dimensional integral of an error function.

Thus, in most cases, the MLE requires minimization over a function that involves one-dimensional numerical integration. However, many strategies can simplify this estimation. For example, if both the number of samples N and quantization bits b are small, then all required solutions can be tabulated. After including the symmetry reductions, the number of distinct correlation possibilities is $N_\ell = 2^{b-1} (1 + 2^{b-1})$. The total number M of partitions of N samples into these categories is then $M = \binom{N+N_\ell-1}{N_\ell-1} \sim N^{N_\ell-1}/(N_\ell-1)!$. If M is prohibitively large, then the N samples can first be partitioned and then the respective correlation estimates averaged to obtain an approximation of the MLE.

6.4.4 Noise in the MLE and the Cramér-Rao Lower Bound

As we have already mentioned, the CRB determines the minimum variance that any unbiased estimator of ρ can achieve. In terms of the likelihood function of §6.4.3, the elements of the 2×2 Fisher information matrix for $\{\rho, \sigma\}$ can be written

$$\begin{aligned} \mathcal{I}_{1,1} &\equiv \left\langle \left(\frac{\partial}{\partial \rho} \sum_{\ell} \mathcal{N}_{\ell} \ln \mathcal{P}_{\ell} \right)^2 \right\rangle = N \sum_{\ell} \frac{\left(\frac{\partial \mathcal{P}_{\ell}}{\partial \rho} \right)^2}{\mathcal{P}_{\ell}}, \\ \mathcal{I}_{1,2} &= N \sum_{\ell} \frac{\left(\frac{\partial \mathcal{P}_{\ell}}{\partial \rho} \right) \left(\frac{\partial \mathcal{P}_{\ell}}{\partial \sigma} \right)}{\mathcal{P}_{\ell}}, \\ \mathcal{I}_{2,2} &= N \sum_{\ell} \frac{\left(\frac{\partial \mathcal{P}_{\ell}}{\partial \sigma} \right)^2}{\mathcal{P}_{\ell}}. \end{aligned} \tag{6.8}$$

If σ is known, then the minimum variance of an unbiased estimator of ρ is $\delta r_{L,\text{CR}}^2 = \mathcal{I}_{1,1}^{-1}$; if σ is unknown, then the minimum variance is $\delta r_{L,\text{CR}}^2 = \mathcal{I}_{2,2} / (\mathcal{I}_{1,1}\mathcal{I}_{2,2} - \mathcal{I}_{1,2}^2)$.

The MLE is asymptotically efficient, so $\langle \delta r_{L,\text{ML}}^2 \rangle \rightarrow \delta r_{L,\text{CR}}^2$ as $N \rightarrow \infty$.

These expressions can be easily generalized to cases where the variances σ_x, σ_y are not necessarily equal, the means μ_x, μ_y are unknown, and so on. However, these broader conditions do not change $\delta r_{L,\text{CR}}^2$, as can be readily verified. Hence, for clarity, we emphasize estimators of ρ in the two prototypical cases: σ known and σ unknown.

6.5 Examples

6.5.1 One-bit Quantization

In the standard one-bit, or two-level, quantization scheme, each sample is reduced to one “sign” bit: $x \mapsto \hat{x}_2 \equiv \text{sign}(x)$. Because the sample error for the signal variance incurs the bulk of the noise in r_∞ , quantization actually *improves* upon the estimate of r_∞ in some cases.

Explicitly, we have $r_2 \equiv \langle \hat{x}\hat{y} \rangle_N$. However, this estimate is biased: $\langle r_2 \rangle = 2\pi^{-1} \sin^{-1} \rho$. The standard Van Vleck clipping correction, denoted $r_{2,\text{V}}$, improves the bias to $\mathcal{O}(1/N)$ by simply inverting this relationship (Van Vleck & Middleton,

1966):

$$r_{2,V} \equiv \sin\left(\frac{\pi}{2}r_2\right). \quad (6.9)$$

In fact, $r_{2,V}$ gives precisely the MLE. To see this, note that the quantized products, $\hat{x}\hat{y}$, have probability $P(\pm 1) = \frac{1}{2} \pm \frac{1}{\pi} \arcsin \rho$.² Minimizing the log-likelihood (Eq. 6.6) with respect to ρ gives that $r_{2,ML} = r_{2,V}$.

Because $r_{2,V}$ is the MLE, the noise for large N is given by the CRB. Substituting $P(\pm 1)$ into Eq. 6.8 gives

$$N\delta r_{2,CR}^2 = \left[\left(\frac{\pi}{2}\right)^2 - (\arcsin \rho)^2 \right] (1 - \rho^2). \quad (6.10)$$

We can easily verify that the noise in $r_{2,V}$ actually achieves this lower bound. Namely, the correlation estimate r_2 is a one-dimensional random walk with N steps of length $\pm 1/N$, distributed according to $P(\pm 1)$. For large N , the central limit theorem gives that r_2 follows a Gaussian distribution with mean $2\pi^{-1} \arcsin \rho$ and variance $N^{-1} \left[1 - (2\pi^{-1} \arcsin \rho)^2 \right]$. In this limit, we obtain

$$\begin{aligned} \langle r_{2,V}^2 \rangle &= \frac{1}{2} \left\{ 1 - (1 - 2\rho^2) \exp\left[\frac{4(\arcsin \rho)^2 - \pi^2}{2N}\right] \right\} \\ \Rightarrow N \langle \delta r_{2,V}^2 \rangle &\approx \left[\left(\frac{\pi}{2}\right)^2 - (\arcsin \rho)^2 \right] (1 - \rho^2), \end{aligned} \quad (6.11)$$

²In Appendix A we give a derivation and extension of this result.

which is identical to the CRB.

The most striking improvement of $r_{2,V}$ relative to r_∞ occurs as $\rho \rightarrow \pm 1$; in this limit, the one-bit correlation has no noise, while $\langle \delta r_\infty^2 \rangle = 2/N$.

6.5.2 Two-Bit Quantization

Perhaps the most common quantization strategy replaces each sample by a pair of bits representing sign and magnitude. The (non-zero) thresholds $\pm v_0$ are fixed at some level relative to the estimated RMS signal voltage σ in a way that minimizes the expected RMS noise in the subsequent correlation estimates. The resulting four levels are then assigned weights $\hat{x}_2 \in \{\pm 1, \pm n\}$, where n is also chosen to minimize the noise. In terms of the mean quantized product $r_4 \equiv \langle \hat{x}_4 \hat{y}_4 \rangle_N$, one obtains the correlation estimate (TMS; Eq. 8.43)

$$r_{4,v} = \frac{r_4}{\Phi + n^2(1 - \Phi)}, \quad \Phi \equiv \text{erf} \left(\frac{v_0}{\sigma\sqrt{2}} \right). \quad (6.12)$$

This estimate of correlation, which already assumes exact knowledge of σ , retains a significant ($\sim 10\%$) bias to high $|\rho|$ (see Figure 1 of Jenet & Anderson (1998)). If $|\rho| \lesssim 0.8$, for instance, then the appropriate correction is simply a constant scaling factor (TMS; Eq. 8.45):

$$r_{4,v} \approx \left\{ \frac{\pi [\Phi + n^2(1 - \Phi)]}{2 [(n - 1)E + 1]^2} \right\} r_{4,v}, \quad E \equiv e^{-\frac{1}{2} \left(\frac{v_0}{\sigma} \right)^2}. \quad (6.13)$$

For additional details and a complete formulation to remove the bias, see Gwinn (2004). Here, we use the “V” subscript to draw analogy with the Van Vleck correction for one-bit correlation. Namely, this estimate calculates the sample covariance after quantization and then performs a bias correction according to the estimated correlation. The remaining bias is $\mathcal{O}(1/N)$.

Researchers then optimize this two-bit correlation scheme by a particular choice of thresholds and weights: $v_0 = 0.9815$, $n = 3.3359$. However, unlike one-bit correlation, the bias-corrected quantized product $r_{4,V}$ is *not* the optimal estimator of correlation for quantized data. In particular, $r_{4,V}$ even reflects the disturbing feature of the continuous estimate r_∞ that the noise tends to increase with $|\rho|$. Hence, high correlations present the paradoxical situation in which traditional estimates $\{r_\infty, r_{4,V}, r_{2,V}\}$ perform *better* as the number of bits is *reduced*.

This troubling evolution merely reflects the incompleteness of these correlation estimates. Figure 6.2 compares the noise in $r_{4,V}$ to the noise in the MLE, both when σ is known and unknown. Each MLE has negligible bias and noise that reflects the behavior seen in the corresponding unquantized MLE, r_p or r_q . The noise is always lower than that of $r_{2,V}$ and approaches zero as $|\rho| \rightarrow 1$. We therefore resolve the puzzling evolution of correlation noise after quantization.

The only remaining barrier is the computational difficulty of implementation. However, for small values of N , the maximum-likelihood solutions may be tabulated prior to calculation; the required number of tabulated values is

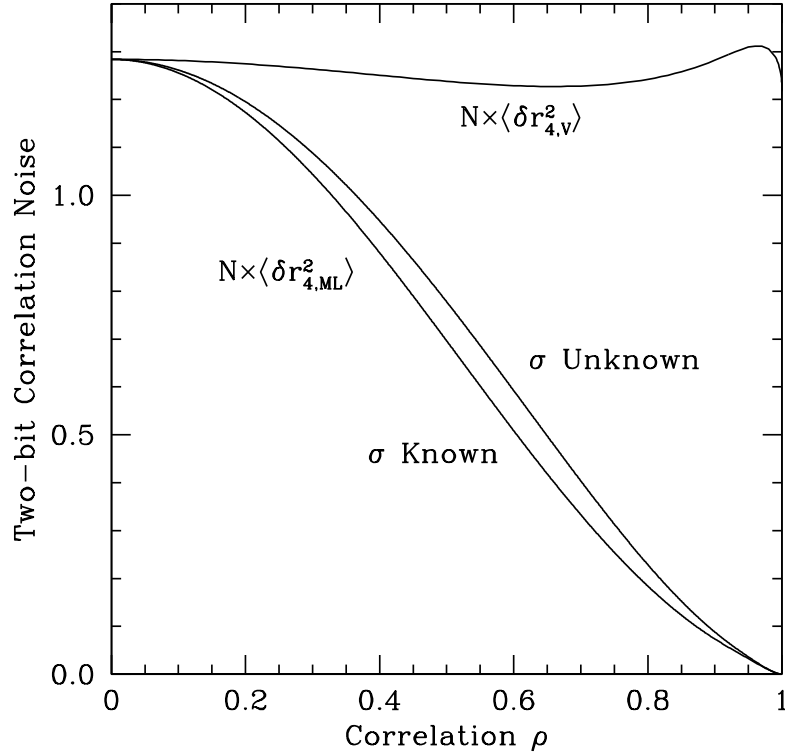


Figure 6.2: Noise in estimates of correlation for signals quantized with two bits. The chosen levels ($v_0 = 0.9815$) and weights ($n = 3.3359$) are optimal as $|\rho| \rightarrow 0$. The upper curve gives the noise in the traditional estimator via sample covariance, as derived in Gwinn (2004), whereas the lower curves give the noise in the MLEs with and without knowledge of σ .

$M = \binom{N+5}{5} \sim N^5/5!$ (see §6.4.3). Alternatively, one can first partition the N samples, then calculate the MLE of correlation for each subset via tabulation, and finally average the results. We defer a comprehensive treatment of these implementation strategies to a future work.

6.5.3 Many-Bit Quantization

Modern instrumentation now permits the storage of baseband data with many-bit quantization schemes. In this case, the noise in the MLE of correlation rapidly

approaches that in the corresponding unquantized limit, r_p or r_q (see Figure 6.3). In such cases, these estimators for unquantized signals provide excellent approximations of the quantized MLEs, and the primary concerns are the influence of RFI and instrumental limitations (TMS). Furthermore, although low-bit quantization schemes are quite robust to impulsive RFI, estimates such as r_p are not, so alternative quantization schemes that are robust at the expense of increased noise may be preferred (Fridman, 2009).

We now consider the incurred bias when approximating the quantized MLE by r_p . Specifically, consider a high-bit scheme with L levels, thresholds in multiples of $\pm v_0$, and quantization weights \hat{x} that are the average values of their respective preimages. We denote the corresponding estimator $r_{L,p}$. Then, if the highest thresholds extend far into the tail of the distribution, the bias after quantization is approximately

$$\langle \delta r_{L,p} \rangle \approx -\frac{1}{12} \left(\frac{v_0}{\sigma} \right)^2 \rho. \quad (6.14)$$

For more general expressions, which include the effects of the finite outer thresholds, consult the discussion in §8.3 of TMS. While correcting the bias is straightforward, even for a low number of bits, this strategy is ineffective for low-bit schemes because $r_{L,p}$ is not a sufficient statistic for ρ .

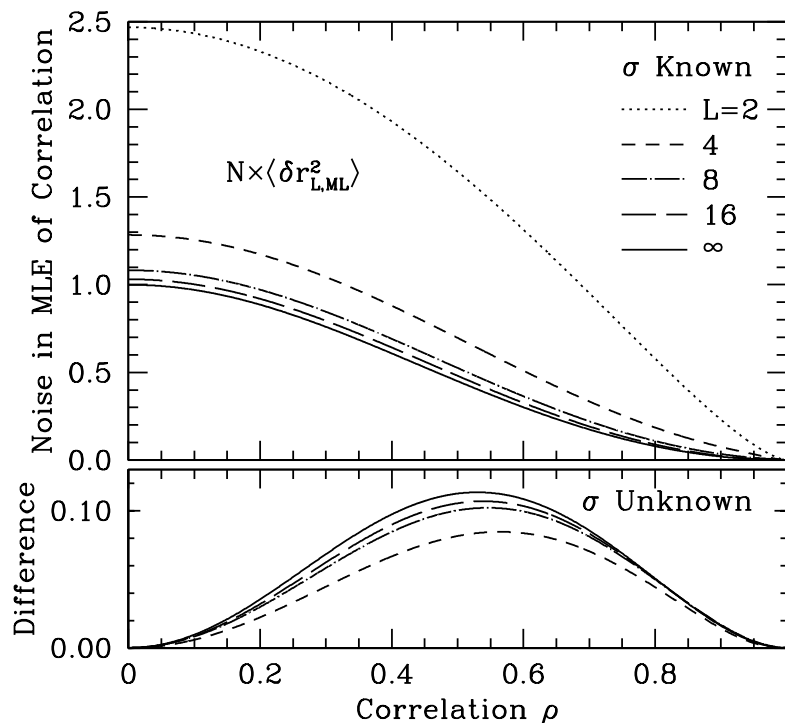


Figure 6.3: Noise in the MLE of correlation for quantized signals as a function of correlation for various quantization levels. The upper panel shows the noise when σ is known, and the lower panel shows the additional noise when σ is unknown. For simplicity, we set the $(L - 1)$ quantization thresholds in multiples of $\pm 4/L$. Observe that the reduction in noise provided by knowledge of σ becomes more pronounced as the number of levels is *increased*. For example, knowledge of σ provides no improvement for one-bit correlation.

6.6 Reductions for Small Correlation

Although the MLE of correlation decreases the noise for large $|\rho|$, it exhibits identical noise to traditional estimators at small $|\rho|$. Furthermore, in this limit, knowledge of σ does not reduce the noise. These features both arise from the form of the bivariate Gaussian PDF in this limit.

For example, consider the estimation of correlation for unquantized signals when $\sigma_x = \sigma_y = 1$ is known. Then, if $|\rho| \ll 1$, the joint PDF of N independently-

drawn pairs of correlated random variables $\{x_i, y_i\}$ is (see Eq. 6.3)

$$P(\{x_i, y_i\}; \rho) \approx \frac{1}{(2\pi)^N} (1 + N\rho\langle xy \rangle_N) e^{-\frac{N}{2}(\langle x^2 \rangle_N + \langle y^2 \rangle_N)}. \quad (6.15)$$

Thus, from the factorization criterion, $r_\infty \equiv \langle xy \rangle_N$ is a sufficient statistic for ρ , and so we expect the asymptotic noise in r_∞ to match that of r_q as $\rho \rightarrow 0$.

Likewise, consider the joint distribution of the samples after quantization into L weighted levels. In this case, we require the set of quantized probabilities

$$\mathcal{P}_\ell \approx \frac{1}{2\pi} \int_{R_\ell} dx dy (1 + \rho xy) e^{-\frac{1}{2}(x^2 + y^2)} \equiv \alpha_\ell + \beta_\ell \rho. \quad (6.16)$$

The joint PDF of the quantized samples is then

$$\begin{aligned} P(\{\hat{x}_{L,i}, \hat{y}_{L,i}\}; \rho) &= \prod_\ell \mathcal{P}_\ell^{\mathcal{N}_\ell} \\ &\approx \left(\prod_\ell \alpha_\ell^{\mathcal{N}_\ell} \right) \left(1 + \rho \sum_\ell \mathcal{N}_\ell \frac{\beta_\ell}{\alpha_\ell} \right). \end{aligned} \quad (6.17)$$

Hence, for small $|\rho|$, the factorization criterion gives that $\langle w(\hat{x}, \hat{y}) \rangle$ is a sufficient statistic for ρ , if the weight function is determined by

$$\begin{aligned} w(\hat{x}, \hat{y}) &= \frac{\int_{R_\ell} dx dy xy e^{-\frac{1}{2}(x^2 + y^2)}}{\int_{R_\ell} dx dy e^{-\frac{1}{2}(x^2 + y^2)}} \\ &= \left[\frac{\int_{R_{\ell,x}} dx x e^{-\frac{x^2}{2}}}{\int_{R_{\ell,x}} dx e^{-\frac{x^2}{2}}} \right] \left[\frac{\int_{R_{\ell,y}} dy y e^{-\frac{y^2}{2}}}{\int_{R_{\ell,y}} dy e^{-\frac{y^2}{2}}} \right], \end{aligned} \quad (6.18)$$

where $R_{\ell,x} \subset \mathbb{R}$ defines the range of values spanned by each quantized level.

Moreover, the final factorization in Eq. 6.18 demonstrates that, by assigning an appropriate weight to each quantization level: $w(\hat{x}, \hat{y}) = \hat{x}\hat{y}$, the sample covariance is a sufficient statistic for ρ and will achieve optimal noise performance as $|\rho| \rightarrow 0$.

The asymptotic noise in this limit is then the CRB:

$$\delta r_{L,\text{CRB}}^2 \Big|_{\rho=0} = \frac{2\pi}{N} \left\{ \sum_{\ell} \frac{\left[\int_{R_{\ell}} dx dy xy e^{-\frac{1}{2}(x^2+y^2)} \right]^2}{\int_{R_{\ell}} dx dy e^{-\frac{1}{2}(x^2+y^2)}} \right\}^{-1}. \quad (6.19)$$

Minimizing this equation yields the optimal thresholds. Then, Eq. 6.18 immediately determines the optimal weights. Observe that these weights are slightly different than those of some previous works, such as Jenet & Anderson (1998), but match the ratios of traditional quantization schemes, such as $n = 3.336$ when $v_0 = 0.982$ for two-bit correlation.

Finally, $\mathcal{I}_{1,2} \rightarrow 0$ as $\rho \rightarrow 0$. This result follows easily by substituting \mathcal{P}_{ℓ} and its derivatives into Eq. 6.8. Hence, the CRB is unchanged by knowledge of σ in this limit.

6.7 Summary

We have explored the paradoxical scaling of noise in traditional estimates of correlation for quantized signals. In particular, we have shown that the decrease in noise that quantization affords is a result of an incomplete comparison with unquan-

tized correlation schemes and of sub-optimal correlation strategies for quantized signals.

We have derived the MLE of correlation, both with and without knowledge of the signal variance and quantization, and we have compared these estimates to traditional schemes. The MLE has negligible bias, lower noise, and is asymptotically efficient: for a large number of samples, no other unbiased scheme will achieve lower noise. We have also derived simple expressions for this asymptotic noise (the CRB). While the MLE gives the familiar Van-Vleck corrected sample covariance for one-bit quantization, it differs significantly from current correlation strategies for all other cases.

Nevertheless, traditional correlation schemes are fully optimized in the limit $\rho \rightarrow 0$. Namely, for suitably chosen weights, the sample covariance \hat{r}_L is a sufficient statistic for the correlation ρ , in this limit.

Future detectors, such as the Square-Kilometer Array, that will achieve high signal-to-noise while being limited to a small number of quantization bits, can benefit from these novel correlation strategies to reduce both the distortion and noise introduced by quantization.

6.8 Appendix: MLE for Unquantized Signals with Known Variance

We now summarize the main features of the MLE of correlation for samples $\{x_i, y_i\}$ drawn from a bivariate Gaussian distribution with known means and variances. See Kendall & Stuart (1979) for additional details. For simplicity, we assume that the means are zero and the variances are unity. We also assume that each pair is drawn independently. The likelihood function is then

$$\begin{aligned} \mathcal{L}(\rho|\{x_i, y_i\}) &\equiv \prod_{i=1}^N P(x_i, y_i; \rho, \sigma_x, \sigma_y) \\ &= \frac{1}{(2\pi\sqrt{1-\rho^2})^N} \exp \left[-\frac{1}{2(1-\rho^2)} \sum_{i=1}^N (x_i^2 + y_i^2 - 2\rho x_i y_i) \right]. \end{aligned} \quad (6.20)$$

The condition for the likelihood function to be extremized is

$$r_\infty (1 + \rho^2) - \rho (s_x^2 + s_y^2 - (1 - \rho^2)) = 0, \quad (6.21)$$

where $s_x^2 \equiv \langle x^2 \rangle_N$, $s_y^2 \equiv \langle y^2 \rangle_N$, and $r_\infty \equiv \langle xy \rangle_N$. Hence, the triplet $\{r_\infty, s_x, s_y\}$ is sufficient for ρ . We will denote the appropriate solution to this cubic equation r_q .

To obtain some intuition for this result, let $\epsilon \equiv s_x^2 + s_y^2 - 2$. Then $\langle \epsilon^2 \rangle = 4(1 + \rho^2)/N$. The discriminant of the cubic is

$$\Delta = -4r_\infty^4 + (\epsilon^2 + 20\epsilon - 8) r_\infty^2 - 4(1 + \epsilon)^3. \quad (6.22)$$

If $\Delta < 0$, then the cubic has a single real solution. As a rough rule of thumb, we can simply consider when all terms are negative. Since $\delta\epsilon \approx 2/\sqrt{N}$, we see that there is likely a unique real solution whenever $\epsilon < .39$, or $N \gtrsim 25$.

Although finding this solution is both analytically and numerically straightforward, an approximation is both useful and enlightening:

$$r_q = r_\infty \left[1 - \frac{1}{1 + r_\infty^2} \epsilon + \frac{1 - r_\infty^2}{(1 + r_\infty^2)^3} \epsilon^2 + \mathcal{O}(\epsilon^3) \right]. \quad (6.23)$$

This expansion immediately identifies the appropriate root of the cubic equation. Furthermore, we can determine the asymptotic noise for r_q by expanding Eq. 6.23 for large N :

$$\langle \delta r_q^2 \rangle = \langle \delta r_\infty^2 \rangle + \frac{\rho^2}{(1 + \rho^2)^2} \langle \epsilon^2 \rangle - \frac{2\rho}{1 + \rho^2} \langle \delta r_\infty \epsilon \rangle. \quad (6.24)$$

A straightforward application of Isserlis' Theorem (Isserlis, 1918) gives that $\langle \delta r_\infty^2 \rangle = (1 + \rho^2)/N$, $\langle \epsilon^2 \rangle = 4(1 + \rho^2)/N$, and $\langle \delta r_\infty \epsilon \rangle = 4\rho/N$. Putting everything together,

we obtain

$$\lim_{N \rightarrow \infty} N \langle \delta r_{\text{q}}^2 \rangle = \frac{(1 - \rho^2)^2}{1 + \rho^2}. \quad (6.25)$$

We can easily verify that this result is equal to the CRB:

$$\begin{aligned} \langle \delta r_{\text{CR}}^2 \rangle &= \left\{ N \int_{-\infty}^{\infty} dx dy \frac{\left(\frac{\partial P(x, y; \rho)}{\partial \rho} \right)^2}{P(x, y; \rho)} \right\}^{-1} \\ &= \left\{ \frac{N}{(1 - \rho^2)^4} \int_{-\infty}^{\infty} dx dy [-\rho(1 - \rho^2) - (1 + \rho^2)xy + \rho(x^2 + y^2)]^2 \right. \\ &\quad \left. \times \frac{1}{2\pi\sqrt{1 - \rho^2}} \exp \left[-\frac{(x^2 + y^2 - 2\rho xy)}{2(1 - \rho^2)} \right] \right\}^{-1} \\ &= \frac{1}{N} \frac{(1 - \rho^2)^2}{1 + \rho^2}. \end{aligned} \quad (6.26)$$

Appendices

Appendix A

An Extension and Application of Price's Theorem

A.1 Extending Price's Theorem

Price's Theorem provides a convenient relationship between derivatives of functions that are separable in elements $\{x_1, x_2\}$ drawn from a standardized bivariate Gaussian distribution with correlation $\rho \equiv \langle x_1 x_2 \rangle$ (Price, 1958):

$$\frac{\partial^k \langle f_1(x_1) f_2(x_2) \rangle}{\partial \rho^k} = \left\langle f_1^{(k)}(x_1) f_2^{(k)}(x_2) \right\rangle. \quad (\text{A.1})$$

See Hagen & Farley (1973) or Thompson et al. (2001) for an application of this result to estimate the bias of quantization on covariance.

McMahon (1964) then showed that this result can be generalized to obtain

$$\frac{\partial^k \langle f(x_1, x_2) \rangle}{\partial \rho^k} = \left\langle \frac{\partial^{2k} f(x_1, x_2)}{\partial x_1^k \partial x_2^k} \right\rangle. \quad (\text{A.2})$$

Finally, Pawula (1967) again generalized the result to incorporate more than two random variables. Let $\langle \dots \rangle_\alpha$ denote an expectation where the off-diagonal elements of the covariance matrix $[\rho_{ij}]$ are scaled by α . In this case, he showed that

$$\frac{\partial^k \langle f(x_1, \dots, x_n) \rangle_\alpha}{\partial \alpha^k} = \langle \mathcal{H}^k f(x_1, \dots, x_n) \rangle_\alpha, \quad (\text{A.3})$$

where we have introduced the operator $\mathcal{H} \equiv \sum_{i < j} \rho_{ij} \frac{\partial^2}{\partial x_i \partial x_j}$. For simplicity, we will write $E_\alpha [f] \equiv \langle f(x_1, \dots, x_n) \rangle_\alpha$. Now, if $k = 1$, then Eq. A.3 can be solved to obtain

$$\begin{aligned} E_1 [f] &= E_0 [f] + \int_0^1 d\alpha E_\alpha [\mathcal{H}f] \\ \Rightarrow E_{\alpha_1} [\mathcal{H}f] &= E_0 [\mathcal{H}f] + \int_0^1 E_{\alpha_1 \alpha_2} [\alpha_1 \mathcal{H}^2 f] d\alpha_2. \end{aligned} \quad (\text{A.4})$$

We can now iterate this substitution to obtain a different representation of $E_1[f]$ that is entirely in terms of averages of functions with independent variables:

$$E_1 [f] = \sum_{j=0}^{\infty} \frac{1}{j!} E_0 [\mathcal{H}^j f]. \quad (\text{A.5})$$

In a somewhat more compelling form, we have

$$\langle f \rangle = \langle e^{\mathcal{H}} f \rangle_0. \quad (\text{A.6})$$

Price's theorem and the generalizations by McMahon and Pawula are all trivial applications of this relationship.

A.2 Example: Calculating the Bias in One-Bit Correlation

As a simple example of Eq. A.5, consider the problem of estimating the bias in covariance after one-bit quantization. In this case, we need the four quadrant integrals, which can be written as $f(x_1, x_2) = \theta(t_1 x_1) \theta(t_2 x_2)$, where the $t_i = \pm 1$ define the quadrant. Thus, $\mathcal{H}^j f = t_1 t_2 \rho^j \delta^{(j-1)}(x_1) \delta^{(j-1)}(x_2)$ for $j > 0$. Now, for a single (standardized) Gaussian variable x , the PDF $P(x)$ obeys

$$\left. \frac{d^n}{dx^n} P(x) \right|_{x=0} = \begin{cases} (-1)^{n/2} \frac{(n-1)!!}{\sqrt{2\pi}} & n \text{ even,} \\ 0 & n \text{ odd.} \end{cases} \quad (\text{A.7})$$

Thus, Eq. A.5 gives

$$\begin{aligned} E_1[f] &= \frac{1}{4} + \frac{1}{2\pi} t_1 t_2 \sum_{\substack{j=1 \\ j \text{ odd}}}^{\infty} \frac{((j-2)!!)^2}{j!} \rho^j \\ &= \frac{1}{4} + \frac{1}{2\pi} t_1 t_2 \arcsin(\rho). \end{aligned} \quad (\text{A.8})$$

A.3 Evaluating Quadrant Integrals with Diagrams

Next, consider a slight generalization of the previous problem. Namely, we seek to calculate the expected value of a function $f = \prod_{i=1}^n \theta(t_i x_i)$ when the x_i are

drawn from a multivariate normal distribution with covariance matrix $[\rho_{ij}]$, and $t_i = \pm 1$. In this case, we can represent the terms in the sum of Eq. A.5 by diagrams: n vertices correspond to the θ functions, and lines between pairs of vertices correspond to derivatives. We then have the following rules (where i and j index the vertices):

1. Lines can only join distinct vertices $i \neq j$.
2. Either no lines or an odd number of lines emanate from each vertex.
3. Each line contributes a factor ρ_{ij} .
4. Each vertex i contributes a factor (where ℓ_i is its number of lines):

$$\begin{cases} \frac{1}{2} & \ell_i = 0, \\ (-1)^{\frac{\ell_i-1}{2}} \frac{(\ell_i-2)!!}{\sqrt{2\pi}} t_i & \ell_i > 0. \end{cases} \quad (\text{A.9})$$

5. Each diagram is multiplied by $\left(\prod_{i < j} \ell_{ij}\right)^{-1}$, where ℓ_{ij} is the number of lines joining the vertices i and j .

For example, consider $n = 2$; $\rho_{12} \equiv \rho$. Rules 1 and 2 imply that all diagrams have either no lines or an odd number of lines, and there is only one possibility for each. The diagrams may be easily characterized and summed:

$$\bullet \quad \bullet \quad + \quad \bullet \text{---} \bullet \quad + \quad \bullet \text{---} \circ \text{---} \bullet \quad + \quad \bullet \text{---} \circ \text{---} \circ \text{---} \bullet \quad + \quad \dots$$

$$\frac{1}{2^2} \quad + \quad \left(\frac{1}{1!}\right) \rho^{\frac{[(-1)!!]^2}{2\pi}} t_1 t_2 \quad + \quad \left(\frac{1}{3!}\right) \rho^3 \frac{[1!!]^2}{2\pi} t_1 t_2 \quad + \quad \left(\frac{1}{5!}\right) \rho^5 \frac{[3!!]^2}{2\pi} t_1 t_2 \quad + \quad \dots$$

As we have already noted, the series sums to the well-known result $\frac{1}{4} + \frac{1}{2\pi} t_1 t_2 \arcsin(\rho)$.

Note that ℓ lines have 2ℓ endpoints, so a diagram must have $\sum_{i=1}^n \ell_i = 2\ell$. For $n = 3$, this condition requires that one of the points has no lines joined to it (since a sum of three odd numbers is odd), and therefore, the $n = 3$ sum is just the three permutations of $n = 2$, appropriately scaled:

$$\langle f \rangle = \frac{1}{8} + \frac{1}{4\pi} (t_1 t_2 \arcsin \rho_{12} + t_2 t_3 \arcsin \rho_{23} + t_1 t_3 \arcsin \rho_{13}). \quad (\text{A.10})$$

However, for higher n , the diagrams rapidly become more complex.

Appendix B

Generalized Effects of Source Structure on the Modulation Index

We have noted the relationship between source size and the modulation index for a square-law structure function: $m^2 = 1 - 4\gamma_s + \mathcal{O}(\gamma_s^2)$. We now derive a more general form of this relationship, suitable for arbitrary structure functions, which we use to relate the emission size inferences of Chapter 4 to more general scattering possibilities.

The modulation index is simply the autocorrelation function of the diffractive scintillation pattern at zero lag, which is also the mean squared snapshot visibility on a vanishing baseline, averaged over a diffractive ensemble. As we have already noted, the region $\{y_2 \gg r_0, y_3 \lesssim r_0\}$ in Eq. 5.16 gives this contribution:

$$\begin{aligned} \langle |\Delta V_{\text{ss}}(0)|^2 \rangle_{\text{diff}} &= \frac{1}{(2\pi r_{\text{F}}^2)^2} \int_{\substack{y_3 \lesssim r_0 \\ y_2 \gg r_0}} d^2 \mathbf{y}_{2,3} e^{i r_{\text{F}}^{-2} \mathbf{y}_2 \cdot \mathbf{y}_3} e^{-\frac{1}{2} [2D_\phi(\mathbf{y}_3) + 2D_\phi(\mathbf{y}_2) - D_\phi(\mathbf{y}_2 + \mathbf{y}_3) - D_\phi(\mathbf{y}_2 - \mathbf{y}_3)]} \\ &\quad \times \left| \int d^2 \mathbf{s} e^{i \frac{\mathbf{k}}{R} \mathbf{s} \cdot \mathbf{y}_2} I_{\text{source}}(\mathbf{s}) \right|^2. \end{aligned} \quad (\text{B.1})$$

We approximate the second exponential as

$$e^{-\frac{1}{2}[2D_\phi(\mathbf{y}_3)+2D_\phi(\mathbf{y}_2)-D_\phi(\mathbf{y}_2+\mathbf{y}_3)-D_\phi(\mathbf{y}_2-\mathbf{y}_3)]} \approx e^{-D_\phi(\mathbf{y}_3)} \quad (\text{B.2})$$

to obtain the following representation for the modulation index:

$$m^2 \approx \frac{1}{(2\pi r_F^2)^2} \int_{\substack{y_3 \lesssim r_0 \\ y_2 \gg r_0}} d^2 \mathbf{y}_{2,3} e^{ir_F^{-2} \mathbf{y}_2 \cdot \mathbf{y}_3} e^{-D_\phi(\mathbf{y}_3)} \left| \int d^2 \mathbf{s} e^{i\frac{k}{R} \mathbf{s} \cdot \mathbf{y}_2} I_{\text{source}}(\mathbf{s}) \right|^2. \quad (\text{B.3})$$

Observe that $m^2 = 1$ for a point source. For a small, circular Gaussian distribution of intensity with standard deviation 2σ ,

$$m^2 \approx \frac{1}{4\pi \hat{\gamma}_s} \int d^2 \mathbf{y}_3 e^{-\frac{1}{4\hat{\gamma}_s} y_3^2} e^{-D_\phi(\mathbf{y}_3)}, \quad (\text{B.4})$$

$$\hat{\gamma}_s \equiv \left(\frac{kr_F \sigma}{R} \right)^2.$$

From Eq. B.4, we see that the modulation index depends on the behavior of $D_\phi(r)$ for $r \lesssim r_0$. In this region, if the inner scale is much smaller than the phase coherence length, then $D_\phi(r) \approx (r/r_0)^\alpha$. For a large inner scale, we simply take $\alpha = 2$. Then, for a small source, we expand the second exponential in Eq. B.4:

$$m^2 \approx 1 - 2^{\alpha-1} \alpha \Gamma\left(\frac{\alpha}{2}\right) \gamma_s^{\alpha/2}, \quad (\text{B.5})$$

where

$$\gamma_s = \left(\frac{k r_F^2}{R r_0} \sigma \right)^2, \quad (\text{B.6})$$

which agrees with our previous definition (e.g. Eq. 2.14) under the substitution $D\theta = r_F^2/r_0$, which corresponds to the usual refractive scale. Thus, the effects of a small transverse emission size on the modulation index are more pronounced for a Kolmogorov spectrum than for a square-law spectrum.

Eq. B.5 can then be applied to relate the estimated γ_s for different assumed structure functions. For example, our previous results have estimated γ_s for a square-law structure function (i.e. $\alpha = 2$); the corresponding inferred value for a structure function with $r_{\text{in}} \ll r_0$ is then

$$\gamma_{s,\alpha} = \left(\frac{2^{3-\alpha}}{\alpha \Gamma(\alpha/2)} \gamma_{s,\alpha=2} \right)^{2/\alpha}, \quad (\text{B.7})$$

which is the relation that we presented without a derivation in Eq. 4.9.

Bibliography

- Anantharamaiah, K. R., Ekers, R. D., Radhakrishnan, V., Cornwell, T. J., & Goss, W. M. 1989, in *Astronomical Society of the Pacific Conference Series*, Vol. 6, *Synthesis Imaging in Radio Astronomy*, ed. R. A. Perley, F. R. Schwab, & A. H. Bridle, 431–442
- Anderson, T. W. 1996, *Statistical Science*, 11, pp. 20
- Arfken, G. B., & Weber, H. J. 2005, *Mathematical methods for physicists* 6th ed.
- Armstrong, J. W., Rickett, B. J., & Spangler, S. R. 1995, *ApJ*, 443, 209
- Arons, J. 1983, *ApJ*, 266, 215
- Arons, J., & Barnard, J. J. 1986, *ApJ*, 302, 120
- Arons, J., & Scharlemann, E. T. 1979, *ApJ*, 231, 854
- Baade, W., & Zwicky, F. 1934, *Proceedings of the National Academy of Science*, 20, 259
- Backer, D. C. 1975, *A&A*, 43, 395
- Barnard, J. J., & Arons, J. 1986, *ApJ*, 302, 138
- Bhat, N. D. R., Gupta, Y., & Rao, A. P. 1999a, *ApJ*, 514, 249
- Bhat, N. D. R., Rao, A. P., & Gupta, Y. 1999b, *ApJS*, 121, 483
- Blaskiewicz, M., Cordes, J. M., & Wasserman, I. 1991, *ApJ*, 370, 643
- Boldyrev, S., & Gwinn, C. 2003, *ApJ*, 584, 791
- Cairns, I. H., Johnston, S., & Das, P. 2001, *ApJL*, 563, L65
- Cheng, K. S., Ho, C., & Ruderman, M. 1986, *ApJ*, 300, 500
- Cohen, M. H., & Cronyn, W. M. 1974, *ApJ*, 192, 193
- Cohen, M. H., Gundermann, E. J., & Harris, D. E. 1967, *ApJ*, 150, 767

- Cole, T. 1968, *Australian Journal of Physics*, 21, 273
- Cooper, B. F. C. 1970, *Australian Journal of Physics*, 23, 521
- Cordes, J. M. 1978, *ApJ*, 222, 1006
- . 2000, *ArXiv Astrophysics e-prints*
- Cordes, J. M., Boriakoff, V., & Weisberg, J. M. 1983, *ApJ*, 268, 370
- Cordes, J. M., & Lazio, T. J. W. 2002, *ArXiv Astrophysics e-prints*
- Cornwell, T. J., Anantharamaiah, K. R., & Narayan, R. 1989, *Journal of the Optical Society of America A*, 6, 977
- Cornwell, T. J., & Narayan, R. 1993, *ApJL*, 408, L69+
- Deller, A. T., Tingay, S. J., Bailes, M., & West, C. 2007, *PASP*, 119, 318
- Demorest, P. B. 2007, PhD thesis, University of California, Berkeley
- Detweiler, S. 1979, *ApJ*, 234, 1100
- Dewdney, P. E., Hall, P. J., Schilizzi, R. T., & Lazio, T. J. L. W. 2009, *IEEE Proceedings*, 97, 1482
- Dicke, R. H. 1946, *Review of Scientific Instruments*, 17, 268
- Dodson, R., Legge, D., Reynolds, J. E., & McCulloch, P. M. 2003, *ApJ*, 596, 1137
- Doeleman, S. S., et al. 2001, *AJ*, 121, 2610
- . 2008, *Nature*, 455, 78
- Dyks, J., Rudak, B., & Harding, A. K. 2004, *ApJ*, 607, 939
- Faran, Jr., J. R., & Hills, Jr., R. 1952, Technical Memo No. 27, Acoustics Research Laboratory, Harvard University
- Fisher, R. A. 1915, *Biometrika*, 10, pp. 507
- . 1921, *Metron*, 1, 3
- Fridman, P. 2009, *A&A*, 502, 401
- Goldreich, P., & Julian, W. H. 1969, *ApJ*, 157, 869
- Goodman, J., & Narayan, R. 1989, *MNRAS*, 238, 995
- Goodman, J. W. 1985, *Statistical optics*, ed. Michelson, A. M. & Levesque, A. H.

- Goodman, N. R. 1963, *The Annals of Mathematical Statistics*, 34, pp. 152
- Gupta, Y., & Gangadhara, R. T. 2003, *ApJ*, 584, 418
- Gwinn, C. 2004, *PASP*, 116, 84
- Gwinn, C. R. 2001, *ApJ*, 554, 1197
- . 2006, *PASP*, 118, 461
- Gwinn, C. R., Bartel, N., & Cordes, J. M. 1993a, *ApJ*, 410, 673
- . 1993b, *ApJ*, 410, 673
- Gwinn, C. R., Britton, M. C., Reynolds, J. E., Jauncey, D. L., King, E. A., McCulloch, P. M., Lovell, J. E. J., & Preston, R. A. 1998, *ApJ*, 505, 928
- Gwinn, C. R., Danen, R. M., Tran, T. K., Middleditch, J., & Ozernoy, L. M. 1991, *ApJL*, 381, L43
- Gwinn, C. R., & Johnson, M. D. 2011, *ApJ*, 733, 51
- Gwinn, C. R., Johnson, M. D., Smirnova, T. V., & Stinebring, D. R. 2011, *ApJ*, 733, 52
- Gwinn, C. R., et al. 1997, *ApJL*, 483, L53+
- . 2000, *ApJ*, 531, 902
- . 2012a, *ApJ*, 758, 6
- . 2012b, *ApJ*, 758, 7
- Hagen, J. B., & Farley, D. T. 1973, *Radio Science*, 8, 775
- Hankins, T. H. 1971, *ApJ*, 169, 487
- Hankins, T. H., Kern, J. S., Weatherall, J. C., & Eilek, J. A. 2003, *Nature*, 422, 141
- Hewish, A. 1975, *Science*, 188, 1079
- Hewish, A., Bell, S. J., Pilkington, J. D. H., Scott, P. F., & Collins, R. A. 1968, *Nature*, 217, 709
- Hewish, A., Scott, P. F., & Wills, D. 1964, *Nature*, 203, 1214
- Hibschman, J. A., & Arons, J. 2001, *ApJ*, 546, 382

- Hill, A. S., Stinebring, D. R., Asplund, C. T., Berwick, D. E., Everett, W. B., & Hinkel, N. R. 2005, *ApJL*, 619, L171
- Hobbs, G., et al. 2010, *Classical and Quantum Gravity*, 27, 084013
- Hotan, A. W., van Straten, W., & Manchester, R. N. 2004, *PASA*, 21, 302
- Hotelling, H. 1953, *Journal of the Royal Statistical Society. Series B (Methodological)*, 15, pp. 193
- Ioka, K. 2003, *ApJL*, 598, L79
- Isserlis, L. 1918, *Biometrika*, 12, pp. 134
- Jackson, J. D. 1998, *Classical Electrodynamics*, 3rd Edition
- Jenet, F. A., & Anderson, S. B. 1998, *PASP*, 110, 1467
- Jenet, F. A., et al. 2006, *ApJ*, 653, 1571
- Johnson, M. D., Chou, H. H., & Gwinn, C. R. 2013a, *ApJ*, 765, 135
- Johnson, M. D., & Gwinn, C. R. 2012, *ApJ*, 755, 179
- . 2013, *ApJ*, Accepted
- Johnson, M. D., Gwinn, C. R., & Demorest, P. 2012, *ApJ*, 758, 8
- Johnson, M. D., Gwinn, C. R., & Demorest, P. B. 2013b, in prep
- Johnston, S., Hobbs, G., Vigeland, S., Kramer, M., Weisberg, J. M., & Lyne, A. G. 2005, *MNRAS*, 364, 1397
- Johnston, S., Nicastro, L., & Koribalski, B. 1998, *MNRAS*, 297, 108
- Johnston, S., van Straten, W., Kramer, M., & Bailes, M. 2001, *ApJL*, 549, L101
- Kapoor, R. C., & Shukre, C. S. 1998, *ApJ*, 501, 228
- Karastergiou, A., & Johnston, S. 2007, *MNRAS*, 380, 1678
- Kardashev, N. S. 2009, *Physics Uspekhi*, 52, 1127
- Kardashev, N. S., et al. 2013, *Astronomy Reports*, 57, 153
- Kendall, M., & Stuart, A. 1979, *The advanced theory of statistics. Vol.2: Inference and relationship*
- Kijak, J., & Gil, J. 1997, *MNRAS*, 288, 631

- Komesaroff, M. M. 1970, *Nature*, 225, 612
- Komesaroff, M. M., Hamilton, P. A., & Ables, J. G. 1972, *Australian Journal of Physics*, 25, 759
- Kramer, M., Johnston, S., & van Straten, W. 2002, *MNRAS*, 334, 523
- Kramer, M., et al. 2006, *Science*, 314, 97
- Krishnamohan, S., & Downs, G. S. 1983, *ApJ*, 265, 372
- Kulkarni, S. R. 1989, *AJ*, 98, 1112
- Lai, D., Chernoff, D. F., & Cordes, J. M. 2001, *ApJ*, 549, 1111
- Lambert, H. C., & Rickett, B. J. 1999, *ApJ*, 517, 299
- Lazio, T. J. W., & Cordes, J. M. 1998, *ApJ*, 505, 715
- Lee, L. C., & Jokipii, J. R. 1975, *ApJ*, 196, 695
- Lehmann, E. L., & Casella, G. 1998, *Theory of Point Estimation* (New York: Springer-Verlag)
- Little, L. T., & Hewish, A. 1966, *MNRAS*, 134, 221
- Lorimer, D. R., & Kramer, M. 2004, *Handbook of Pulsar Astronomy*, ed. R. Ellis, J. Huchra, S. Kahn, G. Rieke, & P. B. Stetson
- Lovelace, R. V. E. 1970, PhD thesis, CORNELL UNIVERSITY.
- Lundgren, S. C., Cordes, J. M., Ulmer, M., Matz, S. M., Lomatch, S., Foster, R. S., & Hankins, T. 1995, *ApJ*, 453, 433
- Lyne, A. G., & Graham-Smith, F. 1998, *Cambridge Astrophysics Series*, 31
- Lyne, A. G., & Lorimer, D. R. 1994, *Nature*, 369, 127
- Lyutikov, M., & Parikh, A. 2000, *ApJ*, 541, 1016
- Macquart, J., Johnston, S., Walker, M., & Stinebring, D. 2000, in *Astronomical Society of the Pacific Conference Series*, Vol. 202, IAU Colloq. 177: Pulsar Astronomy - 2000 and Beyond, ed. M. Kramer, N. Wex, & R. Wielebinski, 215–+
- Macquart, J.-P., & Bower, G. C. 2006, *ApJ*, 641, 302
- Mallik, R. 2003, *Information Theory, IEEE Transactions on*, 49, 1499

- McMahon, E. 1964, *Information Theory, IEEE Transactions on*, 10, 168
- Melrose, D. 2004, in *IAU Symposium, Vol. 218, Young Neutron Stars and Their Environments*, ed. F. Camilo & B. M. Gaensler, 349
- Mitra, D., Gil, J., & Melikidze, G. I. 2009, *ApJL*, 696, L141
- Moran, J. M. 1976, *Methods of Experimental Physics*, 12, 228
- Narayan, R. 1993, in *Pulsars as Physics Laboratories*, ed. J. M. Shull & H. A. Thronson, 151–165
- Narayan, R., & Goodman, J. 1989, *MNRAS*, 238, 963
- Newton, Isaac, S. 1730, *Opticks*
- Ng, C.-Y., & Romani, R. W. 2004, *ApJ*, 601, 479
- . 2008, *ApJ*, 673, 411
- Ozernoi, L. M., & Shishov, V. I. 1979, *Pis ma Astronomicheskii Zhurnal*, 5, 171
- Pacini, F. 1967, *Nature*, 216, 567
- Palfreyman, J. L., Hotan, A. W., Dickey, J. M., Young, T. G., & Hotan, C. E. 2011, *ApJL*, 735, L17+
- Pawula, R. 1967, *Information Theory, IEEE Transactions on*, 13, 285
- Phillips, J. A. 1992, *ApJ*, 385, 282
- Price, R. 1958, *Information Theory, IRE Transactions on*, 4, 69
- Radhakrishnan, V., & Cooke, D. J. 1969, *Astrophys. Lett.*, 3, 225
- Ramachandran, R., Demorest, P., Backer, D. C., Cognard, I., & Lommen, A. 2006, *ApJ*, 645, 303
- Rankin, J. M. 1990, *ApJ*, 352, 247
- Rickett, B., Johnston, S., Tomlinson, T., & Reynolds, J. 2009, *MNRAS*, 395, 1391
- Rickett, B. J. 1975, *ApJ*, 197, 185
- . 1977, *ARA&A*, 15, 479
- . 1990, *ARA&A*, 28, 561
- Rickett, B. J., Coles, W. A., & Bourgois, G. 1984, *A&A*, 134, 390

- Rickett, B. J., Hankins, T. H., & Cordes, J. M. 1975, *ApJ*, 201, 425
- Roberts, J. A., & Ables, J. G. 1982, *MNRAS*, 201, 1119
- Romani, R. W. 1996, *ApJ*, 470, 469
- Ruderman, M. A., & Sutherland, P. G. 1975, *ApJ*, 196, 51
- Salpeter, E. E. 1967, *ApJ*, 147, 433
- Scheuer, P. A. G. 1968, *Nature*, 218, 920
- Shen, Z.-Q., Lo, K. Y., Liang, M.-C., Ho, P. T. P., & Zhao, J.-H. 2005, *Nature*, 438, 62
- Shishov, V. I. 2010, *Astronomy Reports*, 54, 724
- Smirnova, T. V., & Shishov, V. I. 2010, *Astronomy Reports*, 54, 139
- Spangler, S. R., & Gwinn, C. R. 1990, *ApJL*, 353, L29
- Srednicki, M. 2007, *Quantum Field Theory*, ed. Srednicki, M.
- Stinebring, D. R., Smirnova, T. V., Hankins, T. H., Hovis, J. S., Kaspi, V. M., Kempner, J. C., Myers, E., & Nice, D. J. 2000, *ApJ*, 539, 300
- Sturrock, P. A. 1971, *ApJ*, 164, 529
- Tatarskii, V. I. 1971, *The effects of the turbulent atmosphere on wave propagation*
- Taylor, J. H., & Cordes, J. M. 1993, *ApJ*, 411, 674
- Taylor, J. H., & Weisberg, J. M. 1989, *ApJ*, 345, 434
- Thompson, A. R., Moran, J. M., & Swenson, Jr., G. W. 2001, *Interferometry and Synthesis in Radio Astronomy*, 2nd Edition
- van Straten, W. 2009, *ApJ*, 694, 1413
- van Straten, W., & Bailes, M. 2011, *PASA*, 28, 1
- Van Vleck, J. H., & Middleton, D. 1966, *Proceedings of the IEEE*, 54, 2
- Verbiest, J. P. W., et al. 2009, *MNRAS*, 400, 951
- Weinreb, S. 1963, *Technical Report 412*, Research Laboratory of Electronics, MIT
- Williamson, I. P. 1972, *MNRAS*, 157, 55
- Woltjer, L. 1964, *ApJ*, 140, 1309
- Zmuidzinas, J. 2003, *Appl. Opt.*, 42, 4989